How Biotechnological Advances are Transforming Monoclonal Antibody Production

Article Collection

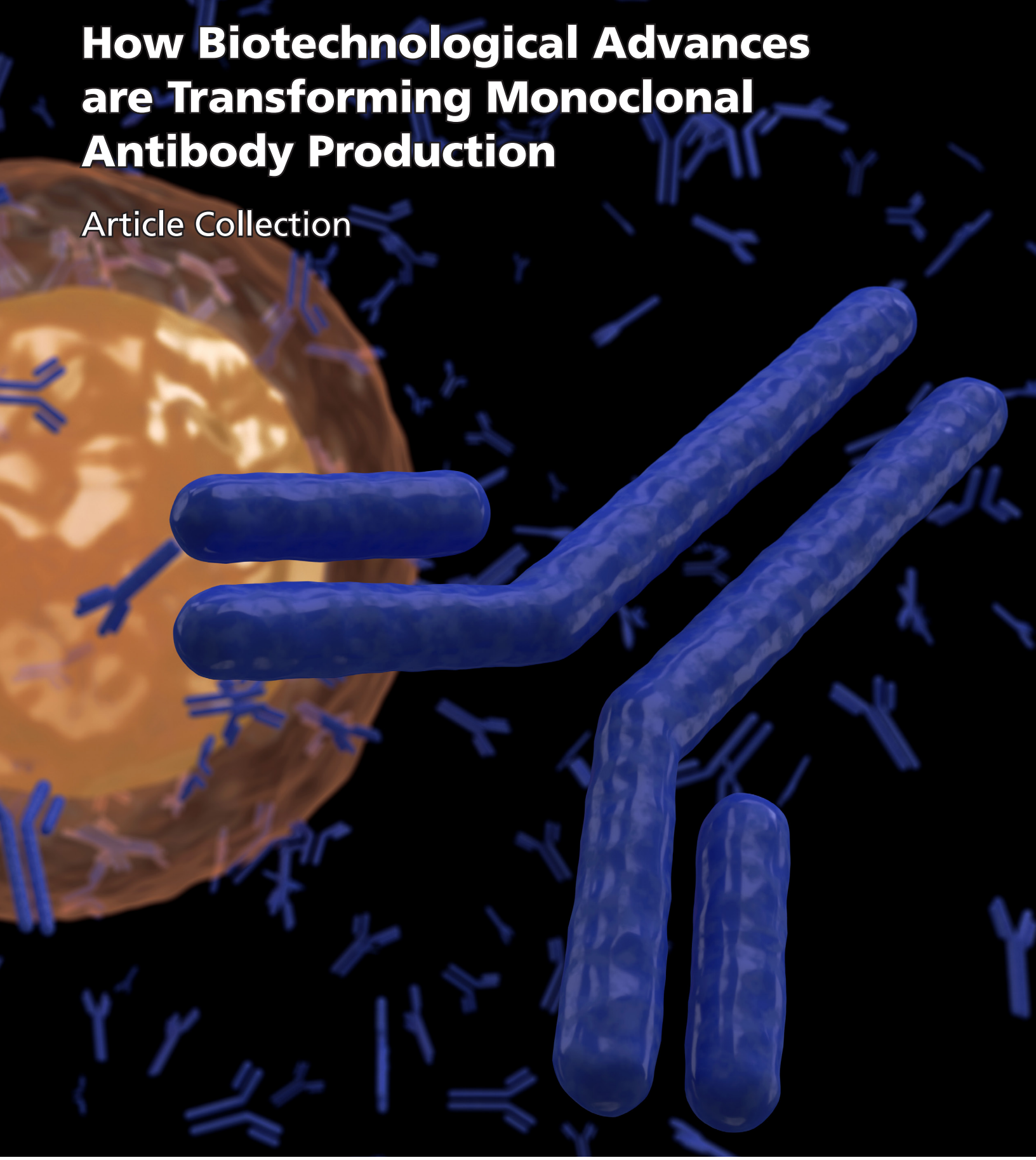

Sponsored by:

WILEY

CURRENT PROTOCOLS
A Wiley Brand

cytiva

cytiva

In silico process development for antibody-drug conjugates

Molecular engineering, conjugation, and purification. The manufacture of antibody-drug conjugates (ADCs) requires a delicate balance of all three. And, in downstream processing, it can take significant experimental effort to find the right operating conditions.

By replacing lab experiments with computer simulations, mechanistic models offer more than highly efficient and robust ADC processes — they eliminate potential exposure to highly toxic chemicals, creating a safer work environment.

Discover solutions from Cytiva for simulating chromatography processes in today's growing molecular diversity.

Learn more

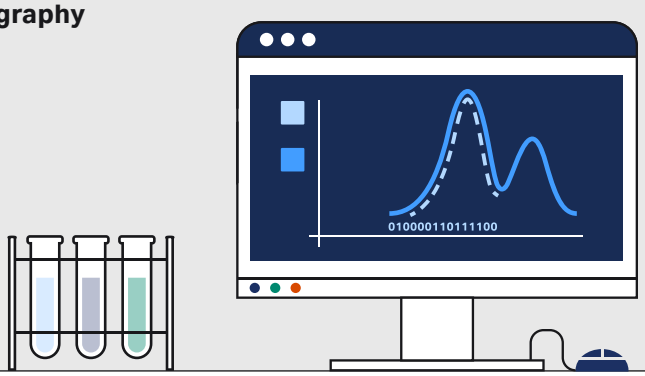

cytiva

Charting a new course in downstream bioprocessing

When you think of biomolecules, does your mind automatically go to mAbs?

It's an exciting time to be working at the forefront of medical innovation as biomolecules expand beyond mAbs — to include plasmids, mRNA, oligos, cell and gene therapies, antibody variants, vaccines, and more.

At Cytiva, we've been helping scientists bring novel therapies to market for many years. Whether you're just starting out in the lab or moving through trials to market, you can rely on our downstream experience to optimize and accelerate your process.

Learn more

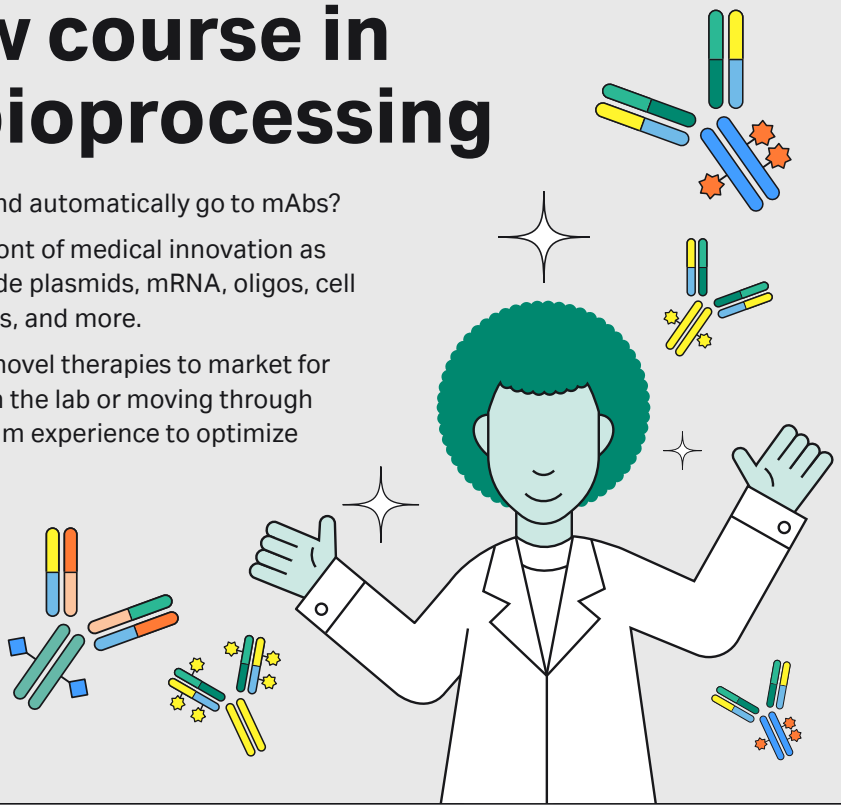

Contents

Imprint

John Wiley & Sons, Inc.
111 River Street,
Hoboken, NJ 07030-5774
USA
Contact: Customer Service

Editor at Wiley Analytical Science:
Róisín Murtagh

Senior Account Manager:
Joseph Tomaszewski

Cytiva
CY41723-8Apr24-EB
cytiva.com

Introduction

Over the last decade, the monoclonal antibody (mAb) therapy market has evolved as a rapidly growing segment within the research sector and the pharmaceutical industry, driven by its pivotal role in treating various diseases. The development and use of mAbs have revolutionized treatment options for many patients, particularly those with breast cancer, leukemia, or lymphoma. By targeting highly specific markers on cancer cells, these therapies can offer more personalized treatment, often with fewer side effects compared to traditional chemotherapy. At present, the market is seeing expansion due to the rising acceptance of new mAb products, ongoing research and development efforts, and a growing number of chronic diseases that require innovative treatment alternatives.

Antibody-drug conjugates (ADCs) are a type of treatment that combines the targeted nature of mAbs with the toxic effects of chemotherapy. Their composition comprises three primary constituents: a mAb, a linker, and a cytotoxic drug. In this context, ADCs are synthetic molecules engineered to serve as substitute antibodies that can restore, enhance, or mimic the immune system. They are designed to bind to specific targets found on cells, such as cancer cells. Each ADC specifically targets a single protein, like a key that precisely fits into a particular lock.

ADCs and mAbs are both integral parts of the modern therapeutic landscape, particularly in oncology, but their applications extend to non-oncology applications as well. They are closely related in that ADCs are a complex moiety designed to deliver potent cytotoxic drugs directly to cancer cells, taking advantage of the specificity of mAbs. This type of medical treatment involves the use of mAbs that are engineered to target specific antigens found on the surface of cells. These antibodies can be engineered to perform various functions, such as blocking cell growth, triggering an immune response to destroy cancer cells, or delivering cytotoxic agents directly to cancer cells. mAbs are also used to treat other diseases, such as autoimmune diseases and infections. They work by mimicking the immune system's ability to fight off harmful pathogens or by interfering with disease progression at the molecular level.

This Expert Insights eBook begins with a research paper from São Pedro *et al.* [1], published on June 13, 2023, presenting the development and successful implementation of a miniaturized Process Analytical Technology (PAT) tool—a fluorescent dye-based microfluidic sensor—for real-time detection of mAb aggregates in a biopharmaceutical manufacturing process. Protein aggregation is a significant concern in the biopharmaceutical industry. High molecular weight species or protein aggregates can compromise the safety and efficacy of therapeutic products, such as monoclonal antibodies. However, traditional methods of detecting these aggregates are often invasive, time-consuming, and not suited for real-time monitoring.

This study introduces a miniaturized sensor that detects these aggregates quickly, effectively marking a significant advancement in the field. The sensor utilizes fluorescent dyes

such as Bis-ANS and CCVJ to detect protein aggregation and was tested in an integrated ÄKTA avant unit, using its capability to detect as low as 2.5% aggregation levels in under 10 minutes. This development is significantly contributing to faster decision-making and better process control in a biopharmaceutical manufacturing process.

In another publication from São Pedro *et al.* [2] in the same year, the fluorescent dye-based microfluidic sensor is introduced for fast, at-line PAT to monitor aggregate formation. The authors emphasize the lack of effective real-time analytical technologies as a bottleneck in the transition to continuous biomanufacturing, particularly for mAb production, where aggregate formation is a critical quality attribute. In this instance, the fluorescent dye-based microfluidic sensor provides a significant solution for detecting a variety of mAb aggregates and can be easily integrated into downstream unit operations.

The study induced various mAb aggregates using factors like temperature, pH shift, and freeze-thaw cycles. Four fluorescent dyes—Bis-ANS, CCVJ, Thioflavin T (ThT), and Nile Red—were assessed for their ability to detect aggregation. Bis-ANS and CCVJ were found to robustly detect 2.5% to 10% of aggregation and were validated in a lab-scale purification system. The ÄKTA avant system was an integral part of the study for validating the fluorescent dye-based microfluidic sensor's capability to detect mAb aggregates in a real chromatographic process, demonstrating the sensor's potential for real-time monitoring in continuous biomanufacturing.

The third research paper from Hahn *et al.* [3], published on May 20, 2023, presents a transformative approach to mAb purification in biotherapeutics production. Their purification is a critical step in ensuring safety and efficacy. Traditionally, protein A affinity chromatography has been the method of choice. However, as with any technology, it comes with its set of challenges, particularly when scaling up or down. Moreover, the complexity of mass transfer effects in bead-based resins often leads to inefficiencies and escalated costs. This study explores fiber-based technology as an alternative, which does not have related issues, potentially simplifying the scaling process.

Fiber-based chromatography, using a well-defined matrix of cellulose fibers, offers a more accessible surface area compared to beads, facilitating convection, and simplifying adsorption processes. The research included small to pilot scale fiber-based protein A affinity adsorber units, employing ÄKTA systems for chromatographic processes. to investigate and understand the adsorption/desorption processes. The research successfully demonstrated the predictive scaling of fiber-based protein A capture chromatography, suggesting that with accurate modeling, fiber-based chromatography could be a viable and efficient alternative for the biopharma industry.

Our fourth research study, published by Lorek *et al.* [4] on November 5, 2023, demonstrates how high throughput screening (HTS) can accelerate downstream process

development in biotechnology, particularly for monoclonal antibodies. The study conducted HTS in batch binding mode to analyze the monovalent antibodies (mvAbs) interactions with different anion exchange and mixed-mode resins at relevant conditions. The findings show that HTS can accurately predict mvAb behavior in larger-scale processes. It also emphasized the importance of understanding mAb molecular interactions and surface properties for improved downstream processes, providing a way to rapidly identify optimal conditions and predict large-scale process outcomes.

The final study published by Eltahir *et al.* [5] on May 19, 2022, focuses on the development of Adaptable Drug Affinity Conjugate (ADAC) technology for improved delivery and presentation of synthetic peptide-based vaccines, targeting CD40 on antigen-presenting cells for cancer therapy. ADAC combines agonistic CD40 antibodies with a high-affinity cargo peptide interaction, allowing for targeted delivery and sustained release within cells. It holds the promise of transforming cancer therapy into a more effective and personalized treatment due to its ability to improve peptide stability, target delivery, and adapt to individual needs. The production, purification, and characterization of the antibodies utilized in the ADAC technology were supported by Cytiva products, including but not limited to HiTrap Protein A HP pre-packed columns, HiLoad pre-packed columns, and the Biacore surface plasmon resonance (SPR) system.

Overall, biotechnological manufacturing of monoclonal antibodies represents a significant step forward in medical therapies, addressing a wide range of diseases. Advancements in biotechnological processes, such as the development of innovative PAT tools for real-time monitoring and the exploration of novel purification techniques, have the potential to streamline the manufacturing process. These improvements ensure the production of high-quality, effective mAbs, which is critical given the expanding landscape of biopharmaceutical therapies and the growing demand for novel treatment options in modern medicine.

We hope that researchers will find this collection of articles useful in their pursuit of knowledge about the latest developments in the field of biopharmaceutical drug research and manufacturing, specifically regarding monoclonal antibodies (mAbs) and antibody-drug conjugates, as well as in precision medicine. For more information, we encourage you to visit the antibody production workflow page at Cytiva to gain a deeper understanding of available options for improving the development and manufacturing of monoclonal antibodies, bispecific antibodies, fragments, and more.

Julian Renpenning, Ph.D.

References

[1] São Pedro, M.N. et al. (2023). Real-time detection of mAb aggregates in an integrated downstream process. *Biotechnology and Bioengineering.* DOI: 10.1002/BIT.28466.

[2] São Pedro, M.N. et al. (2023). Application of a fluorescent dye-based microfluidic sensor for real-time detection of mAb aggregates. *Biotechnology Progress.* DOI: 10.1002/BTPR.3355.

[3] Hahn, T. et al. (2023). Predictive scaling of fiber-based protein A capture chromatography using mechanistic modeling. *Biotechnology and Bioengineering.* DOI: 10.1002/BIT.28434.

[4] Lorek, J.K. et al. (2023). High throughput screening for rapid and reliable prediction of monovalent antibody binding behavior in flowthrough mode. *Biotechnology and Bioengineering.* DOI: 10.1002/BIT.28572.

[5] Eltahir, M. et al. (2022). An Adaptable Antibody-Based Platform for Flexible Synthetic Peptide Delivery Built on Agonistic CD40 Antibodies. *Advanced Therapeutics.* DOI: 10.1002/ADTP.202200008.

Received: 31 March 2023 | Revised: 12 May 2023 | Accepted: 31 May 2023

DOI: 10.1002/bit.28466

ARTICLE

BIOTECHNOLOGY AND BIOENGINEERING WILEY

Real-time detection of mAb aggregates in an integrated downstream process

Mariana N. São Pedro[1] | Madelène Isaksson[2] | Joaquín Gomis-Fons[2] | Michel H. M. Eppink[3,4] | Bernt Nilsson[2] | Marcel Ottens[1]

[1]Department of Biotechnology, Delft University of Technology, Delft, The Netherlands

[2]Department of Chemical Engineering, Lund University, Lund, Sweden

[3]Byondis B. V., Nijmegen, The Netherlands

[4]Bioprocessing Engineering, Wageningen University, Wageningen, The Netherlands

Correspondence

Marcel Ottens, Department of Biotechnology, Delft University of Technology, Van der Maasweg 9, Delft 2629 HZ, The Netherlands.
Email: m.ottens@tudelft.nl

Funding information

CODOBIO

Abstract

The implementation of continuous processing in the biopharmaceutical industry is hindered by the scarcity of process analytical technologies (PAT). To monitor and control a continuous process, PAT tools will be crucial to measure real-time product quality attributes such as protein aggregation. Miniaturizing these analytical techniques can increase measurement speed and enable faster decision-making. A fluorescent dye (FD)-based miniaturized sensor has previously been developed: a zigzag microchannel which mixes two streams under 30 s. Bis-ANS and CCVJ, two established FDs, were employed in this micromixer to detect aggregation of the biopharmaceutical monoclonal antibody (mAb). Both FDs were able to robustly detect aggregation levels starting at 2.5%. However, the real-time measurement provided by the microfluidic sensor still needs to be implemented and assessed in an integrated continuous downstream process. In this work, the micromixer is implemented in a lab-scale integrated system for the purification of mAbs, established in an ÄKTA™ unit. A viral inactivation and two polishing steps were reproduced, sending a sample of the product pool after each phase directly to the microfluidic sensor for aggregate detection. An additional UV sensor was connected after the micromixer and an increase in its signal would indicate that aggregates were present in the sample. The at-line miniaturized PAT tool provides a fast aggregation measurement, under 10 min, enabling better process understanding and control.

KEYWORDS

antibody aggregation, continuous biomanufacturing, fluorescent dyes, microfluidic sensor, process analytical technology (PAT)

Abbreviations: Bis-ANS, 4-4-bis-1-phenylamino-8-naphthalene sulfonate; CCVJ, 9-(2-carboxy-2-cyanovinyl)julolidine; ColV, column valve; CQA, critical quality attribute; FD, fluorescent dye; FT, flow through; HMW, high molecular weight; InjV, injection valve; InlS, inlet valve; LOD, limit of detection; LoopV, loop valve; MALS, multi-angle light scattering; OutV, outlet valve; VI, viral inactivation; VV, versatile valve; λ_{em}, emission wavelength; λ_{exc}, excitation wavelength.

1 | INTRODUCTION

A challenge in the implementation of continuous biomanufacturing by the biopharmaceutical industry is the shortage of process analytical technologies (PAT) (Chopda et al., 2021; São Pedro, Silva, et al., 2021). A real-time measurement of certain critical quality attributes (CQAs), such as protein aggregation, is imperative to provide decisive information for subsequent steps and to facilitate process control (Mandenius & Gustavsson, 2015). For the biomanufacturing of monoclonal antibodies (mAbs), the presence of high molecular weight (HMW) species is undesirable (Bansal et al., 2019). With several known aggregation inducing factors being present in the downstream process (Telikepalli et al., 2014; Walchli et al., 2020), a PAT tool capable to detect the formation of these HMW species is essential. Miniaturized biosensors as in-line or on-line PAT tool could speed up the analytical measurement to the required time frame for decision-making. The inherent short operation time, the small sample volume required (in the scale of nL or µL) and the easiness of fabrication are just a few advantages provided by the miniaturization of the analytical technique (São Pedro, Klijn, et al., 2021).

Fluorescent dyes (FD), such as 4-4-bis-1-phenylamino-8-naphthalene sulfonate (Bis-ANS) and 9-(2-carboxy-2-cyanovinyl) julolidine (CCVJ), have been employed to detect and study protein aggregation (Paul et al., 2017). The fluorescence of these molecules is intensified due to changes in the hydrophobicity, Bis-ANS (He et al., 2010), or the viscosity of the surrounding environment, CCVJ (Oshinbolu et al., 2018). Since these dyes provide an immediate and straightforward measurement of aggregation, a FD-based microfluidic biosensor for aggregate detection was designed and developed. A zigzag micromixer, represented in Figure 1, is capable of effectively mixing two different streams within 30 s (São Pedro et al., 2022). The micromixer is comprised of two inlets and one outlet, where the mixing occurs due to the 45° zigzag design, with a total of 30 mixing units. This zigzag structure was applied to detect the presence of HMW species in a variety of mAb aggregation samples, induced by different induction factors (like temperature, freeze-thawing, or low pH incubation). Depending on the FD employed, the developed micromixer was able to robustly detect, at least, 2.5% of aggregation (São Pedro et al., 2023).

Although the micromixer was able to successfully detect aggregation in a single unit operation, an anion exchange (AEX) chromatography (São Pedro et al., 2023), further validation in an integrated downstream process is still required. Therefore, in this work, the developed PAT tool will be assessed for aggregate detection in a lab-scale integrated system, established in an ÄKTA™ Avant unit. The final steps of a mAb purification scheme were carried out: a low-pH viral inactivation (VI) step followed by two polishing steps, a bind-and-elute cation exchange (CEX) and a flow-through (FT) AEX chromatography step. The presence of aggregates in the final purification steps is critical, especially after the polishing steps, since these steps were designed and developed to remove any product related impurities. After each unit operation, a sample of either the FT pool or the eluate was directly sent to the micromixer for aggregate detection. An increase in the UV absorbance would

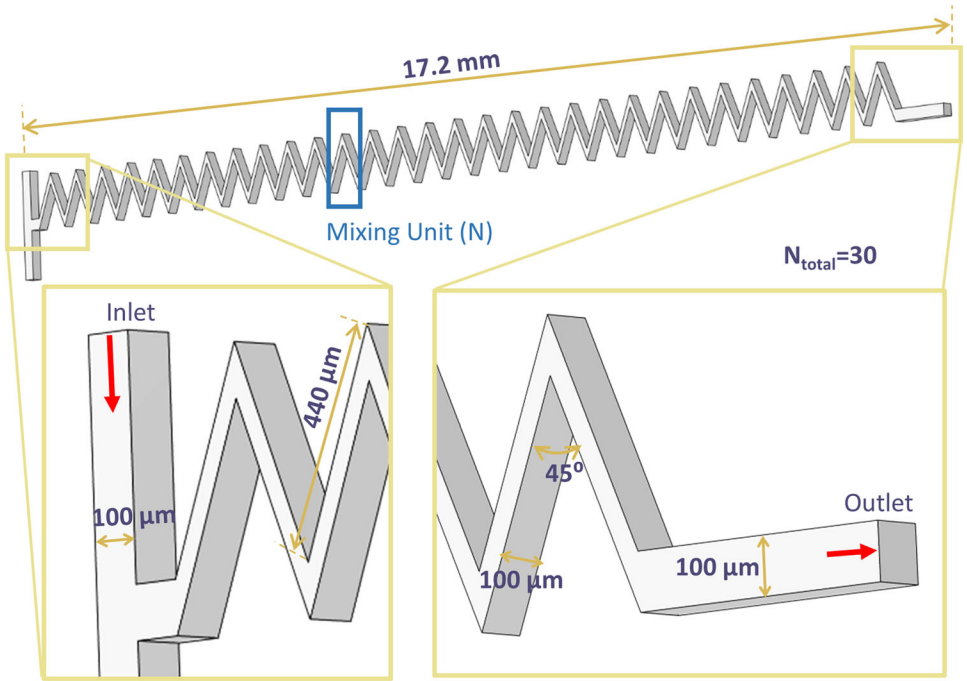

FIGURE 1 3D schematic representation of the micromixer structure, with the relevant measurements described. The zigzag mixing unit (N) of the micromixer is highlighted in blue, with the structure being a consecutive repetition of 30 N and having a total mixing length of around 27 mm (calculated based on the 30 N and the length of the zigzag channel diagonally, 440 µm). The red arrows indicate the flow of both liquids entering in one of the inlets and the resulting mixed liquid exiting at the outlet.

mean that aggregates were present in the sample, which would subsequently be confirmed by off-line analytical size exclusion chromatography (SEC-UPLC). The micromixer was able to effectively detect aggregation in the samples validated with an offline measurement, demonstrating the potential of creating a real-time measurement by the miniaturization of the analytical technique.

2 | MATERIALS AND METHODS

Poly(dimethylsiloxane) (PDMS) was purchased as a Sylgard 184 elastomer kit (Dow Corning). Dimethylsiloxane-(60%–70% ethylene oxide) block copolymer was acquired from Gelest. Sodium phosphate monobasic dehydrate was purchased from Sigma-Aldrich. Di-sodium hydrogen phosphate and sodium chloride were bought from VWR Chemicals (VWR International), whereas sodium acetate was purchased from Merck Aldrich. Acetic acid was obtained from Fluka and sodium hydroxide from J. T. Baker (VWR International). Regarding the FDs, CCVJ, and Bis-ANS were purchased from Sigma-Aldrich and Invitrogen, respectively. The mAb used was supplied by Byondis B. V., with an isoelectric point of 8.6.

The integrated downstream process was implemented in an ÄKTA Avant system (Figure 2), controlled by the software UNICORN™ 7.5 (Cytiva). This ÄKTA unit was equipped with: three pumps (pumps A, B, and sample pump) with inlet valves in each to be able to select different buffers; a column valve (ColV); a loop valve (LoopV); an inlet (InlS) and an outlet (OutV) valve; four versatile valves (VV); an injection valve (InjV); two UV monitors; conductivity and pH sensors; and a 10 mL and two 50 mL superloops™ (all from Cytiva).

2.1 | Sample preparation

The mAb sample was stored in sodium acetate buffer, pH 4.5, at −80°C, in a concentration of 6 mg mL^{-1}. This sample was dialyzed with 50 mM sodium acetate buffer, 100 mM NaCl, pH 5, using amicon ultra-15 centrifugal filters, and concentrated to 40 mg mL^{-1}.

To prepare the stock solutions of the FD dyes, CCVJ was dissolved in dimethyl sulfoxide (Fluka) and Bis-ANS in methanol (Sigma-Aldrich). The exact concentration of each FD stock solution was calculated from the UV absorbance: for CCVJ at 440 nm, with the molar extinction of 25 404 M^{-1} cm^{-1}; and for Bis-ANS at 385 nm, with a molar extinction of 16 790 M^{-1} cm^{-1}. From the stock solutions, the FD solution was diluted with MilliQ water to a concentration of 1 µM for CCVJ and to 0.5 µM for Bis-ANS (São Pedro et al., 2023).

2.2 | Aggregate detection

2.2.1 | Microstructure fabrication

The zigzag micromixer (100 µm high × 100 µm wide × 17.2 mm long) presents two inlets and one outlet (Figure 1). More information on the dimensions and characteristics of the micromixer channel are found in São Pedro et al. (2022). In terms of the structure fabrication, the designed mold was ordered from INESC Microsystems and Nanotechnologies. To reduce the inherent hydrophobicity of PDMS and protein adsorption to the micromixer walls, the structures were fabricated according to Gökaltun et al. (2019). Dimethylsiloxane-(60%–70% ethylene oxide) block copolymer, comprised of poly(ethylene glycol) (PEG) and PDMS segments (PDMS-PEG), were blended with PDMS during device manufacturing, using a 10:1:0.0025 ratio of PDMS, curing agent, and PDMS-PEG. After being degassed, the mixture was poured onto the mold and baked at 70°C overnight. After the PDMS was cured, the chip was removed from the mold and the inlets and outlet were punched in the microstructure. Finally, the PDMS chip was bonded to a glass substrate and sealed with a 20:1 mixture of PDMS to curing agent.

2.2.2 | Off-line analytics

The mAb concentration and level of aggregation was determined off-line by analytical SEC in an UltiMate 3000 UHPLC System (Thermo Fisher Scientific). Five microliters of each sample was injected in an ACQUITY UPLC Protein BEH SEC. 200 Å column (Waters), using the running buffer 100 mM sodium phosphate buffer, pH 6.8. After the sample injection, the flow rate was set to 0.3 mL min^{-1} for 10 min and the protein detection was performed at 280 nm.

2.3 | Integrated downstream process

2.3.1 | Process conditions and buffers

The integrated downstream process included three steps: a low-pH VI; followed by a CEX step in bind/elute mode; and finally an AEX step in FT mode, starting with the injection of 1 mL of mAb sample (concentration of 40 mg mL^{-1}). The VI step was performed at a pH of 3.0 for 60 min, in one of the 50 mL superloop. The CEX column used was a 1 mL HiTrap® Capto™ S ImpAct and the AEX resin was a 1 mL HiTrap® Capto™ Adhere (both obtained from Cytiva). In total, seven different buffers were used for the loading, elution, and stripping of the columns, described in Table 1. The choice of these buffers, as well as the column volumes and flow rates employed, were based on GE Healthcare (2015). Each step was optimized separately and in batch mode beforehand to assess the formation and removal of mAb aggregates. Between several unit operations/steps, the sample buffer conditions had to be adjusted. This was performed through in-line conditioning by dilution. For the VI, the pH of the initial sample had to be lowered from 5.0 to 3.0. A solution of 0.2 M of hydrochloric acid was used, with a dilution ratio of 4:1. To increase the pH after the VI, a 100 mM sodium acetate, 150 mM sodium hydroxide solution was employed, with a dilution ratio of 4:1. Before the AEX column, the CEX eluate was diluted in-line with a ratio of 1:1, with 50 mM sodium

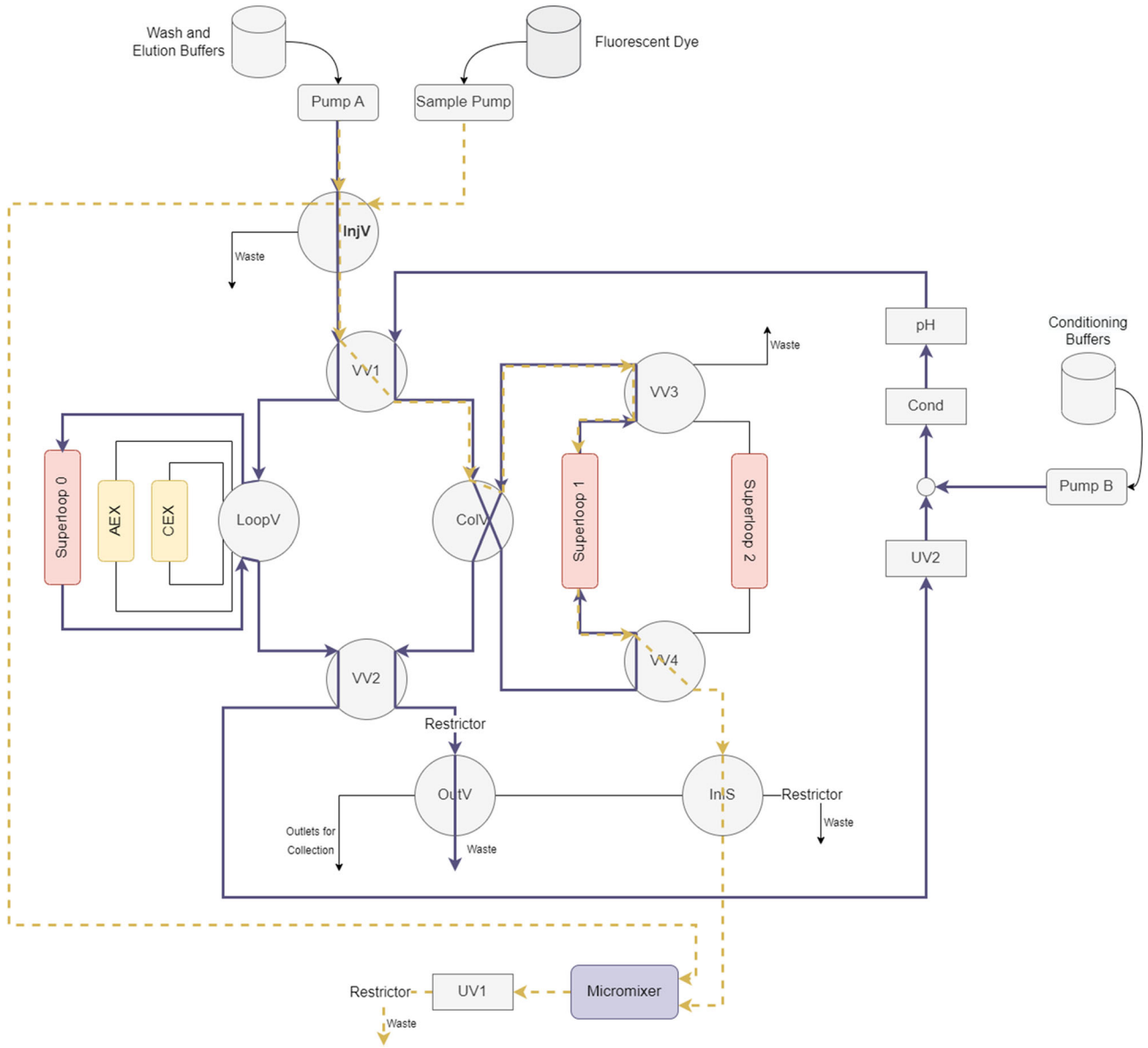

FIGURE 2 Process diagram of the integrated downstream setup with the implementation of the real-time PAT micromixer. The dark blue line represents the flow path for the sample injection in the VI step: Pump A is used to transfer the mAb sample stored in superloop 0, connected to the loop valve (LoopV), to superloop 1, where the VI step occurs, passing through UV2, conductivity (Cond) and pH meter. Since the mAb sample is stored at pH 5, Pump B is used for the in-line sample conditioning to decrease the sample's pH to 3. Similar flow paths are used for the wash and elution of the CEX and AEX chromatography steps, also connected to the LoopV, where the FT or the eluate pools are stored in superloop 1/2. The dashed gold line indicates the flow path used for aggregate detection with the micromixer: the sample pump is used to inject the fluorescent dye into the micromixer through the injection valve (InjV); while, simultaneously, the stored sample in superloop 1 is injected in the micromixer by Pump A. Both streams are mixed in the micromixer structure and the resulting mixed fluid is sent to the UV1 sensor, where, if there is aggregation, an increase in the signal is observed. Black lines represent inactive flow paths. AEX, anion exchange; CEX, cation exchange; FT, flow-through; mAb, monoclonal antibody; PAT, process analytical technologies; VI, viral inactivation.

phosphate solution, pH 6.8. A cleaning-in-place of each column was performed with 1 M NaOH.

2.3.2 | Process setup

The developed system configuration for the implementation of the microfluidic chip in an ÄKTA Avant unit is shown in Figure 2. Pump A was used for the equilibration, elution, and stripping buffers and Pump B was mainly employed for the in-line conditioning buffers. The sample pump was applied to inject the FD into the micromixer structure, passing through the InjV (Figure 2, dashed gold line). The four VVs were used to guide the flow path and to incorporate the two 50 mL superloops in the system. The VI step was performed in superloop 1 (Figure 2, dark blue line). For the remaining process steps, the two superloops independently collected the eluate from

TABLE 1 Buffers used in the integrated downstream set-up experiments.

		Buffer
	Initial sample	50 mM NaOAc + 100 mM NaCl, pH 5.0
VI	Incubation	37.5 mM NaOAc + 75 mM NaCl, pH 3.0
CEX	Equilibration	50 mM NaOAc + 60 mM NaCl, pH 5.0
	Elution	50 mM NaOAc + 240 mM NaCl, pH 5.0
	Stripping	50 mM NaOAc + 500 mM NaCl, pH 5.0
AEX	Equilibration	25 mM NaOAc + 25 mM Na-Pb + 120 mM NaCl, pH 6.2
	Stripping	37.5 mM NaOAc + 75 mM NaCl, pH 3.0

Note: NaOAc corresponds to sodium acetate, Na-Pb to sodium phosphate, and NaCl to sodium chloride.

Abbreviations: AEX, anion exchange; CEX, cation exchange; VI, viral inactivation.

the CEX column, and the FT and the eluate of the AEX column. These samples were shortly stored in superloops 1 or 2 to be later sent to the micromixer channel for aggregate detection. Another particularity of the developed setup was the addition of three different restrictors. By adding these restrictors, the overall process pressure was maintained which was crucial to preserve the integrity of the microfluidic mixer. The LoopV contained the two chromatographic columns and the 10 mL superloop, from where the mAb sample was injected to start the process (superloop 0). The ColV was used as a versatile valve, guiding the flow path and allowing the connection to the two 50 mL superloops. By switching the ColV position, the superloops could either be filled (Figure 2, dark blue line) or emptied (Figure 2, dashed gold line). The OutV was utilized in the sampling of what was collected in the superloop and not further injected in the next step. For example, the FT of the AEX column, that is, the mAb purified product, the stripping of the CEX column and the elution of the AEX column were collected and later analyzed off-line to determine the level of aggregation. The flow paths for remaining phases, such as the CEX column equilibration and elution, are represented in Supporting Information: Figure S1 for a better understanding of the process set-up.

Additionally, two separate UV monitors were employed in this system: UV1, a U9-M monitor able to measure up to three wavelengths; and UV2, a U9-L detector, able to measure only one wavelength. UV1 was placed after the micromixer, to be able to detect aggregation due to the increase in UV absorbance; and UV2, at 280 nm, monitored the chromatographic run, placed after the VV2. The pH and conductivity sensor were also placed after UV2 to monitor the chromatography process.

2.3.3 | Micromixer implementation

The micromixer provides around 90% of mixing efficiency when both streams are simultaneously pumped into the structure at 1 µL min^{-1} (São Pedro et al., 2022). Due to the ÄKTA's inherent pump limitations for lower flows, a flow rate of 3 µL min^{-1} (0.003 mL min^{-1}) was used, which still provided a high mixing efficiency, of around 85%, determined according to São Pedro et al. (2023). With the incorporation of the two 50 mL superloops, this reduction of pump A's flow rate to 3 µL min^{-1} for aggregate detection in the micromixer could be achieved.

To implement the FD-based PAT tool in an ÄKTA unit, several challenges had to be tackled to enable a fast analytical measurement, under 10 min: (1) by placing the micromixer close to the InlS valve (Supporting Information: Figure S2), the volume of the connection tubes, was reduced as much as possible; (2) before the analytical measurement was started, the connection tubes were filled with sample; (3) to clean and remove any remaining sample or FD, the connection tubes and micromixer were flushed with water at a flow rate of 5 µL min^{-1} after each aggregate detection (Supporting Information: Figure S3); and, finally, (4) to eliminate any interference from the FD's intrinsic fluorescence, before the measurement, the UV signal was auto-zeroed with FD and sample buffer in the micromixer. Regarding the wavelengths used in UV1 for aggregate detection, for the FD CCVJ, the selected excitation wavelength (λ_{exc}) was of 435 nm and the emission wavelength (λ_{em}) of 520 nm. For the FD Bis-ANS, the selected λ_{exc} was of 385 nm and the λ_{em} of 520 nm (São Pedro et al., 2023).

2.3.4 | Process control

The ÄKTA systems are normally controlled by the Unicorn software. However, the Unicorn software has several limitations as, for example, operating an ÄKTA system with customized flow paths or introducing process control features. The Orbit software, written in Python, was developed at the department of Chemical Engineering, Lund University. With Orbit, direct communication and control of ÄKTA equipment is enabled via two different protocols (OPC and REST API), and customized control strategies can be implemented, thus overcoming these limitations. In this work, the ÄKTA Avant was controlled via Orbit and a pooling control strategy was implemented: the pooling cut-off times of the collection of the FT and eluate pools of the polishing steps in both 50 mL superloops were based on the UV absorbance at a wavelength of 280 nm, measured on-line by the UV2 monitor (Lofgren et al., 2018). More information on Orbit and how the controller functions can be found in Gomis-Fons et al. (2019) and Löfgren et al. (2021), with several examples on its use described elsewhere (Gomis-Fons, Schwarz, et al., 2020; Moreno-González et al., 2021; Schwarz et al., 2022).

3 | RESULTS AND DISCUSSION

3.1 | Design of the downstream process

To assess the micromixer ability to detect the presence of HMW species in a biomanufacturing process, the final steps of the purification process of mAbs were implemented and integrated in

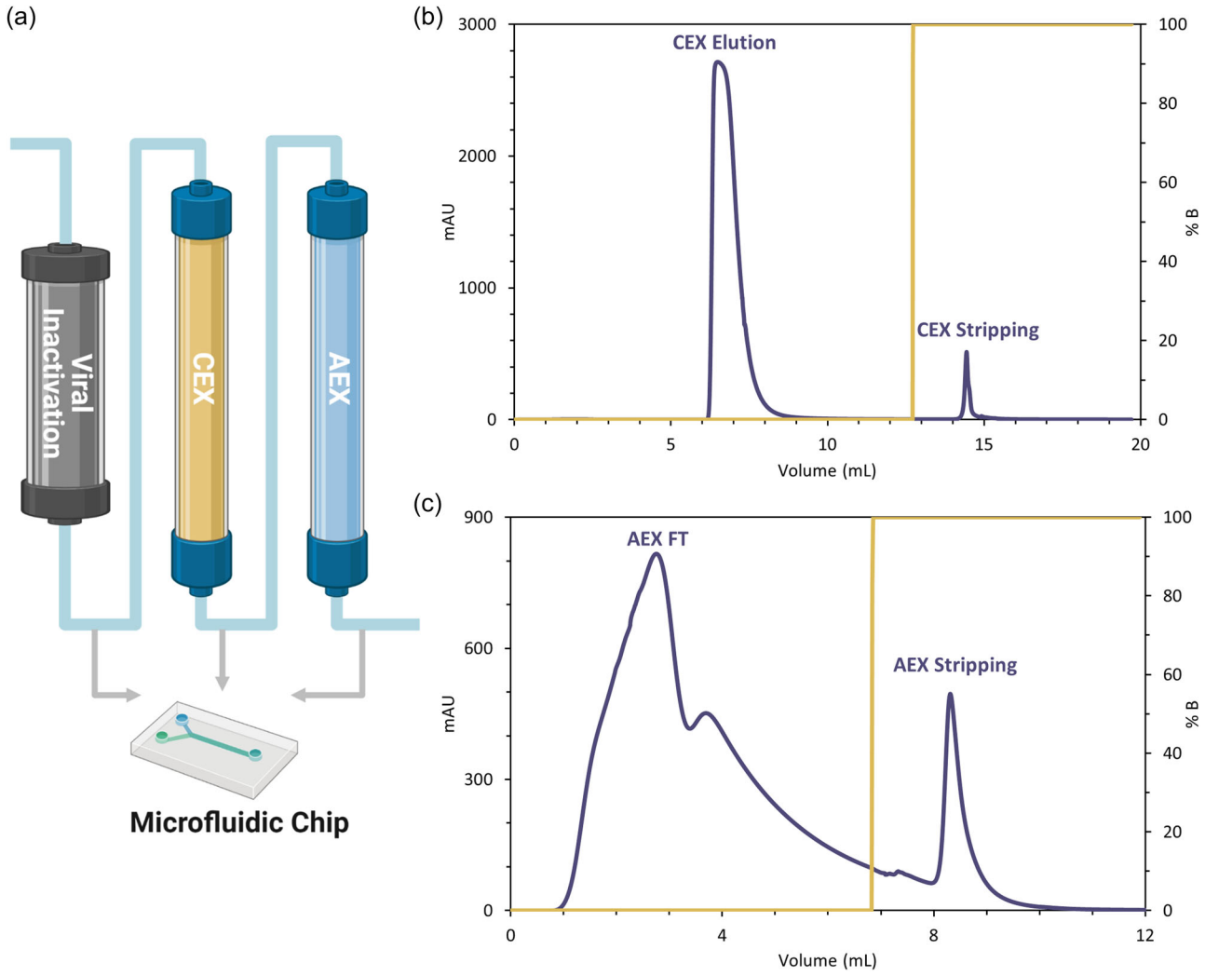

FIGURE 3 (a) Schematic representation of the unit operations implemented in the integrated downstream setup: VI, a CEX, and a AEX chromatography step. A sample of each collected phase is sent directly to the micromixer structure, where mAb aggregation is detected within 10 min. Each unit operation was optimized separately beforehand: first, the mAb sample was incubated at pH 3 for 60 min, and the resulting sample was injected in a (b) CEX column, in a bind-and-elute mode; followed by a (c) AEX step, in a FT mode. The buffers employed can be found in Table 1, the same buffers used in the integrated system. Each sample was also analyzed by SEC-UPLC to determine the aggregation level (Table 2) to confirm aggregate removal within the downstream process. AEX, anion exchange; CEX, cation exchange; FT, flow-through; mAb, monoclonal antibody; SEC, size exclusion chromatography; VI, viral inactivation.

an ÄKTA system. The main goal was to directly send a sample to the micromixer for aggregate detection (Figure 3a). However, the purification steps were first optimized separately and an early assessment of the level of aggregation was performed. Basing the experimental buffers (Table 1) and process conditions on the mAb downstream processes implemented elsewhere (GE Healthcare [2015] and Gomis-Fons, Andersson, et al. [2020]), the three unit operations were reproduced, and the volumes necessary for in-line conditioning were determined. The resulting chromatograms of the bind-and-elute CEX and FT AEX are presented in Figure 3b and c, respectively. The level of aggregation after each unit operation was determined by SEC-UPLC, and is described in Table 2. With the

TABLE 2 Aggregation levels and concentration determined by SEC-UPLC for each collected sample from the batch optimization experiments.

	Aggregation (%)	Concentration (mg mL^{-1})
Initial sample	2.7	36.5
VI incubation	2.8	28.7
CEX stripping	3.2	11.6
AEX FT	0.1	2.0
AEX stripping	13.8	0.4

Abbreviations: AEX, anion exchange; CEX, cation exchange; FT, flow-through; SEC, size exclusion chromatography; VI, viral inactivation.

optimization of each step, the elimination of HMW species was accomplished, with the final mAb product containing merely 0.1% of aggregation. Therefore, the designed integrated process is expected to efficiently remove the aggregates, and the developed PAT tool should only detect aggregation in the VI and the CEX steps, but not in the AEX FT, the final purified product.

3.2 | Implementation of micromixer in the downstream process

The next step was to incorporate and integrate all the steps in an ÄKTA Avant unit, with the implementation of the PAT microfluidic chip (Figure 2, Supporting Information: Figures S1 and S3). Several extra modules were added to a standard ÄKTA unit: a LoopV, four VVs, one extra UV monitor, and three superloops, one of 10 mL and two 50 mL. The function of each additional module is extensively described in Section 2.3.2. The microfluidic chip was operated at a flow rate of 3 µL min^{-1} (0.003 mL min^{-1}), which provided a mixing efficiency of around 85% (São Pedro et al., 2023). Pump A and sample pump inject the sample and the FD into the micromixer, respectively. The incorporation of two superloops in the system was crucial since it allowed to perform not only the VI step, but also to collect the eluate from the CEX column, as well as the FT and the eluate of the AEX column. Thus, the mAb samples could be stored and later directly sent to the micromixer to detect the presence of HMW species (Figure 2, dashed gold line), using a reduced pump A's flow rate. Additionally, with the addition of three restrictors, the system's pressure could be maintained, without the presence of any pressure spikes which could damage the integrity of micromixer or cause the disconnection of the tubes to the micromixer. Thus, a single microfluidic chip could be constantly reused for every measurement performed.

The micromixer was previously validated to successfully detect aggregation in an FT AEX unit operation (São Pedro et al., 2023). However, the detection time, starting with the pumping of the sample to be mixed with the FD and finishing with forwarding the mixed fluid to the UV sensor, took a total of 60 min. Hence, since the micromixer was not able to provide a real-time measurement, a major challenge when integrating this microfluidic sensor was to significantly reduce this detection time. Several design measures and procedures were implemented to decrease this measuring time to merely 10 min, explained in detail in Section 2.3.3. Rathore et al. (2008) used an online-HPLC system to perform pooling of a chromatography column based on product CQAs, like aggregation. The time of analysis in the HPLC was reduced to 11 min, allowing for a real-time decision making for the chromatographic pooling. Therefore, the measuring time of the PAT micromixer was aimed to be reduced to the 10 min mark. Furthermore, to eliminate any interference from the FD's intrinsic fluorescence, the UV signal was auto-zeroed with the injection of FD and the sample buffer in the micromixer before the measurement.

3.3 | Aggregate detection

With the process set up in the ÄKTA system, the final mAb purification steps were reproduced and, after each phase, a sample was directly sent to the developed PAT tool for aggregate detection. First, resorting to the viscosity-sensitive FD CCVJ, a run was performed in the integrated downstream process and the results can be found in Figure 4. The UV signal at 280 nm (dark blue line) was recorded by UV2, controlling the process, whereas the UV signal at 520 nm (dashed gold line) was recorded by UV1. The UV signal at 520 nm was defined to monitor the λ_{em} of the FD CCVJ, meaning that when there was an increase in absorbance, aggregation was present in the analyzed sample. Once more, off-line SEC-UPLC was performed to confirm and determine the level of aggregation of the collected samples which were not loaded into the next purification step (Table 3).

The integrated run started with the cleaning of the micromixer and connection tubes. Afterwards, the mAb sample was injected from the 10 mL superloop 0 to the 50 mL superloop 1, loading the VI step (Figure 2, dark blue line). Since the injection of the mAb sample required the passage through the UV2 detector, the first peak observed at 280 nm in Figure 4 corresponds to this VI loading. During the VI loading, pump B performed sample conditioning by in-line dilution, lowering the mAb pH solution from 5.0 to 3.0. The sample was incubated for 60 min, while the equilibration of the CEX and AEX columns were taking place. After the VI step, a mAb sample was directly sent to the microfluidic sensor for aggregate detection (Figure 2, dashed gold line). A significant increase in the UV absorbance at 520 nm can be observed (Figure 4), which means HMW species are present in the mAb sample. Then, a bind-and-elute CEX was performed, with the eluate also being analyzed in the micromixer. Once again, an increase in the UV signal at 520 nm can be detected, which means that the first polishing step does not completely remove all HMW species present. Subsequently, the CEX eluate was loaded onto the AEX column and the FT was collected for aggregate analysis. Surprisingly, the microfluidic sensor detected HMW species in the AEX FT, that is, the final purified product, which was not expected since the process was optimized for aggregate removal. The off-line analysis by SEC-UPLC revealed that the mAb final product still contained 0.9% of aggregation (Table 3). Hence, the FD CCVJ can detect aggregation in samples containing as low as 1% of HMW species. Nevertheless, aggregate detection using FDs is more related to the properties of the aggregates than actually their amount (Hawe et al., 2008). Therefore, FDs will only provide a qualitative measurement, not quantitative, and an absolute value for its limit of detection (LOD) should not be defined. Later, the AEX column was stripped and the sample pool was sent for aggregate detection and posterior off-line analysis. The micromixer was not able to detect aggregation, which could not be confirmed by the SEC-UPLC analysis since not enough volume was collected. A possible explanation is, since a larger percentage of aggregation was encountered in the mAb product, the absence of a signal in UV1 from the AEX strip sample is due to a poor separation of the HMW

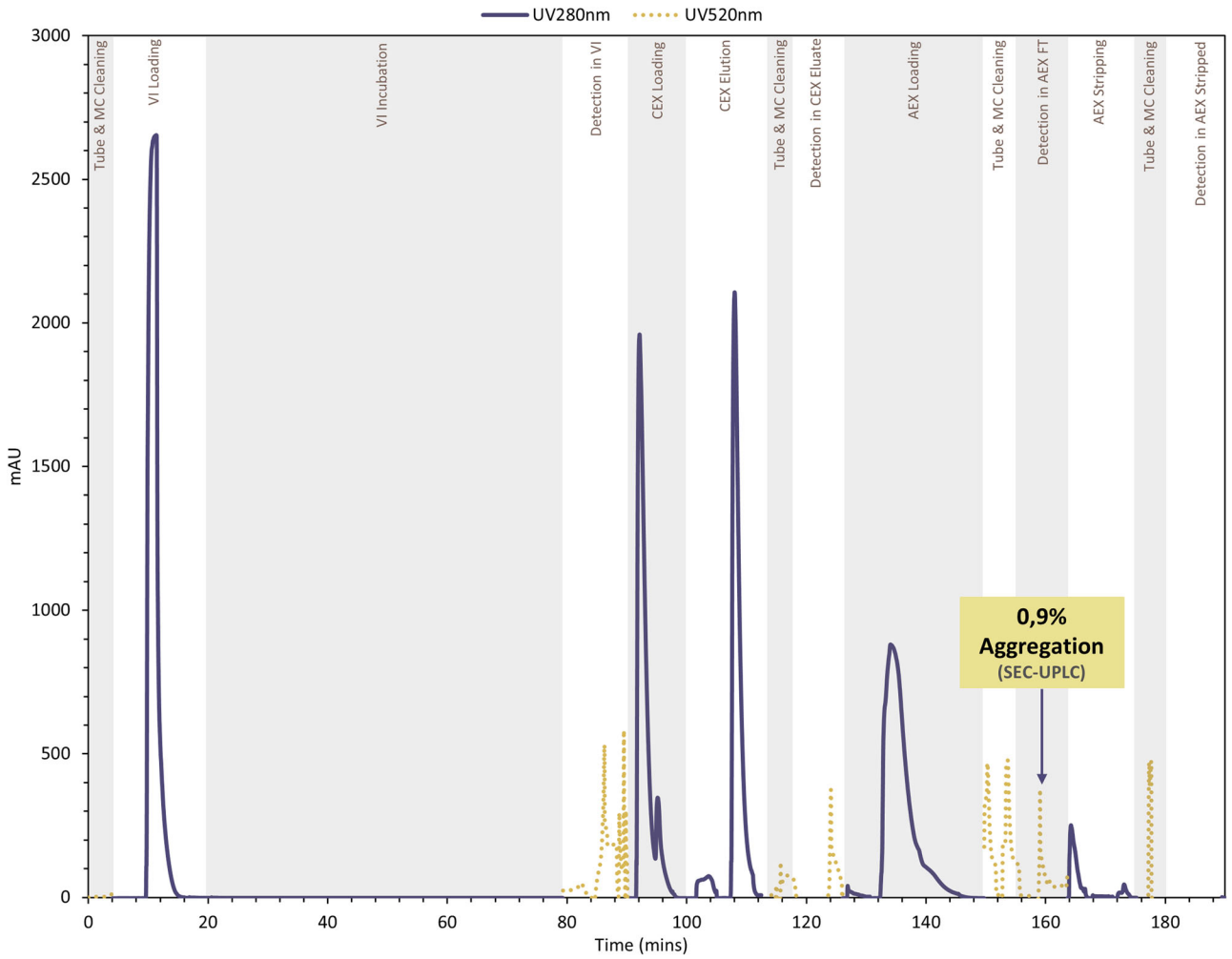

FIGURE 4 Chromatographic profile for a single run in the integrated downstream set-up: VI, CEX, and AEX, with CCVJ ([CCVJ] = 1 μM, λ_{exc} = 435 nm, λ_{em} = 520 nm) as the fluorescent dye (FD) used for detection. The mAb sample ([mAb = 40 mg mL^{-1}) first undergoes the viral inactivation step, where it is incubated at pH 3 for 60 min, followed by CEX in bind-and-elute mode and a FT AEX step. Before each measurement, the micromixer structure is cleaned with water. The UV signal at 280 nm (UV2) is used to monitor the chromatography run whereas the UV signal at 520 nm (UV1) is employed for aggregate detection. The UV1 signal was autozeroed with buffer and FD in the micromixer before each analysis. The examined samples in the microfluidic structure were also analyzed by SEC-UPLC to determine the aggregation level (Table 3). AEX, anion exchange; CEX, cation exchange; FT, flow-through; mAb, monoclonal antibody; VI, viral inactivation.

TABLE 3 Aggregation levels and concentration determined by SEC-UPLC for each collected sample from the integrated downstream runs, for the fluorescent dyes CCVJ ([CCVJ] = 1 μM, λ_{exc} = 435 nm, λ_{em} = 520 nm) and Bis-ANS ([Bis-ANS] = 0.5 μM, λ_{exc} = 380 nm, λ_{em} = 520 nm).

	CCVJ		Bis-ANS	
	Aggregation (%)	Concentration (mg mL^{-1})	Aggregation (%)	Concentration (mg mL^{-1})
Initial sample	4.8	39.3	5.2	40.6
CEX FT	ND	0	ND	0
CEX stripping	32.9	2.4	31.1	3.3
AEX FT	0.9	0.6	0.6	0.6
AEX stripping	-		ND	0

Note: The AEX stripped sample collected was not enough to be analyzed by SEC-UPLC in the CCVJ run. The CEX FT and the AEX Stripping sample for the Bis-ANS run did not contain mAb sample, therefore aggregation was not detected (ND).

Abbreviations: AEX, anion exchange; CEX, cation exchange; FT, flow-through; mAb, monoclonal antibody; SEC, size exclusion chromatography.

species in the final polishing step. Additionally, the AEX strip sample might be too diluted for the FD CCVJ being able to detect aggregation. Since sample collection in each of the superloops is controlled by the UV signal at 280 nm provided by the UV2 monitor, the shortage of volume collected from the stripping of the AEX column already indicated a very diluted sample (Table 3). Nonetheless, the micromixer was successfully implemented and applied, detecting aggregation where HMW species were indeed present during the mAb purification process.

Furthermore, the micromixer sensor was also tested with the hydrophobicity sensitive FD Bis-ANS. The results are described in Figure 5, with the off-line analysis by SEC-UPLC being found in Table 3. An identical process was performed, starting with the VI step and followed by the two polishing steps. Similarly to CCVJ, an increase in the UV signal at 520 nm is observed in the VI and CEX eluate samples. Hence, aggregation was effectively detected by the micromixer once more. However, for the AEX FT, the UV absorbance never increased during the 10 min measuring time. Consequently, aggregation was not detected in the mAb final product, which was later analyzed off-line. The mAb final product contained merely 0.5% of aggregates, which was not detected by the FD Bis-ANS. The regulatory guidelines provided by the United States and the European Pharmacopeia recommend that the mAb final formulation has to be "practically/essentially free" of insoluble aggregates (100 nm to 100 µm), which have been reported to cause immunogenicity (van Beers & Bardor, 2012; den Engelsman et al., 2011). Even though the size of these aggregates would still need to be assessed, 0.5% of aggregation on the final mAb formulation can be considerable acceptable (if the HMW species present are mainly reversible soluble aggregates). Therefore, Bis-ANS can be an ideal choice to be employed in the mAb purification process since it only provides an increase of the UV signal at 520 nm for samples with around 2% of aggregation (São Pedro et al., 2023). Additionally, for the stripping of the AEX column, the micromixer was able to effectively detect aggregation, which was expected (Table 2). Once more, the developed miniaturized PAT tool, using Bis-ANS, successfully detected aggregation in an integrated downstream process. Thus, the FD can be chosen with respect to the maximum recommended

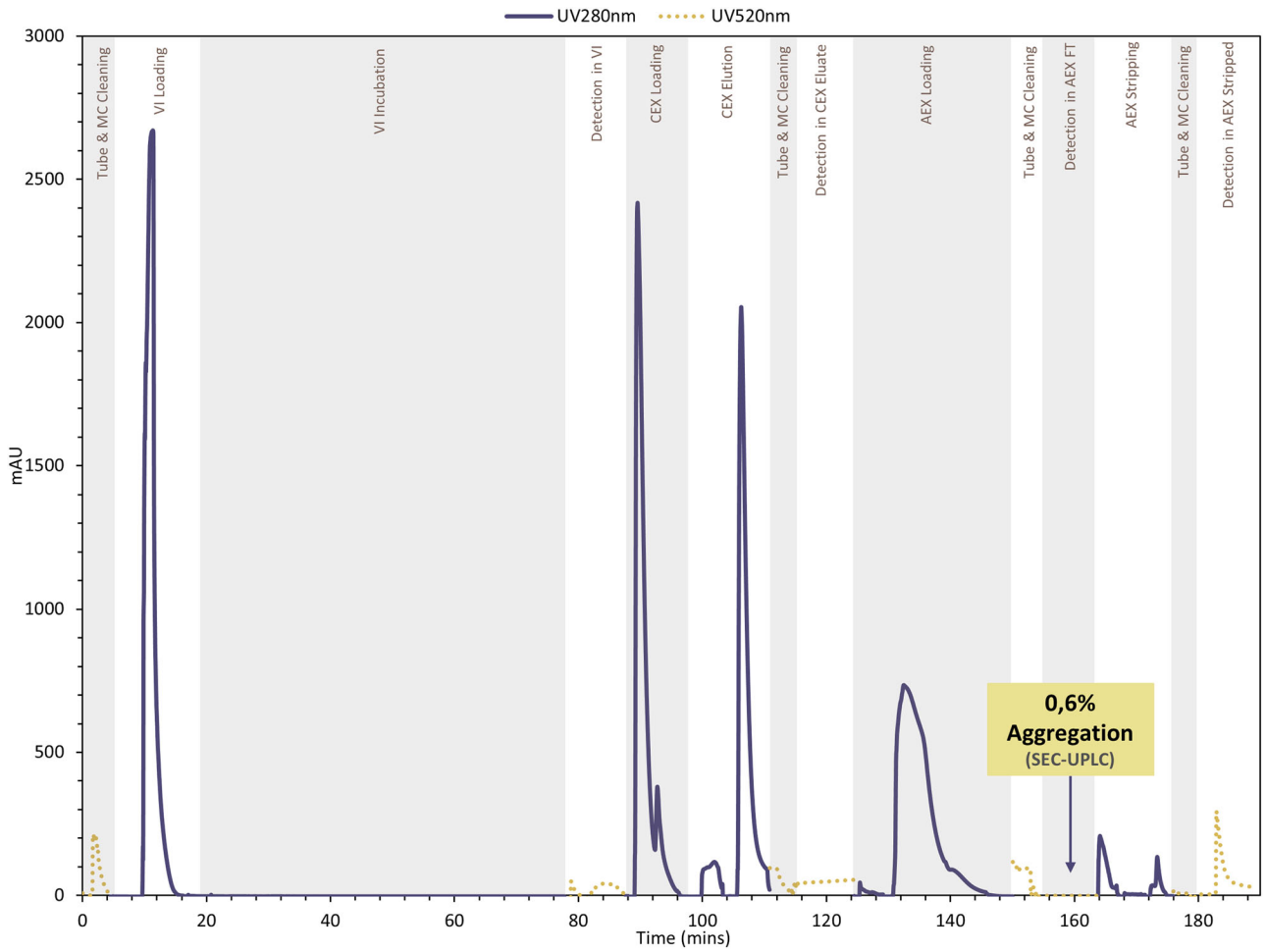

FIGURE 5 Chromatographic profile for a single run in the integrated downstream set-up: VI, CEX, and AEX, with Bis-ANS ([Bis-ANS] = 0.5 µM, λ_{exc} = 380 nm, λ_{em} = 520 nm) as the fluorescent dye used for detection. The same chromatography run was performed as in Figure 4, with the examined samples in the microfluidic structure analyzed by SEC-UPLC to determine the aggregation level (Table 3). AEX, anion exchange; CEX, cation exchange; SEC, size exclusion chromatography; VI, viral inactivation.

concentration of aggregates in the final mAb formulation: the UV signal would only increase if the aggregate level is above the recommended limit.

3.4 | Potential and limitations of the micromixer

The main goal was to develop a PAT tool capable of real-time detection of aggregation in an integrated continuous downstream process. Although the miniaturized PAT tool fulfilled the requirement of detecting the presence of HMW species, this microfluidic sensor cannot be implemented in a truly continuous process. However, the majority of the implemented continuous downstream operations are actually merely semicontinuous, such as the periodic counter current chromatography. The loading of the harvest feed is performed continuously but the washing and elution of the chromatography columns is not, with a discontinuous output of material. Therefore, the developed PAT micromixer could still be easily implemented.

Due to the inherent low flow rates employed in the micromixer, the addition of two superloops was essential to store the product pools. A reduction to lower flow rates, while using the ÄKTA system pumps, could be achieved without jeopardizing the entire purification process. Although the ÄKTA's pumps can technically employ these low flow rates, the entrance of air bubbles could be observed as not enough back pressure was generated. In Figure 4, a sudden increase in the UV signal at 520 nm can be seen at the start of every measurement. The presence of air bubbles result in these oscillations in the UV signal, which might affect the stability of the aggregation measurement. These air bubbles are primarily caused by switching of valve positions and thus flow paths, and the pump's limitation for lower flow rates, making their appearance unavoidable. For example, the sudden peak observed in the tube cleaning before the AEX stripped pool (Figure 4) detection can be attributed to an air bubble. Nevertheless, if the UV signal ends up stabilizing, as seen for the AEX FT pool, the aggregate detection provided by the micromixer is reliable, which was later confirmed by an off-line analysis.

The LOD for this miniaturized PAT tool is directly correlated with the LOD of the FD employed. Depending on the level of aggregation allowed in the final biopharmaceutical formulation, CCVJ and Bis-ANS may be great options to be applied. Recently, several novel FDs have emerged, such as Proteostat, which seems to be better suited to detect small soluble aggregates (Oshinbolu et al., 2018). Hence, the choice of the ideal FD will be critical to produce a reliable aggregate detection and it should be selected according to the needs of removing aggregates in a specific process. Furthermore, even though this work focused on the purification of a biopharmaceutical mAb, these FDs can detect aggregation across a variety of different proteins (Bai et al., 2021; Lindgren et al., 2005; Maarschalkerweerd et al., 2011). Hence, the developed micromixer can be employed in several purification processes where protein aggregation is a CQA.

Unfortunately, a quantification of the degree of aggregation is not yet possible. Since the signal provided by the FD is directly related to the type of aggregate rather than actually its amount, a quantification cannot be achieved (Hawe et al., 2008). For example, in Figure 5, similar UV signals at 520 nm can be observed throughout the process (VI, CEX eluate, and AEX stripped sample), even though the amount of aggregates in each sample differs (Tables 2 and 3). Therefore, this microfluidic sensor is limited to offering a qualitative measurement. For aggregate quantification, the possibility of miniaturizing other analytical techniques should be examined since the developed micromixer demonstrated that its miniaturization produces a real-time measurement. Hydrodynamic chromatography and asymmetrical flow field-flow fractionation (AF4) could be powerful alternatives to be miniaturized and implemented in the developed integrated system (São Pedro, Klijn, et al., 2021).

Nevertheless, the developed PAT tool presents two major advantages when compared to other already reported analytical approaches for a real-time measure of aggregation: the sample volume collected for analysis (30 µL) is negligible, being easily implemented in several biomanufacturing steps; and, since only an extra UV monitor is necessary to perform the analytical measurement, a FD-based microfluidic sensor is a relatively affordable alternative. For example, Patel et al. (2018) created a real-time aggregation measurement by coupling a multi-angle light scattering (MALS) detector to a purification unit. Even though an immediate and in-line measurement is achieved, the cost associated to a MALS detector make this technique not readily available in a biomanufacturing site. Other analytical techniques pose a similar challenge, with an extra and complicated external set-up required to perform the measurement which increases production costs: Raman spectrometry (Yilmaz et al., 2020), near-infrared spectroscopy (Thakur et al., 2020), and light scattering (Rolinger et al., 2020).

4 | CONCLUDING REMARKS

A PAT FD-based microfluidic sensor was successfully implemented in an integrated downstream process, and it was capable of detecting aggregation after each unit operation. First, the final steps in the integrated downstream process for the purification of mAbs, composed of the VI and two polishing steps, were optimized separately for aggregate removal. Then, to implement the previously developed micromixer, an integrated downstream system was developed in an ÄKTA system. A sample was directly sent for aggregate analysis after each step in the purification chain. By adding two superloops and one extra UV sensor, the implementation of the microfluidic sensor was achieved: the two superloops allowed the collection of the mAb samples to be sent for analysis, reducing the flow rate; while the extra UV sensor permitted the monitoring of the chromatographic run while the already existing UV was used for the aggregation measurement. Additionally, several strategies were employed to reduce the measuring time of the microsensor from 60 to 10 min, such as reducing the connection tubes length or filling them with sample/FD beforehand. The microfluidic sensor effectively and robustly detected aggregation when using two distinct FDs, CCVJ, and Bis-ANS, which was later confirmed off-line. Depending on the regulatory

guidelines for the presence of aggregate in the final formulation of the mAb, a more (CCVJ) or less (Bis-ANS) sensitive FD can be selected to detect aggregation in the micromixer.

Although the developed PAT tool cannot produce a quantifiably measurement of the level of aggregation, the microfluidic chip does allow a rapid detection of HMW species. With the implementation in the integrated system, a real-time measurement was achieved, even under the desired 10 min. Therefore, the miniaturization of the analytical technique effectively speeds up the measurement. With the ability to measure real-time CQAs, immediate feedback and control of the process parameters can be achieved. For example, while performing the measurement, a control strategy can be implemented if an increase in the UV signal at 520 nm occurs.

ACKNOWLEDGMENTS

The authors wish to thank the European Union's Horizon 2020 research and innovation programme under the Marie Skłodowska-Curie grant agreement No 812909 CODOBIO, within the Marie Skłodowska-Curie European Training Networks framework.

CONFLICT OF INTEREST STATEMENT

The authors declare no conflict of interest.

DATA AVAILABILITY STATEMENT

The data that support the findings of this study are available from the corresponding author upon reasonable request.

ORCID

Mariana N. São Pedro http://orcid.org/0000-0002-1801-9629

Bernt Nilsson http://orcid.org/0000-0003-3568-7706

REFERENCES

Bai, Y., Wan, W., Huang, Y., Jin, W., Lyu, H., Xia, Q., Dong, X., Gao, Z., & Liu, Y. (2021). Quantitative interrogation of protein co-aggregation using multi-color fluorogenic protein aggregation sensors. *Chemical Science*, *12*(24), 8468–8476. https://doi.org/10.1039/d1sc01122g

Bansal, R., Gupta, S., & Rathore, A. S. (2019). Analytical platform for monitoring aggregation of monoclonal antibody therapeutics. *Pharmaceutical Research*, *36*(11), 152. https://doi.org/10.1007/s11095-019-2690-8

Chopda, V., Gyorgypal, A., Yang, O., Singh, R., Ramachandran, R., Zhang, H., Tsilomelekis, G., Chundawat, S. P. S., & Ierapetritou, M. G. (2021). Recent advances in integrated process analytical techniques, modeling, and control strategies to enable continuous biomanufacturing of monoclonal antibodies. *Journal of Chemical Technology & Biotechnology*, *97*(9), 2317–2335. https://doi.org/10.1002/jctb.6765

den Engelsman, J., Garidel, P., Smulders, R., Koll, H., Smith, B., Bassarab, S., Seidl, A., Hainzl, O., & Jiskoot, W. (2011). Strategies for the assessment of protein aggregates in pharmaceutical biotech product development. *Pharmaceutical Research*, *28*(4), 920–933. https://doi.org/10.1007/s11095-010-0297-1

Gökaltun, A., Kang, Y. B., Yarmush, M. L., Usta, O. B., & Asatekin, A. (2019). Simple surface modification of poly(dimethylsiloxane) via surface segregating smart polymers for biomicrofluidics. *Scientific Reports*, *9*(1), 7377. https://doi.org/10.1038/s41598-019-43625-5

Gomis-Fons, J., Andersson, N., & Nilsson, B. (2020). Optimization study on periodic counter-current chromatography integrated in a monoclonal antibody downstream process. *Journal of Chromatography A*, *1621*, 461055. https://doi.org/10.1016/j.chroma.2020.461055

Gomis-Fons, J., Löfgren, A., Andersson, N., Nilsson, B., Berghard, L., & Wood, S. (2019). Integration of a complete downstream process for the automated lab-scale production of a recombinant protein. *Journal of Biotechnology*, *301*, 45–51. https://doi.org/10.1016/j.jbiotec.2019.05.013

Gomis-Fons, J., Schwarz, H., Zhang, L., Andersson, N., Nilsson, B., Castan, A., Solbrand, A., Stevenson, J., & Chotteau, V. (2020). Model-based design and control of a small-scale integrated continuous end-to-end mAb platform. *Biotechnology Progress*, *36*(4), e2995. https://doi.org/10.1002/btpr.2995

Hawe, A., Friess, W., Sutter, M., & Jiskoot, W. (2008). Online fluorescent dye detection method for the characterization of immunoglobulin G aggregation by size exclusion chromatography and asymmetrical flow field flow fractionation. *Analytical Biochemistry*, *378*(2), 115–122. https://doi.org/10.1016/j.ab.2008.03.050

Healthcare, G. (2015). Continuous chromatography, downstream processing of a monoclonal antibody. 2015 Report 29170800 AA.

He, F., Phan, D. H., Hogan, S., Bailey, R., Becker, G. W., Narhi, L. O., & Razinkov, V. I. (2010). Detection of IgG aggregation by a high throughput method based on extrinsic fluorescence. *Journal of Pharmaceutical Sciences*, *99*(6), 2598–2608. https://doi.org/10.1002/jps.22036

Lindgren, M., Sörgjerd, K., & Hammarström, P. (2005). Detection and characterization of aggregates, prefibrillar amyloidogenic oligomers, and protofibrils using fluorescence spectroscopy. *Biophysical Journal*, *88*(6), 4200–4212. https://doi.org/10.1529/biophysj.104.049700

Löfgren, A., Andersson, N., Sellberg, A., Nilsson, B., Löfgren, M., & Wood, S. (2018). Designing an autonomous integrated downstream sequence from a batch separation process—An industrial case study. *Biotechnology Journal*, *13*(4), 1700691. https://doi.org/10.1002/biot.201700691

Löfgren, A., Gomis-Fons, J., Andersson, N., Nilsson, B., Berghard, L., & Lagerquist Hägglund, C. (2021). An integrated continuous downstream process with real-time control: A case study with periodic countercurrent chromatography and continuous virus inactivation. *Biotechnology and Bioengineering*, *118*(4), 1645–1657. https://doi.org/10.1002/bit.27681

Maarschalkerweerd, A., Wolbink, G.-J., Stapel, S. O., Jiskoot, W., & Hawe, A. (2011). Comparison of analytical methods to detect instability of etanercept during thermal stress testing. *European Journal of Pharmaceutics and Biopharmaceutics*, *78*(2), 213–221. https://doi.org/10.1016/j.ejpb.2011.01.012

Mandenius, C.-F., & Gustavsson, R. (2015). Mini-review: Soft sensors as means for PAT in the manufacture of bio-therapeutics. *Journal of Chemical Technology & Biotechnology*, *90*(2), 215–227. https://doi.org/10.1002/jctb.4477

Moreno-González, M., Keulen, D., Gomis-Fons, J., Gomez, G. L., Nilsson, B., & Ottens, M. (2021). Continuous adsorption in food industry: The recovery of sinapic acid from rapeseed meal extract. *Separation and Purification Technology*, *254*, 117403. https://doi.org/10.1016/j.seppur.2020.117403

Oshinbolu, S., Shah, R., Finka, G., Molloy, M., Uden, M., & Bracewell, D. G. (2018). Evaluation of fluorescent dyes to measure protein aggregation within mammalian cell culture supernatants. *Journal of Chemical Technology & Biotechnology*, *93*(3), 909–917. https://doi.org/10.1002/jctb.5519

Patel, B. A., Gospodarek, A., Larkin, M., Kenrick, S. A., Haverick, M. A., Tugcu, N., Brower, M. A., & Richardson, D. D. (2018). Multi-angle light scattering as a process analytical technology measuring real-time molecular weight for downstream process control. *mAbs*, *10*(7), 1–6. https://doi.org/10.1080/19420862.2018.1505178

Paul, A. J., Bickel, F., Röhm, M., Hospach, L., Halder, B., Rettich, N., Handrick, R., Herold, E. M., Kiefer, H., & Hesse, F. (2017). High-

throughput analysis of sub-visible mAb aggregate particles using automated fluorescence microscopy imaging. *Analytical and Bioanalytical Chemistry*, *409*(17), 4149–4156. https://doi.org/10.1007/s00216-017-0362-2

Rathore, A. S., Yu, M., Yeboah, S., & Sharma, A. (2008). Case study and application of process analytical technology (PAT) towards bioprocessing: Use of on-line high-performance liquid chromatography (HPLC) for making real-time pooling decisions for process chromatography. *Biotechnology and Bioengineering*, *100*(2), 306–316. https://doi.org/10.1002/bit.21759

Rolinger, L., Rüdt, M., Diehm, J., Chow-Hubbertz, J., Heitmann, M., Schleper, S., & Hubbuch, J. (2020). Multi-attribute PAT for UF/DF of proteins-monitoring concentration, particle sizes, and buffer exchange. *Analytical and Bioanalytical Chemistry*, *412*(9), 2123–2136. https://doi.org/10.1007/s00216-019-02318-8

São Pedro, M. N., Eppink, M. H. M., & Ottens, M. (2023). Application of a fluorescent dye-based microfluidic sensor forreal-time detection of mAb aggregates. *Biotechnology Progress*. https://doi.org/10.1002/btpr.3355

São Pedro, M. N., Klijn, M. E., Eppink, M. H. M., & Ottens, M. (2021). Process analytical technique (PAT) miniaturization for monoclonal antibody aggregate detection in continuous downstream processing. *Journal of Chemical Technology & Biotechnology*, *97*(9), 2347–2364. https://doi.org/10.1002/jctb.6920

São Pedro, M. N., Santos, M. S., Eppink, M. H. M., & Ottens, M. (2022). Design of a microfluidic mixer channel: First steps into creating a fluorescent dye-based biosensor for mAb aggregate detection. *Biotechnology Journal*, *18*, 2200332. https://doi.org/10.1002/biot.202200332

São Pedro, M. N., Silva, T. C., Patil, R., & Ottens, M. (2021). White paper on high-throughput process development for integrated continuous biomanufacturing. *Biotechnology and Bioengineering*, *118*(9), 3275–3286. https://doi.org/10.1002/bit.27757

Schwarz, H., Gomis-Fons, J., Isaksson, M., Scheffel, J., Andersson, N., Andersson, A., Castan, A., Solbrand, A., Hober, S., Nilsson, B., & Chotteau, V. (2022). Integrated continuous biomanufacturing on pilot scale for acid-sensitive monoclonal antibodies. *Biotechnology and Bioengineering*, *119*(8), 2152–2166. https://doi.org/10.1002/bit.28120

Telikepalli, S. N., Kumru, O. S., Kalonia, C., Esfandiary, R., Joshi, S. B., Middaugh, C. R., & Volkin, D. B. (2014). Structural characterization of IgG1 mAb aggregates and particles generated under various stress conditions. *Journal of Pharmaceutical Sciences*, *103*(3), 796–809. https://doi.org/10.1002/jps.23839

Thakur, G., Hebbi, V., & Rathore, A. S. (2020). An NIR-based PAT approach for real-time control of loading in Protein A chromatography in continuous manufacturing of monoclonal antibodies. *Biotechnology and Bioengineering*, *117*(3), 673–686. https://doi.org/10.1002/bit.27236

van Beers, M. M. C., & Bardor, M. (2012). Minimizing immunogenicity of biopharmaceuticals by controlling critical quality attributes of proteins. *Biotechnology Journal*, *7*(12), 1473–1484. https://doi.org/10.1002/biot.201200065

Wälchli, R., Ressurreição, M., Vogg, S., Feidl, F., Angelo, J., Xu, X., Ghose, S., Jian Li, Z., Le Saoût, X., Souquet, J., Broly, H., & Morbidelli, M. (2020). Understanding mAb aggregation during low pH viral inactivation and subsequent neutralization. *Biotechnology and Bioengineering*, *117*(3), 687–700. https://doi.org/10.1002/bit.27237

Yilmaz, D., Mehdizadeh, H., Navarro, D., Shehzad, A., O'Connor, M., & McCormick, P. (2020). Application of Raman spectroscopy in monoclonal antibody producing continuous systems for downstream process intensification. *Biotechnology Progress*, *36*(3), e2947. https://doi.org/10.1002/btpr.2947

SUPPORTING INFORMATION

Additional supporting information can be found online in the Supporting Information section at the end of this article.

Received: 21 March 2023 | Revised: 24 April 2023 | Accepted: 27 April 2023

DOI: 10.1002/btpr.3355

BIOTECHNOLOGY PROGRESS

RESEARCH ARTICLE

Bioseparations and Downstream Processing

Application of a fluorescent dye-based microfluidic sensor for real-time detection of mAb aggregates

Mariana N. São Pedro[1] | Michel H. M. Eppink[2,3] | Marcel Ottens[1]

[1]Department of Biotechnology, Delft University of Technology, Delft, The Netherlands

[2]Byondis B.V., Nijmegen, The Netherlands

[3]Bioprocessing Engineering, Wageningen University, Wageningen, The Netherlands

Correspondence
Marcel Ottens, Department of Biotechnology, Delft University of Technology, Van der Maasweg 9, Delft, 2629 HZ, The Netherlands.
Email: m.ottens@tudelft.nl

Funding information
CODOBIO, Grant/Award Number: 812909

Abstract

The lack of process analytical technologies able to provide real-time information and process control over a biopharmaceutical process has long impaired the transition to continuous biomanufacturing. For the monoclonal antibody (mAb) production, aggregate formation is a major critical quality attribute (CQA) with several known process parameters (i.e., protein concentration and agitation) influencing this phenomenon. The development of a real-time tool to monitor aggregate formation is then crucial to gain control and achieve a continuous processing. Due to an inherent short operation time, miniaturized biosensors placed after each step can be a powerful solution. In this work, the development of a fluorescent dye-based microfluidic sensor for fast at-line PAT is described, using fluorescent dyes to examine possible mAb size differences. A zigzag microchannel, which provides 90% of mixing efficiency under 30 s, coupled to an UV–Vis detector, and using four FDs, was studied and validated. With different generated mAb aggregation samples, the FDs Bis-ANS and CCVJ were able to robustly detect from, at least, 2.5% to 10% of aggregation. The proposed FD-based micromixer is then ultimately implemented and validated in a lab-scale purification system, demonstrating the potential of a miniaturized biosensor to speed up CQAs measurement in a continuous process.

KEYWORDS
continuous biomanufacturing, fluorescent dyes, microfluidic sensor, process analytical technology (PAT), protein aggregation

1 | INTRODUCTION

The creation of process analytical technologies (PAT) for fast analytics and control is still one of the major challenges to tackle when implementing continuous bioprocessing into biopharmaceutical processes. To elicit a response for fluctuations in operational conditions, in-line or at-line sensors need to be placed within the manufacturing process to provide a real-time measurement of product critical quality attributes (CQAs).[1] A common monitored CQA is protein aggregation, especially in the biomanufacturing of monoclonal antibodies (mAbs). Even though the presence of high molecular weight (HMW) species in the final formulation can enhance immune response, their appearance is inevitable.[2] For example, the increasing protein concentration[3] and

Abbreviations: Bis-ANS, 4-4-bis-1-phenylamino-8-naphthalene sulfonate; CCVJ9-(2-carboxy-2-cyanovinyl)julolidine; DLS, dynamic light scattering; F/T, freeze-thawing; FD, fluorescent dye; FT, flow through; HIC, hydrophobic interaction chromatography; HMW, high-molecular weight; HT, high-throughput; LoD, limit of detection; PDMS, poly (dimethylsiloxane); SEC, size exclusion chromatography; ThT, thioflavin T.

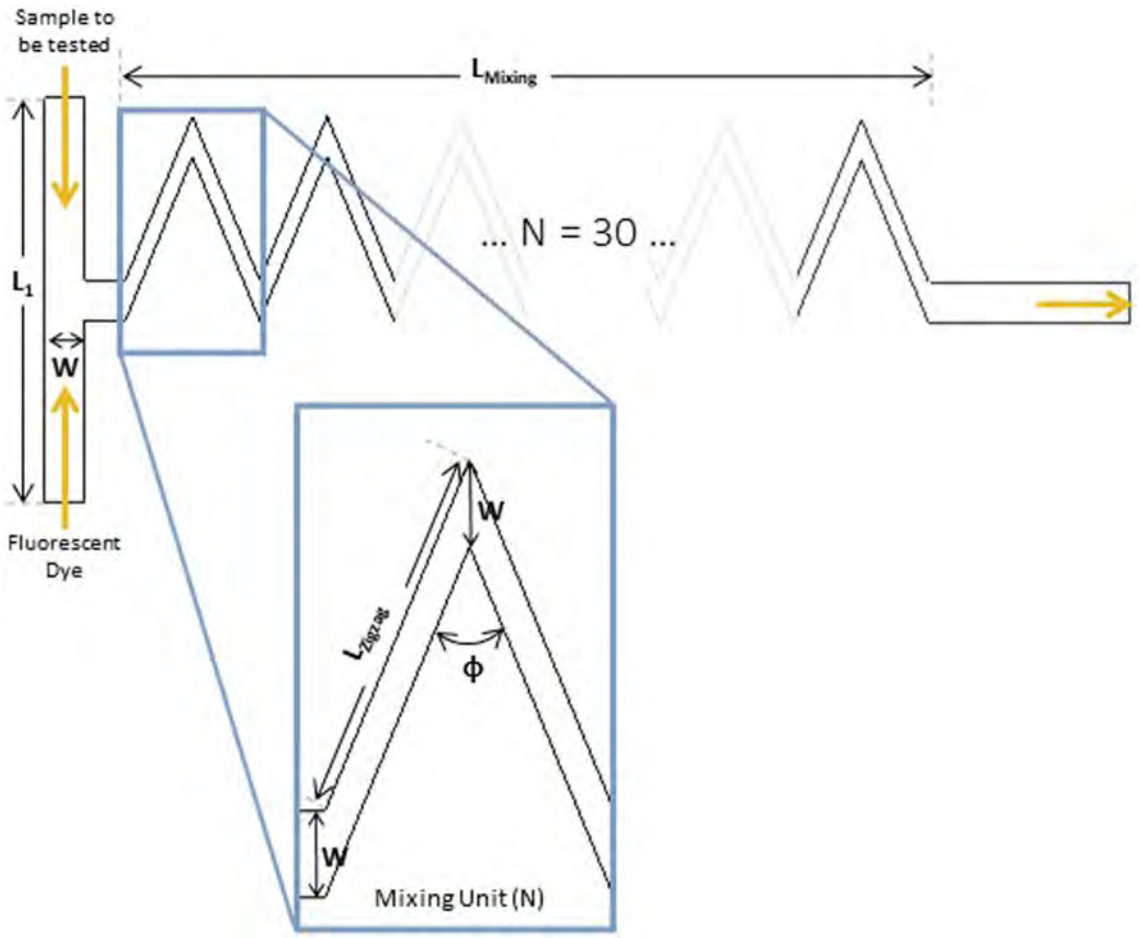

FIGURE 1 Schematic representation of the micromixer structure, with the measurement of each parameter described in Table 1. In blue, the zigzag mixing unit (N) of the micromixer is highlighted, with the structure having a total of 30 N. The orange arrows indicate the flow of both liquids entering in the two inlets and the resulting mixed liquid exiting in the outlet.

agitation[4] are known aggregation inducing factors. Hence, a PAT tool for the detection of mAb HMW species is crucial to allow to control their formation.

Fluorescent dyes (FD), such as 4-4-bis-1-phenylamino-8-naphthalene sulfonate (Bis-ANS), SYPRO Orange and Nile Red, are a widely used analytical technique to detect and study aggregation.[5,6] These dye's fluorescence intensifies (when compared to its intensity in the presence of the monomeric mAb form) in the presence of hydrophobic unfolded protein structures, a common characteristic in aggregate formation.[5] In particular, the FD Bis-ANS binds to these hydrophobic residues through hydrophobic interactions of the aromatic rings, present in its structure.[7] Additionally, a novel class of fluorescent molecular rotors, such as Thioflavin T (ThT), 9-(2-carboxy-2-cyanovinyl)julolidine (CCVJ) and Proteostat, have recently appeared as possible alternatives to the previously described classic probes. These molecular rotors rotate freely in solution and when their movement is restricted, these FDs emit fluorescence.[8,9] For example, when ThT binds to amyloid fibrils (insoluble proteinaceous materials formed during protein-misfolding events), through β-sheet-rich deposits, their FD's movement is constrained and it increases dramatically its fluorescence.[10] Since both classes provide a fast, stable and straightforward result,[11] these FDs can be taken into consideration when creating a real-time PAT tool to measure aggregation.[12] To further speed up the analytical measurement, miniaturized sensors are considered a promising solution. The inherent short operation time, the minimal amounts of sample (nL or μL) and the easiness of fabrication and affordability are major benefits provided by the implementation of a miniaturized PAT tool.[12] A zigzag microfluidic structure was designed and developed for a FD-based aggregate detection: this micromixer will then allow the mixing of a mAb sample with a FD.[13] This zigzag microchannel, represented in Figure 1 (with its geometric measurements described in Table 1) provides a mixing efficiency of around 90% within 30 s. In total, this microchannel has 30 mixing zigzag units, adding to 26.25 mm of mixing length. Additionally, due to the low shear forces, this structure is expected not to alter the amount of aggregates during the measurement and, due to the low-pressure drop, the micromixer is easy to operate and fabricate. More information on the development of this structure and its characteristics can be found in São Pedro et al.[13]

Therefore, this microfluidic structure was designed to be able to produce an immediate aggregate detection in a continuous downstream process. However, this micromixer was only experimentally validated for its mixing efficiency. The ability of the proposed structure to actually detect aggregates still needs to be assessed. In this

TABLE 1 Measurement of each geometric parameters used in the micromixer (identified in Figure 1).[13]

Parameter	Measurement
L_1	1000 μm
W	100 μm
L_{Zigzag}	440 μm
Φ	45°
L_{Mixing}	26.25 mm

Note: L_1 corresponds to the transverse length of the T-junction, W to the width of the main channel, L_{Zigzag} to the length of the zigzag channel diagonal, Φ to the angle of the zigzag channel and L_{Mixing} to the mixing length, calculated based on the number of mixing units, 30, and the length of the zigzag channel diagonally.

present work, first, a high-throughput (HT) screening of four different FDs is performed: the hydrophobic sensitive Bis-ANS and Nile Red and the molecular rotors ThT and CCVJ. The required FD concentration to be later employed in the micromixer is reached, as well as an early assessment into possible limits of detection intrinsic to each FD. After, resorting to different types of aggregates, the micromixer is used to identify aggregation using a UV–Vis detector: an increase in the UV signal is observed when aggregation is detected. Finally, the micromixer is validated in a chromatographic unit operation. Anion exchange (AEX) chromatography in an ÄKTA™ Avant unit was performed in flow-through (FT) mode to remove aggregates, with the micromixer implemented within the system. An increase in the UV signal was observed in the eluate, with the presence of aggregates later confirmed by analytical size exclusion chromatography (SEC-UPLC), while the FT (containing the product) did not produce any signal. A miniaturized FD-based PAT tool is then demonstrated, being able to robustly detect all types of aggregates which can arise in a downstream process.

2 | MATERIALS AND METHODS

Poly(dimethylsiloxane) (PDMS) was purchased as a Sylgard 184 elastomer kit (Dow Corning, Midland, MI, USA) and dimethylsiloxane-(60%–70% ethylene oxide) block copolymer was acquired from Gelest (Pennsylvania, USA). Sodium phosphate monobasic dehydrate, ammonium sulfate and sodium citrate hydrate were purchased from Sigma-Aldrich (New Jersey, USA). Di-sodium hydrogen phosphate and sodium chloride (NaCl) were bought from VWR Chemicals (VWR International, Pennsylvania, USA). Acetic acid was obtained from Fluka (Honeywell, North Carolina, USA) and citric acid from J.T. Baker (VWR International, Pennsylvania, USA). The mAb employed in this study was supplied by Byondis B.V. (Nijmegen, The Netherlands), with an isoelectric point of 8.6.

Regarding the FDs used, ThT, CCVJ and Nile Red were purchased from Sigma-Aldrich (New Jersey, USA), whereas Bis-ANS was acquired from Invitrogen (Massachusetts, USA). For the preparation of the stock solutions, the dye ThT was dissolved in MilliQ water and filtered through a 0.2 μm Whatman syringe filter (Merck, New Jersey, USA). The exact concentration was calculated from measuring the UV absorbance at 412 nm, using a molar extinction coefficient of 36,000 M^{-1} cm^{-1}.[14] Bis-ANS was dissolved in methanol (Sigma-Aldrich, New Jersey, USA) and the exact concentration calculated at 385 nm, with a molar extinction of 16,790 M^{-1} cm^{-1}.[15] Finally, CCVJ and Nile Red were dissolved in dimethyl sulfoxide (Fluka, Massachusetts, USA), and the exact concentration calculated at 440 and 552 nm, with the molar extinction of 25,404 and 19,600 M^{-1} cm^{-1}, respectively.[8]

2.1 | Stressing of mAb formulations

The provided mAb was stored at a concentration of 6 mg mL^{-1} in sodium acetate buffer, pH 4.5, at −80°C. An early characterization of this sample was performed and the presence of 4% of aggregation was detected, being referred from here on as the storage aggregates. To remove these HMW species, size exclusion chromatography (SEC) was performed on an ÄKTA™ Avant system (Cytiva, Massachusetts, USA). An HiPrep™ 16/60 Sephacryl S-300 HR column (Cytiva, USA) was used, with the elution being performed with 50 mM sodium phosphate buffer, 150 mM NaCl, pH 7.2, at a flow rate of 0.5 mL min^{-1}. The collected fraction of the purified monomer was then concentrated to 5 mg mL^{-1}, using the amicon ultra-15 centrifugal filters (Merck, New Jersey, USA).

Protein aggregation was then induced to the purified mAb solution, in 1.5 mL eppendorfs, using different types of aggregation factors such as time, temperature, low pH shift or freeze–thawing (F/T). Time aggregates were generated by storing the mAb purified sample at 4°C for, at least, 4 weeks. Temperature aggregates were induced by incubating the mAb purified sample at 75°C for 10 min, using a thermomixer (Eppendorf, Hamburg, Germany) operated at 600 rpm. Low pH shift aggregates were produced by dialyzing the mAb purified sample with 50 mM sodium citrate buffer, 500 mM NaCl, pH 3, using the amicon ultra-15 centrifugal filters. F/T aggregates were generated by incubating the purified mAb sample at −80°C for 1 h followed by thawing at 25°C. The freeze–thaw cycle was repeated five times.

2.2 | Characterization of the stressed formulations

After the different types of aggregates were generated, an initial characterization of each sample was performed using the following analytical techniques:

2.2.1 | SEC-UPLC

The mAb concentration and the percentage of aggregation of each stressed sample is determined by analytical SEC in an UltiMate 3000 UHPLC System (Thermo Fisher Scientific, Massachusetts, USA). Five microliters of sample was injected in an ACQUITY UPLC Protein BEH

SEC 200 Å column (Waters, Massachusetts, USA) and run with the 100 mM sodium phosphate buffer, pH 6.8, for 10 min. The flow rate used was 0.3 mL min^{-1} and the protein was detected at 280 nm.

2.2.2 | Hydrophobic interaction chromatography (HIC)

The hydrophobicity of each stressed formulation was assessed by HIC, according to Goyon et al.[16] A HiTrap™ Butyl FF column (CV of 1 mL), purchased from Cytiva (New Jersey, USA), was employed. An adsorption buffer of 3.5 M ammonium sulfate and 0.1 M phosphate buffer, pH 7, and an elution buffer of 0.1 M phosphate buffer, pH 7, were used. A gradient was performed from 25% to 100% of the elution buffer in 20 CV at a flow rate of 1 mL min^{-1}.

2.2.3 | Dynamic light scattering (DLS)

The presence of larger aggregates was determined by DLS, performed in Zetasizer APS with the protein size standard operating procedure (SOP) of the Zetasizer Software (Version 8.02, Malvern Panalytical, United Kingdom). One hundred microliters of each of the stressed formulations were measured in a 96-well plate at the fixed angle of 90°, at a laser wavelength of 830 nm and a temperature of 25°C. The samples were measured in triplicates and each sample was measured three times by the instrument.

2.3 | HT screening of FDs

The HT screening of the selected FDs was performed in a Tecan EVO Freedom 200 robotic station (Tecan, Switzerland), equipped with a plate reader (InfiniTe Pro 200), a robotic manipulator (RoMa) arm (to move microplates to the different positions) and one liquid handing arm (LiHa). Corning 96-well NBS™ microplate (Merck, New Jersey, USA), made of white polystyrene, were used for the measurement of the fluorescence emission spectra. From the FDs stock solutions previously prepared, several diluted FD solutions were prepared with MilliQ water, with the concentration range tested present in Table 2. Then, 100 µL of each of the generated aggregates (maintaining the concentration of 5 mg mL^{-1}) were pipetted into a well by the liquid handling robot, followed by the addition of 100 µL of the FD. Hence, a one-to-one ratio of sample to FD was used, which would be later applied in the micromixer measurements. After, the microplate is transported to the plate reader, where it is mixed at 600 rpm for 2 min and the fluorescence spectrum of each sample recorded according to the wavelengths described in Table 2. Extra blank measurements were performed where the mAb aggregate samples were replaced by buffer only. Then, the fluorescence signal recorded was subtracted from each mAb induced aggregation sample measurement to remove any buffer interference on the fluorescence signal.

TABLE 2 FDs employed in the HT screening, with the excitation and emission wavelengths used, the concentration range tested and the determined optimal concentration.

Fluorescent dye	Excitation wavelength (nm)	Emission wavelengths (nm)	Concentration range tested	Optimal concentration
ThT	415	465–600	1–5 mM	1 mM
CCVJ	435	465–650	0.5–50 µM	1 µM
Bis-ANS	380	450–600	0.5–5 µM	0.5 µM
Nile Red	550	600–750	25–100 µM	75 µM

2.4 | Aggregate detection with the micromixer

2.4.1 | Structure fabrication

The zigzag microfluidic device (100 µm high × 100 µm wide × 17.2 mm long) presents two inlets and one outlet, each 100 µm wide (Figure 1).[13] The dimensions of this micromixer are also described in Table 1. The designed mold was ordered from INESC Microsystems and Nanotechnologies (Lisbon, Portugal) and the structures were fabricated according to Gokaltun et al.[17] to reduce the inherent hydrophobicity of PDMS. Dimethylsiloxane-(60%–70% ethylene oxide) block copolymer, comprised of poly(ethylene glycol) (PEG) and PDMS segments (PDMS-PEG), were blended with PDMS during device manufacturing, using a 10:1:0.0025 mixture of PDMS, curing agent and PDMS-PEG. After being degassed, the mixture is poured onto the mold and baked at 70°C overnight. After the PDMS is cured, the chip is removed from the mold and the inlets and outlet are punched. Finally, the PDMS chip is bonded to a glass substrate and sealed with a 20:1 mixture of PDMS to curing agent.

2.4.2 | UV–Vis measurement

A syringe pump KD Scientific 200 (KD Scientific Inc, Massachusetts, USA) was used to pump both mAb sample and FD into the micromixer structure, with a flow rate of 1 µL min^{-1}. The FD concentrations used were the optimal concentrations determined in the HT screening, present in Table 2. Before starting the measurement, the UV signal is first auto-zero resorting to a solution composed of the FD with the sample buffer, with a ratio of one-to-one. The autozero is performed to eliminate any interference from the dye's intrinsic fluorescence. After the two fluids were mixed in the microstructure, the fluid is sent to an inline UV–Vis detector (SPD-20AV, Shimadzu, Kyoto, Japan) which contains a microflow cell (0.2 µL). Two wavelengths were selected to perform the measurement for each FD, taking into consideration the results previously obtain in the HT screening: CCVJ, with excitation wavelength (λ_{exc}) of 435 nm and the emission wavelength (λ_{em}) of 520 nm; ThT, with λ_{exc} of 415 nm and λ_{em} of 520 nm; Bis-ANS, with λ_{exc} of 380 nm and λ_{em} of 520 nm; and Nile Red, with λ_{exc} of 550 nm and λ_{em} of 650 nm. After the connection of the micromixer to the UV–Vis detector, the aggregation measurement starts and the UV signal is recorded until is stable for at least 10 min. Then, after the signal

stabilization, the micromixer is disconnected from the UV–Vis detector and the UV signal is once more autozero with the FD and sample buffer mixture. This procedure was repeated for all generated aggregate samples with each of the FDs selected in this study.

2.4.3 | AEX validation

An ÄKTA™ Avant unit was used to perform an anion exchange chromatography (AEX) for the removal of aggregates, resorting to a 1 mL Capto™ adhere column (Cytiva, Massachusetts, USA). This system was equipped with: three pumps (pumps A, B and sample pump) with inlet valves in each to be able to select different buffers, a column valve, an outlet valve, three versatile valves, two UV monitors and a 10 mL Superloop™ (Cytiva, Massachusetts, USA). The sample pump was employed to inject the FD into the micromixer structure, using a flow rate of 3 μL min^{-1} (0.003 mL min^{-1}). The versatile valves were used to incorporate the superloop and the micromixer in the system. The superloop will collect the FT and eluate from the AEX column, and then send it to the micromixer channel for aggregate detection. Thus, the reduction of the pump flow rate to 3 μL min^{-1} necessary for aggregate detection in the micromixer can be achieved. Additionally, two UV monitors were employed: UV1, placed after the micromixer, to detect the increase of signal due to the presence of HMW species; and UV2, placed after the column valve, to monitor the chromatographic run. The chromatography system was controlled with the research software Orbit, a control and data acquisition system developed at Lund University (Lund, Sweden). Orbit communicates with UNICORN™ and creates the necessary instructions to run a continuous process, which then sends the information to an ÄKTA™ unit. More information on the software Orbit is described elsewhere.[18,19]

The buffers and flow rates used for the AEX chromatography run were based on GEHealthcare,[20] for a sample concentration of 60 mg mL^{-1}. The AEX operation was performed in flow through (FT) mode, with a mAb sample stressed by low pH induction, resulting in 6% aggregation. The selected FD was CCVJ ([CCVJ] = 1 μM, λ_{exc} = 435 nm, λ_{em} = 520 nm). Aggregate detection is performed during 60 min, after the collection of the FT and eluate from the AEX column in the superloop. Apart from the autozero of the UV signal, an extra phase was incorporated after aggregate detection where water is injected in the micromixer and in the connection tubes to clean and remove any remaining sample or FD.

3 | RESULTS AND DISCUSSION

3.1 | Aggregate induction and characterization

To create the necessary aggregation PAT tool, the designed micromixer should be able to detect the widest type and size range of aggregates which can arise during a biomanufacturing process. Thus, the first part of this work was to generate a broad sample variety, with aggregates possessing different physical and chemical characteristics, resorting to different induction factors. Using a mixture of mAb aggregate samples, the FDs and the micromixer will be later tested to assess the capability to detect all types of aggregates. The provided mAb already presented 4% of aggregation, becoming the first mAb sample to be tested, the hereby named storage aggregates. Then, to remove any remaining HMW species, SEC was performed and a purified mAb sample obtained, which unsurprisingly presented 0% of aggregation. Since mAb aggregate formation depends on the type of stress used,[4] protein aggregation in the purified mAb sample was then induced using a variety of aggregation factors: time, temperature, low pH shift or F/T.

The level of aggregation was determined by SEC-UPLC (Table 3), ranging from 2.5% (time aggregates) to 10% aggregation (low pH aggregates). Additionally, SEC allowed to detect oligomers in the size range of 1–25 nm,[2] with the presence of dimers and trimers across all aggregation samples. The presence of larger aggregates was then assessed by DLS, which can detect oligomers in the size range of 10 nm to 5 μm.[2] The results obtained by this analytical technique are described in Table 3 and in Figure S1B. While the monomer mAb form presents a size of 12.5 nm, all the induced aggregates exhibit HMW species with larger sizes, especially the time and F/T aggregates (up to 1 μm). The storage aggregates similarly display larger dimensions, being mainly composed of trimers and HMW species up to 640 nm, as generally aggregates increase in size (and amount) in a time-dependent manner.[2] Additionally, F/T as an aggregation induction factor, when performed with NaCl, forms larger particles (in the micron range) due to the decrease of colloidal stability.[4]

The mAb monomeric form and the resulting induced aggregates were also characterized according to their hydrophobicity by HIC.[16] The results obtained are also presented in Table 3, with the corresponding chromatograms obtained in Figure S1A. In HIC, the retention of the molecule in the column is solely due to interactions between the surface amino acids and the stationary phase. Hence, different retention times and profiles are due to conformational changes, when compared to the monomer form. Temperature and low pH induced aggregates have a later retention time and profile, with the conformational changes suffered making them more hydrophobic when compared to the remaining samples. This increase in hydrophobicity happens when the antibody is exposed to strong destabilizing conditions, such as low pH (pH 3.0) and high temperatures (75°C): the level of unfolding exposes a larger number of hydrophobic patches.[21] Nevertheless, a wide variety of different types of aggregates, ranging in terms of the level of aggregation, size and hydrophobicity, were generated. Since the type of stress that the mAb solution suffers greatly influences its physical and chemical properties,[4] and in an integrated continuous process a variety of aggregation inducing factors are employed, it was crucial to have an extensive sample set. Since the objective is to create a PAT tool which covers the entire size range or type of aggregates, it is imperative that the micromixer (with the selected FD to be employed) can detect all mAb induced aggregation samples.

TABLE 3 Aggregation samples generated resorting to different induction factors (purified mAb, time, storage, F/T, temperature and low pH induced aggregates).

Aggregation sample	Buffer	% Aggregation (SEC-UPLC)	Size (SEC-UPLC and DLS)	Hydrophobicity (HIC)
Purified mAb	50 mM Na-PB Buffer, 150 mM NaCl, pH 7.2	0	Monomer 165 kDa/12.5 nm	–
Time aggregates	50 mM Na-PB Buffer, 150 mM NaCl, pH 7.2	2.5	Mainly dimers 375 kDa/320–1000 nm	–
Storage aggregates	25 mM NaOAc +5 mM NaCl, pH 4.5	4	Mainly trimers 500 kDa/60–640 nm	–
F/T aggregates	50 mM Na-PB Buffer, 150 mM NaCl, pH 7.2	7	Mainly dimers 375 kDa/20–40 & 640–1000 nm	–
Temperature aggregates	50 mM Na-PB Buffer, 150 mM NaCl, pH 7.2	6	Trimers 500 kDa/40–80 nm	+
Low pH aggregates	50 mM Na-Citrate +500 mM NaCl, pH 3	10	Trimers 500 kDa/40–160 nm	++

Note: These samples were used in the HT screening of the FDs and in the UV–Vis detection with the micromixer. The type of aggregate induction, with the corresponding buffer used, the resulting percentage of aggregation (obtained by SEC-UPLC) and the characterization of each sample (achieved by DLS and HIC) is here described. More information on this characterization can be found in Supplementary Material (Figure S1). Na-Pb corresponds to sodium phosphate, NaCl to sodium chloride, NaOAc to sodium acetate and Na-Citrate to sodium citrate.

3.2 | HT screening of FDs

Several commercially available FDs have been used to detect mAb aggregation.[5,8,11] However, the minimal concentration required to produce a measurable signal for each FD when applied in the micromixer was still unknown. Hence, a HT screening of each FD was performed to determine the FD concentration to be employed in the micromixer. Additionally, possible constrains regarding the limit of detection of each FD can be assessed. A broad literature review on the use of these FDs was already performed in São Pedro et al.,[12] which includes the concentration and wavelengths used in each reported publication. Based on this information, the concentration range tested is described in Table 2 as well as the excitation and emission wavelengths used.

The optimal concentration for each FD was reached (Table 2), with the fluorescence spectra recorded for the best condition represented in Figure 2. As expected, all FDs had strong fluorescence signals for the majority of the mAb induced aggregation samples, with most being able to distinguish as little as 2.5% of aggregation. Moreover, the purified mAb sample displayed almost no fluorescence intensity across all four FDs. Nevertheless, Bis-ANS and Nile Red, both hydrophobic sensitive FDs, do not produce a major increase in fluorescence intensity for the F/T aggregates, when compared to the mAb purified sample. The F/T aggregates do not contain any exposed hydrophobic regions in the unfolded aggregated structure which would produce a fluorescence intensity increase by these two FDs. Previous studies indicate that the mAb native structure is retained to a high degree after F/T, with the sample mainly be composed of native-like IgG molecules.[22] The HIC characterization confirms this hypothesis since the hydrophobicity of the F/T aggregates did not increase compared to the mAb monomer form, showing the same retention time and profile. Additionally, Nile Red also does not produce a fluorescence signal for the time aggregate detection, the sample with the lowest level of aggregation, which indicates the dye's limit of detection. Therefore, Nile Red will only be suitable to be applied in mAb samples, which present more than 2.5% of aggregation.

Furthermore, for all FDs employed, it is possible to observe that the fluorescence signal measured does not directly correlate with the quantity of mAb aggregates in the sample. For example, as seen in Figure 2a, the storage aggregates display a higher fluorescence signal than the remaining mAb samples, except the low pH aggregates. However, the storage aggregates only present 4% of aggregation. The fluorescence intensity not only depends on the amount of aggregates, but also on the properties of such aggregates.[15] Ultimately, a straightforward quantification of aggregation based on the FD signal is, up to the moment, not possible. The aggregate measurement provided by the FDs and, subsequently, the micromixer, will only be qualitative, not quantitative.

3.3 | Application of micromixer

3.3.1 | UV–Vis sensor

With the FD concentration defined, the next step was to validate the developed micromixer for mAb aggregation detection resorting to a standard UV–Vis detector. Each FD, with the mAb aggregation sample to be tested, were simultaneously pumped in the microfluidic structure where both streams mixed under 30 s. A flow rate of 1 µL min^{-1} was employed, which provides a mixing efficiency of around 90%.[13] The resulting fluid is then sent to an inline UV–Vis detector where, if an increase of the signal is observed, aggregation is detected. The emission wavelength of each FD was selected according to the HT screening performed beforehand, choosing a wavelength close to the

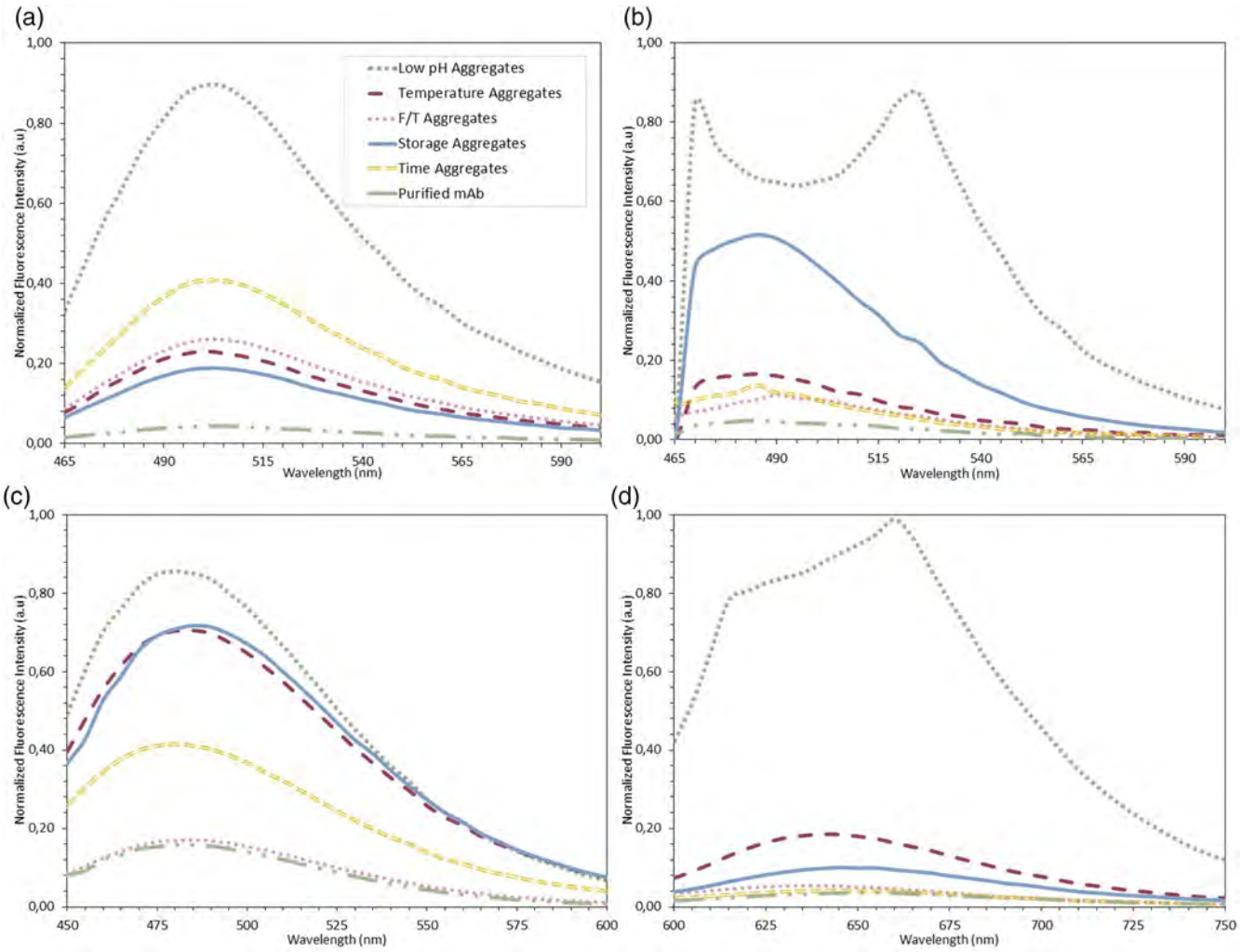

FIGURE 2 Optimized fluorescence spectra of the different FDs studied, resorting to the different type of aggregates (purified mAb, time, storage, F/T, temperature and low pH induced aggregates): (a) ThT, at a concentration of 1 mM; (b) CCVJ, at a concentration of 1 μM; (c) Bis-ANS, at a concentration of 0.5 μM; and (d) Nile Red, at a concentration of 75 μM. The excitation and emission wavelengths, as well as the tested concentrations, can be found in Table 2.

peak of the fluorescence intensity signal. Before starting the measurement, the UV signal is auto-zero with a solution composed of FD and the sample buffer (ratio one-to-one) to eliminate any possible interference from the FD intrinsic fluorescence. As observed in Figure 3a, after the micromixer is connected to the UV–Vis detector, the signal is allowed to stabilize for, at least, 10 min before finishing the measurement by disconnecting the micromixer and auto-zero again with the same FD and sample buffer solution. Similar procedure was repeated for all four FDs and all mAb aggregate samples, with the results obtained presented in Figure 4. However, not all FDs were able to be successfully employed in the UV–Vis detector. Nile Red, as observed in Figure 3b for the detection of storage aggregates, does not produce a stable signal over the imposed 10 min time range. The signal decreases during the measurement due to the aggregation of the FD. Nile Red self-associates in dimers in the micromixer and subsequently, in the tubes connecting to the UV–Vis detector, due to the dye's poor solubility in water.[23] These aggregates interfere with the aggregate measurement and, since the majority of the buffers used during the mAb purification chain are composed by water, Nile Red cannot be applied as a FD to detect aggregation within a continuous integrated process. Therefore, Nile Red was discarded as a FD to be further used in this miniaturized PAT tool.

Nevertheless, all the remaining FDs, ThT, CCVJ and Bis-ANS, were able to successfully provide a stable measurement and detect aggregation (Figure 4). The purified mAb sample, with 0% aggregation, yields no measurable UV signal across all three FDs. Moreover, all the aggregate samples displayed great increases in the UV signal when the aggregation measurement started. Although ThT could detect all the different mAb induced aggregation samples, the UV signal from the temperature and low pH aggregates is relatively less than the remaining (storage and F/T aggregates). ThT binds to intermolecular β-sheets formed in high-order aggregates, being an indicator of amyloid structure.[24,25] Hence, the lower ThT signal indicates that the temperature and low pH aggregation mechanism is not accompanied by

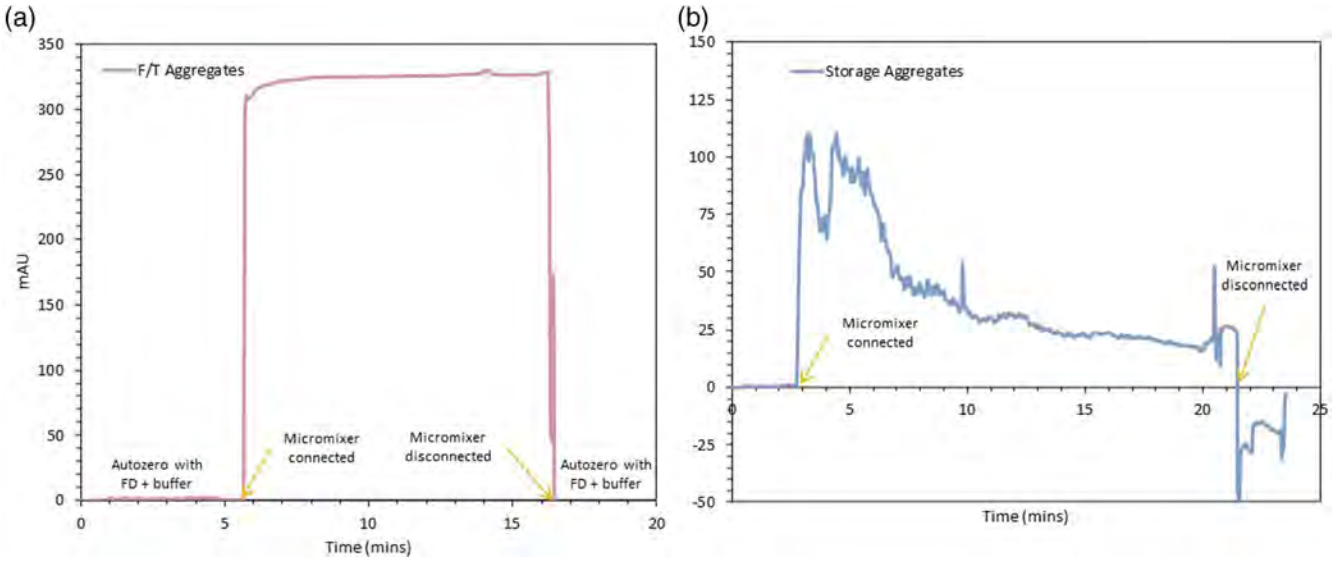

FIGURE 3 UV signal measured for: (a) F/T aggregates detected with ThT ([ThT] = 1 mM, λ_{exc} = 415 nm, λ_{em} = 520 nm); and (b) Storage aggregates detected with Nile Red ([Nile Red] = 75 μM, λ_{exc} = 550 nm, λ_{em} = 650 nm). The measurement starts with the autozero of the UV signal with a solution composed of the FD and the sample buffer, mixed in a ratio of one-to-one. Then, the micromixer is connected to the UV–Vis detector to start the aggregation detection. After the stabilization of the signal for at least 10 min, the micromixer is disconnected and the signal once more autozero with the FD and sample buffer mixture.

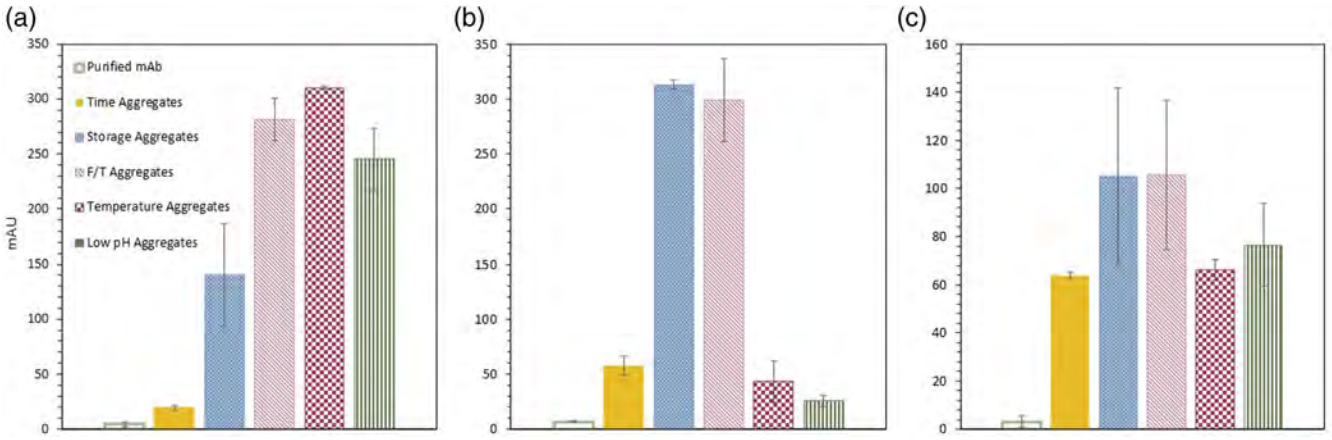

FIGURE 4 UV signal measured for each induced aggregation sample (purified mAb, time, storage, F/T, temperature and low pH induced aggregates) and the FDs: (a) CCVJ ([CCVJ] = 1 μM, λ_{exc} = 435 nm, λ_{em} = 520 nm); (b) ThT ([ThT] = 1 mM, λ_{exc} = 415 nm, λ_{em} = 520 nm); and (c) Bis-ANS ([Bis-ANS] = 0.5 μM, λ_{exc} = 380 nm, λ_{em} = 520 nm). The UV measured values are the average of two experiments and the error bars represent the standard deviation (±SD).

β-sheet formation, but by the exposure of the hydrophobic patches. The HIC results already showed the increase in the hydrophobicity of these two samples when compared to the mAb monomer form (Table 3). Therefore, since not all mAb aggregation mechanisms will lead to a β-sheet formation, ThT is no longer considered a suitable FD to be applied and will not be further explored. Nonetheless, Bis-ANS and CCVJ exhibit an ample increase in the UV signal and are suitable to be used in the micromixer. Once again, the UV signal obtained does not directly correlate with the amount of aggregates in each sample: for example, for Bis-ANS, the time aggregates produce a similar UV signal than for the temperature aggregates. Thus, FD detection of aggregation depends more on the proprieties of the aggregates than the amount, providing a merely qualitative measurement. The limit of detection (LoD) of the developed PAT tool is intrinsically connected to the LoD of the FD. Therefore, to properly use the developed PAT tool, further investigation into the LoD of the FD is needed. Additionally, in the past years, there has been the development of novel FDs, like Proteostat, which might be better suitable to detect other types of aggregates[9] and might be an alternative option to be applied in the micromixer. Nevertheless, with CCVJ and Bis-ANS being able to produce measurable UV signals, it was demonstrated the potential of using the two FDs to successfully detect HMW species.

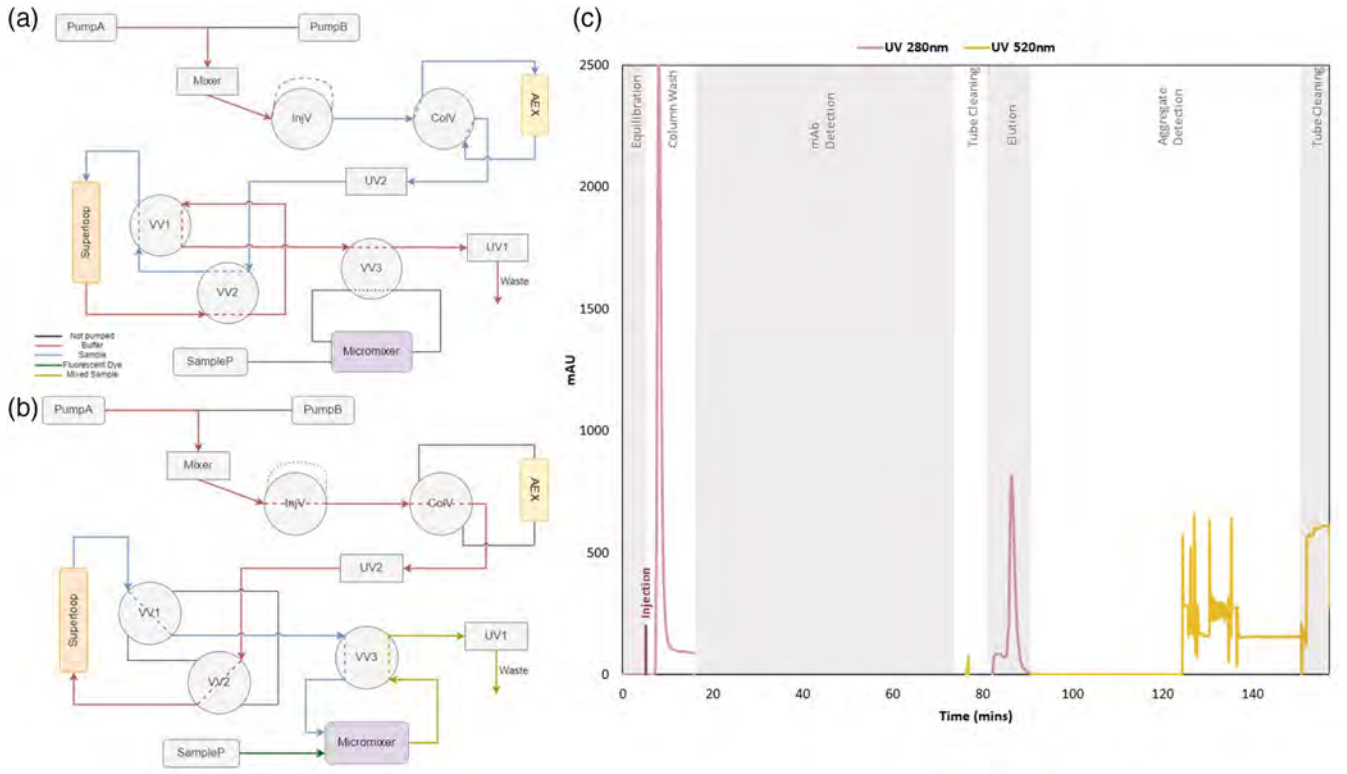

FIGURE 5 Process diagrams of the integration of the micromixer in an AEX chromatographic run in an ÄKTA™ Avant system, performed for the removal of mAb aggregates: (a) Sample application in the AEX column, with the subsequent collection of the FT in a superloop; and (b) aggregate detection of the collected sample in the micromixer. The red line represents the pathway of the different buffers pumped in by Pump A and B, whereas the blue line exemplifies the pathway performed by the sample in the system. The sample pump (SampP) is used to inject the fluorescent dye into the micromixer (green line), which, when mixed with the mAb sample (gold yellow line), is then sent to the UV1 detector. Black lines represent inactive flow paths. (c) AEX chromatographic run performed in FT mode for aggregate removal, using a low pH induced sample with 6% aggregation (60 mg mL^{-1}) and CCVJ ([CCVJ] = 1 μM, λ_{exc} = 435 nm, λ_{em} = 520 nm) as the FD. Firstly, after the column equilibration, mAb sample is injected in the column and the FT is collected in the superloop. The sample is then directed to the micromixer where is mixed with the FD at a flow rate of 3 μL min^{-1}, with the signal detection being performed during 60 min. Then, the tubes and micromixer are cleaned with water and the same procedure is repeated for the elution of the AEX column.

Finally, one of the design constrains when developing this fluorescent dye-based microfluidic sensor was that the micromixer would not alter the amount of aggregates.[13] To confirm that indeed the micromixer was not affecting the sample's aggregation levels, the mAb aggregate samples were collected after the UV–Vis detection and analyzed by SEC-UPLC. No increase in the level of aggregation was observed for any analyzed sample (data not shown). Therefore, the developed microfluidic sensor fulfills all the design constrains of a PAT tool: a real-time measurement of mAb aggregation in a continuous process can be achieved, with the micromixer providing 90% of mixing efficiency within 30 s.[13]

3.3.2 | AEX validation

The final evaluation of the fluorescent dye-based micromixer was to employ it in a chromatographic operation for aggregate detection. AEX chromatography was performed in a flow-through (FT) mode for the removal of aggregates, which has been previously optimized.[20] The micromixer was then implemented in a standard ÄKTA™ Avant unit, with the addition of an extra UV sensor, one 10 mL superloop and three versatile valves (Figure 5a,b). The extra UV sensor (UV2) was used to monitor the chromatographic run whereas the UV already present in the ÄKTA™ unit (UV1) was placed after the micromixer to detect the aggregation signal provided by the FD. The superloop was added, after the chromatography column, to collect the FT and the eluate (Figure 5a). The pumps already existing in the system, pump A and B, were not only used for the chromatographic run but also to pump the FT/eluate collected in the superloop directly to the micromixer (Figure 5b). Therefore, to allow the reduction of flow rate for aggregate detection in the micromixer, the incorporation of the superloop was crucial. Due to pump limitations for lower flows, a flow rate of 3 μL min^{-1} was applied, which is still able to provide a high mixing efficiency (around 85%). Additionally, the sample pump (SampP) injects the FD directly into the micromixer, with a similar flow rate.

TABLE 4 Aggregation levels and concentration determined by SEC-UPLC for each collected sample from the AEX chromatographic run.

	Aggregation (%)	Concentration (mg mL^{-1})
Initial sample	6	60.0
FT sample	0.4	2.0
Eluate sample	5	0.5

From the results obtained in the UV–Vis detector, CCVJ, a molecular rotor, showed a more significant UV signal increase, around 300 mAU, being the preferred FD to be used in this validation. A mAb sample, with a concentration of 60 mg mL^{-1}, was stressed by low pH induction, obtaining a 6% level of aggregation (Table 4). This aggregation sample was then injected onto an AEX column, with the results obtained found in Figure 5c. First, after the column equilibration and sample injection, the FT is collected in the superloop. Then, a FT sample is sent to the micromixer, where when mixed with the FD, no UV signal was detected. Hence, the FT sample exhibits no aggregation, with AEX column being able to bind all the aggregates. The level of aggregation was later confirmed by SEC-UPLC (Table 4), which merely identified 0.4% of aggregates. Later, after cleaning the micromixer and the attached tubes with water and disposing the remaining sample in the superloop, the AEX elution was performed and collected. The detection procedure is repeated once more, and for the eluate, the UV signal increased. Even though theoretically the pump system can handle flow rates starting at 1 µL min^{-1}, the ÄKTA™ system still has some limitations when using lower flow rate. The presence of air bubbles is visible on the UV signal, especially in the first minutes after the signal increases. Nevertheless, the signal was allowed to stabilize and aggregation was still detected using the micromixer sensor. The detection time was initially defined to be 60 min which needs to be considerably reduced to provide a real-time analysis. Since the micromixer can provide an efficient mixing under 30 s,[13] modifications to the external ÄKTA™ setup have to be performed to decrease of the overall measurement time. For example, by reducing the connection tubes which connect the versatile valve to the micromixer, this decrease of measuring time can be achieved. The aggregate detection was again confirmed by SEC-UPLC, with the eluate collected presenting 5% of aggregation (Table 4). Thus, even if a long measuring time was defined, the proposed micromixer was still able to successfully detect aggregation.

Recently, with the development of the PAT framework, several PAT tools have been successfully implemented to detect aggregation in the required time frame for decision making and control.[26,27] For example, Patel et al.[28] has used a multi-angle light scattering (MALS) system coupled to ÄKTA™ unit to real-time quantify the formation of aggregates. However, extra equipment such as a MALS system is not as readily available as a standard UV–Vis detector to detect aggregation. If the detection time can be significantly decreased, the increase in the UV signal can be used as a cut-off point to stop collecting the mAb product. When developing this PAT sensor, several design constraints were imposed including: the overall cost of the technique had to be minimal and the microfluidic chip simple to operate.[12] By using a zigzag micromixer and a simple extra UV monitor connected to a ÄKTA™ unit, these design constraints are met since no external equipment and setup is required, which would increase the cost and complexity of the developed PAT tool. Although FDs have inherent limitations regarding the quantification of the HMW species, a simple zigzag micromixer was firstly designed[13] and hereby applied and tested. Thus, this work demonstrates that the miniaturization of the analytical technique discussed by São Pedro et al.[12] is a powerful solution to speed up the CQAs measurement in a continuous process.

4 | CONCLUDING REMARKS

A PAT fluorescent dye-based microfluidic sensor was developed and hereby introduced, being able to detect all different types of aggregates tested. From a SEC purified mAb sample, with 0% of aggregation, several induction factors were used to create a large variety of mAb aggregates, which presented different physical and chemical properties. A HT screening was then performed to assess the required concentration, emission wavelength and limit of detection of each FD later to be applied in the micromixer. This microfluidic chip was then connected to an UV–Vis detector and tested to detect mAb aggregation with all the stressed samples. Even though Nile Red and ThT were not suitable to be applied due to intrinsic limitations of the dye, Bis-ANS and CCVJ provide a measurable signal when aggregates were present in the analyzed sample. However, a measurement resorting to FDs will merely be qualitative, not yet being possible to quantify aggregation based on its signal. The FD signal is more dependent on the type of aggregate than its amount, making this developed PAT tool able to solely detect protein aggregation. Ultimately, the micromixer was validated in an AEX chromatographic run for the removal of mAb aggregates. An increase of the UV signal was observed on the eluate sample, which presented 5% of aggregation, whereas the FT sample, with 0.4% of aggregation, was not (Figure 5c and Table 4). Even though further investigation into the LoD of each FD should be performed, it was demonstrated that the micromixer can efficiently and robustly detect several type of aggregates and can be easily incorporated in a downstream unit operation.

Although the micromixer was able to successfully detect aggregation in a chromatography run, the measurement was still performed for 60 min. To create a real-time measurement, this detection time ought to be significantly reduced. By decreasing the connection tubes length in the ÄKTA™ system and/or introducing an extra phase in the Orbit software to fill these tubes with sample prior to the measurement, this time reduction should be achieved. Nevertheless, a fluorescent dye-based microfluidic

sensor was demonstrated, being able to effectively detect a wide range of mAb aggregates. Furthermore, the micromixer was capable of handling the higher flow rates and pressure inherent to the ÄKTA™ system, demonstrating the potential of miniaturizing the analytical technique to accelerate CQAs measurement to the required time frame for process control.

AUTHOR CONTRIBUTIONS

Mariana Neves São Pedro: Investigation (lead); methodology (lead); validation (lead); writing – original draft (lead). **Michel H. M. Eppink:** Funding acquisition (equal); methodology (supporting); project administration (supporting); supervision (supporting); writing – review and editing (equal). **Marcel Ottens:** Funding acquisition (lead); methodology (supporting); project administration (lead); supervision (lead); writing – review and editing (equal).

ACKNOWLEDGMENTS

The authors wish to thank the European Union's Horizon 2020 research and innovation programme under the Marie Skłodowska-Curie grant agreement No 812909 CODOBIO, within the Marie Skłodowska-Curie European Training Networks framework.

CONFLICT OF INTEREST STATEMENT

The authors have declared no conflict of interest.

PEER REVIEW

The peer review history for this article is available at https://www.webofscience.com/api/gateway/wos/peer-review/10.1002/btpr.3355.

DATA AVAILABILITY STATEMENT

The data that support the findings of this study are available from the corresponding author upon reasonable request.

ORCID

Mariana N. São Pedro https://orcid.org/0000-0002-1801-9629

REFERENCES

1. São Pedro MN, Silva TC, Patil R, Ottens M. White paper on high-throughput process development for integrated continuous biomanufacturing. *Biotechnol Bioeng*. 2021;118(9):3275-3286.
2. Bansal R, Gupta S, Rathore AS. Analytical platform for monitoring aggregation of monoclonal antibody therapeutics. *Pharm Res*. 2019;36(11):152.
3. Schermeyer M-T, Wöll AK, Kokke B, Eppink M, Hubbuch J. Characterization of highly concentrated antibody solution—a toolbox for the description of protein long-term solution stability. *MAbs*. 2017;9(7):1169-1185.
4. Telikepalli SN, Kumru OS, Kalonia C, et al. Structural characterization of IgG1 mAb aggregates and particles generated under various stress conditions. *J Pharm Sci*. 2014;103(3):796-809.
5. He F, Phan DH, Hogan S, et al. Detection of IgG aggregation by a high throughput method based on extrinsic fluorescence. *J Pharm Sci*. 2010;99(6):2598-2608.
6. Paul AJ, Bickel F, Rohm M, Hospach L, et al. High-throughput analysis of sub-visible mAb aggregate particles using automated fluorescence microscopy imaging. *Anal Bioanal Chem*. 2017;409(17):4149-4156.
7. Bothra A, Bhattacharyya A, Mukhopadhyay C, Bhattacharyya K, Roy S. A fluorescence spectroscopic and molecular dynamics study of bis-ANS/protein interaction. *J Biomol Struct Dyn*. 1998;15(5):959-966.
8. Hawe A, Filipe V, Jiskoot W. Fluorescent molecular rotors as dyes to characterize polysorbate-containing IgG formulations. *Pharm Res*. 2010;27(2):314-326.
9. Oshinbolu S, Shah R, Finka G, Molloy M, Uden M, Bracewell DG. Evaluation of fluorescent dyes to measure protein aggregation within mammalian cell culture supernatants. *J Chem Technol Biotechnol*. 2018;93(3):909-917.
10. Biancalana M, Koide S. Molecular mechanism of Thioflavin-T binding to amyloid fibrils. *Biochim Biophys Acta*. 2010;1804(7):1405-1412.
11. Paul AJ, Schwab K, Prokoph N, Haas E, Handrick R, Hesse F. Fluorescence dye-based detection of mAb aggregates in CHO culture supernatants. *Anal Bioanal Chem*. 2015;407(16):4849-4856.
12. São Pedro MN, Klijn ME, Eppink MHM, Ottens M. Process analytical technique (PAT) miniaturization for monoclonal antibody aggregate detection in continuous downstream processing. *J Chem Technol Biotechnol*. 2021;97:2347-2364.
13. São Pedro MN, Santos MS, Eppink MHM, Ottens M. Design of a microfluidic mixer channel: first steps into creating a fluorescent dye-based biosensor for mAb aggregate detection. *Biotechnol J*. 2022;18:2200332.
14. Sulatskaya AI, Lavysh AV, Maskevich AA, Kuznetsova IM, Turoverov KK. Thioflavin T fluoresces as excimer in highly concentrated aqueous solutions and as monomer being incorporated in amyloid fibrils. *Sci Rep*. 2017;7(1):2146.
15. Hawe A, Friess W, Sutter M, Jiskoot W. Online fluorescent dye detection method for the characterization of immunoglobulin G aggregation by size exclusion chromatography and asymmetrical flow field flow fractionation. *Anal Biochem*. 2008;378(2):115-122.
16. Goyon A, D'Atri V, Bobaly B, Wagner-Rousset E, et al. Protocols for the analytical characterization of therapeutic monoclonal antibodies. I—Non-denaturing chromatographic techniques. *J Chromatogr B Analyt Technol Biomed Life Sci*. 2017;1058:73-84.
17. Gokaltun A, Kang YBA, Yarmush ML, Usta OB, Asatekin A. Simple surface modification of poly(dimethylsiloxane) via surface segregating smart polymers for biomicrofluidics. *Sci Rep*. 2019;9(1):7377.
18. Gomis-Fons J, Andersson N, Nilsson B. Optimization study on periodic counter-current chromatography integrated in a monoclonal antibody downstream process. *J Chromatogr A*. 2020;1621:461055.
19. Gomis-Fons J, Schwarz H, Zhang L, et al. Model-based design and control of a small-scale integrated continuous end-to-end mAb platform. *Biotechnol Prog*. 2020;36(4):e2995.
20. GEHealthcare, Selective removal of aggregates with Capto adhere. Application note 28–9078-93 AB. 2012.
21. Arosio P, Rima S, Morbidelli M. Aggregation mechanism of an IgG2 and two IgG1 monoclonal antibodies at low pH: from oligomers to larger aggregates. *Pharm Res*. 2013;30(3):641-654.
22. Hawe A, Kasper JC, Friess W, Jiskoot W. Structural properties of monoclonal antibody aggregates induced by freeze-thawing and thermal stress. *Eur J Pharm Sci*. 2009;38(2):79-87.
23. Ray A, Das S, Chattopadhyay N. Aggregation of Nile red in water: prevention through encapsulation in beta-cyclodextrin. *ACS Omega*. 2019;4(1):15-24.
24. Li Y, Mach H, Blue JT. High throughput formulation screening for global aggregation behaviors of three monoclonal antibodies. *J Pharm Sci*. 2011;100(6):2120-2135.
25. Sahin E, Grillo AO, Perkins MD, Roberts CJ. Comparative effects of pH and ionic strength on protein-protein interactions, unfolding, and aggregation for IgG1 antibodies. *J Pharm Sci*. 2010;99(12):4830-4848.

26. Rathore AS, Yu M, Yeboah S, Sharma A. Case study and application of process analytical technology (PAT) towards bioprocessing: use of on-line high-performance liquid chromatography (HPLC) for making real-time pooling decisions for process chromatography. *Biotechnol Bioeng*. 2008;100(2):306-316.
27. Rolinger L, Rudt M, Diehm J, Chow-Hubbertz J, et al. Multi-attribute PAT for UF/DF of proteins-monitoring concentration, particle sizes, and buffer exchange. *Anal Bioanal Chem*. 2020;412(9):2123-2136.
28. Patel BA, Gospodarek A, Larkin M, et al. Multi-angle light scattering as a process analytical technology measuring real-time molecular weight for downstream process control. *MAbs*. 2018;10(7):945-950.

SUPPORTING INFORMATION

Additional supporting information can be found online in the Supporting Information section at the end of this article.

BACK TO CONTENTS

Received: 31 January 2023 | Revised: 4 May 2023 | Accepted: 6 May 2023

DOI: 10.1002/bit.28434

ARTICLE

BIOTECHNOLOGY AND BIOENGINEERING WILEY

Predictive scaling of fiber-based protein A capture chromatography using mechanistic modeling

Tobias Hahn[1] | Tatjana Trunzer[1] | Florence Rusly[2] | Ryan Zolyomi[2] | Lalita K. Shekhawat[3] | Gunnar Malmquist[3] | Ashley Hesslein[2] | Hendri Tjandra[2]

[1]Cytiva, Karlsruhe, Germany

[2]Bayer, Berkeley, California, USA

[3]Cytiva, Uppsala, Sweden

Correspondence

Tobias Hahn, Cytiva, Global Life Sciences Solutions Germany GmbH, Kriegsstraße 240, Karlsruhe 76135, Germany.
Email: tobias.hahn@cytiva.com

Abstract

Protein A affinity chromatography is an important step in the purification of monoclonal antibodies (mAbs) and mAb-derived biotherapeutics. While the biopharma industry has extensive expertise in the operation of protein A chromatography, the mechanistic understanding of the adsorption/desorption processes is still limited, and scaling up and scaling down can be challenging because of complex mass transfer effects in bead-based resins. In convective media, such as fiber-based technologies, complex mass transfer effects such as film and pore diffusions do not occur which facilitates the study of the adsorption phenomena in more detail and simplifies the process scale-up. In the present study, the experimentation with small-scale fiber-based protein A affinity adsorber units using different flow rates forms the basis for modeling of mAb adsorption and elution behavior. The modeling approach combines aspects of both stoichiometric and colloidal adsorption models, and an empirical part for the pH. With this type of model, it was possible to describe the experimental chromatograms on a small scale very well. An in silico scale-up could be carried out solely with the help of system and device characterization without feedstock. The adsorption model could be transferred without adaption. Although only a limited number of runs were used for modeling, the predictions of up to 37 times larger units were accurate.

KEYWORDS

colloidal particle adsorption model, flow rate dependency, modeling, protein A fibro chromatography, scale-up

1 | INTRODUCTION

Protein A affinity chromatography is an important step in the purification of monoclonal antibodies (mAbs) and mAb-derived biotherapeutics. The purification sequence of mAbs typically starts with protein A capture chromatography and continues with one to three polishing steps using other modes of chromatography (Kelley et al., 2008). Though protein A chromatography resins are expensive and have shorter lifetime in comparison to polishing resins (Ramos-de-la-Peña et al., 2019), it remains an integral part of antibody purification platforms (Liu et al., 2010). Because of its high selectivity and capacity, the achievable purity and yield are typically higher than

95% for mAbs and thereby reduce the separation challenges for the following polishing steps significantly (Shukla et al., 2007).

Protein A is a polypeptide originating from *Staphylococcus aureus* (Hjelm et al., 1972) and thus different compared to the small chemical ligands used for ion-exchange (IEX) or hydrophobic interaction chromatography (HIC). While a mAb is assumed to bind to several of such small ligands at once during IEX or HIC (Mollerup, 2006, 2008), it is the opposite for protein A: Because of its size and constitution, it is assumed that several mAbs can bind to a single protein A ligand (Ghose et al., 2007). Depending on the ligand density and the structure of the base matrix, very different binding and elution behaviors can be observed, which has been the subject of various studies (Hahn et al., 2003, 2005; Pabst et al., 2018). The PrismA ligand used here is a hexamer of an alkaline stabilized Z domain. This suggests that up to at least three mAbs could bind to the same ligand depending on experimental conditions.

While the biopharma industry has extensive expertise in the operation of protein A chromatography, the mechanistic understanding of the adsorption/desorption processes is still limited and thereby its scaling up or scaling down can be challenging (Dimartino et al., 2011; Lienqueo et al., 2011; Montes Sanchez et al., 2004; Tejeda-Mansir et al., 2001). Benner et al. (2019) describe mass transfer effects in bead-based resins as one difficulty for the latter: This has also been a focus of research for Pabst et al. (2018), who found that smaller bead sizes reduce mass transfer limitations, or Reck et al. (2015), who visualized that pore diffusion depends on protein size and loading conditions as well as salt concentration.

In convective media, such as the fiber-based Fibro technology (Figure 1), complex mass transfer effects such as film and pore diffusion do not occur which facilitates studying adsorption effects in more detail and simplifies the process scale-up. However, it must be pointed out that all convective media have an individual topology and thus a distinct flow behavior (Podgornik, 2022). Fibrous adsorbers can be created from various materials, including natural and synthetic polymers, and arranged in different ways for the use as chromatography media. Fiber structures include randomly packed short fibers (Gavara et al., 2012; King & Pinto, 1992; Singh & Pinto, 1995), aligned fibers (Czok & Guiochon, 1990; Marcus et al., 2003) woven fabrics (Yang et al., 1992), and electrospun fiber mats (Hardick et al., 2012) as used in this study. The potential of these materials to increase productivity have been the subject of experimental studies in batch (Gavara et al., 2012, 2015; Hardick et al., 2012) and continuous mode (Hardick et al., 2015), as well as studies employing mechanistic modeling (Winderl et al., 2016).

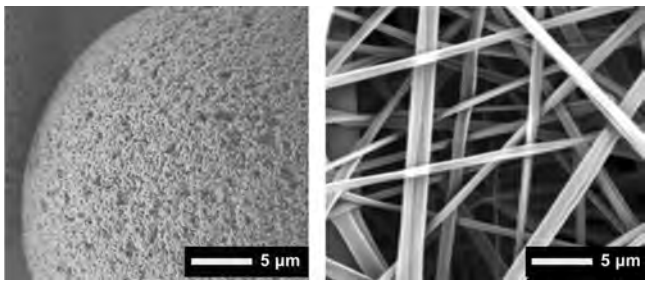

FIGURE 1 Fiber-based chromatography uses a well-defined matrix of cellulose fibers (right) that has a very open structure relative to chromatography beads (left). While beads have a surface area of ~40 m^2/g, most binding sites are only accessible by diffusion. In contrast, the surface area of Fibro of ~10 m^2/g is accessible by convection. The surface area was provided by Cytiva and determined with BET (Brunauer–Emmett–Teller) analysis.

The binding behavior of mAbs to protein A has been described with Langmuir-type isotherms in the past (Lane, 2018; Pabst et al., 2018), while acknowledging that the fundamental assumption of a one-to-one binding mechanism does not hold for protein A chromatography. The more recent modeling approach of Lane (Lane, 2018) also takes the protonation state of both the target mAb and the protein A ligand into account.

The modeling approach employed in this work combines aspects of both stoichiometric and colloidal models. The surface blocking function from the colloidal particle adsorption (CPA) model (Briskot, Hahn, Huuk, & Hubbuch, 2021; Briskot, Hahn, Huuk, Wang, et al., 2021) was used in combination with a pH-dependent equilibrium coefficient and a finite rate of adsorption kinetics, as first used by Thomas for nonporous particles (Thomas, 1944). The derivation of the surface saturation function is independent of the chromatography mode and is thus assumed to be transferrable to affinity chromatography.

When modeling membranes, monoliths, and fiber-based materials, precise system and device characterization is of great importance as hold-up volumes in the devices can exceed the functionalized adsorber volume. In this study, extensive experimentation at different flow rates with tracer substances were performed for three system scales, with and without prototypical Fibro units with volumes ranging from 4.3 to 160 mL. The Fibro units consist of the PrismA affinity ligand coupled to electrospun cellulose nanofiber adsorbents. Following the fundamental assumption of *in silico* scale-up and scale-down of chromatography, that the adsorption model is scale-independent, four bind-and-elute experiments at 4.3 mL small scale were needed to calibrate the model. The model is then used to predict the behavior of 40 and 160 mL Fibro prototype units.

2 | THEORY

2.1 | Adsorption model

Sandoval et al. (2012) developed a model for affinity chromatography by following a common stoichiometric approach and adding a pH-relationship empirically. Here, one mole of protein molecule P in solution is assumed to bind to one mole of protein A ligands L, forming one mole of protein-ligand complexes PL:

$$P + L \rightleftharpoons PL. \quad (1)$$

Theoretically, it would be possible to extend the above equation with a stoichiometric coefficient to describe that three mAbs can bind to one PrismA ligand. However, as it is unclear whether the full saturation happens also under all conditions, Equation (1) was used unmodified. Applying the law of mass action, the equilibrium formulation was derived to be

$$\frac{q}{c} = k_{eq}\bar{q}, \tag{2}$$

where c and q are the molar protein concentrations in solution and bound to the stationary phase, respectively. $\bar{q}$ is the normalized concentration of available ligands which is later replaced by the CPA surface coverage function, as also applied in Hahn et al. (2022).

Similar to Hunt et al. (2017) for IEC and Hahn et al. (2018) for HIC, the pH-dependency of the equilibrium constant, k_{eq} was empirically included by Sandoval et al. (2012) as

$$k_{eq}(pH) = k_{eq0}\cdot 10^{k_{eq1}\cdot(pH-pH_{ref})}. \tag{3}$$

In this work, we added a second order term to achieve a better agreement with the experimental data, and also included an exponential influence of the salt concentration times the interaction parameter K_s, stemming from Mollerup's model of the protein solute activity coefficient (Mollerup, 2008):

$$k_{eq}(pH) = k_{eq0}\cdot 10^{k_{eq1}\cdot(pH-pH_{ref})+k_{eq2}\cdot(pH-pH_{ref})^2}\cdot \exp^{K_S\cdot c_{salt}}. \tag{4}$$

As later shown in Table 4, the second order term limits the k_{eq} value at binding pH and allows for a steep slope at the point of elution. This is especially beneficial when simulating long gradient elutions. Adding the K_s term to a protein A model was first proposed in Schwan (2019).

The general structure of the nonlinear isotherm follows the CPA formalism for ion-exchange chromatography (Briskot, Hahn, Huuk, & Hubbuch, 2021). The rate of change of the bound protein concentration is described by a constant kinetic rate k_{kin} and adsorption and desorption terms, multiplied by the protein concentrations in solution and adsorbed state, respectively.

$$\frac{\partial q}{\partial t} = k_{kin}[k_{eq}(pH)\cdot B(A_s, a)\cdot c - q]. \tag{5}$$

The available surface function B from the CPA model depends on the resin specific surface area A_s, a material-specific constant, and protein colloid radius a. It is explained in detail in Briskot, Hahn, Huuk, Wang, et al. (2021).

A summary of all model parameters and their physical meaning is given in Table 1.

2.2 | Column model

In the absence of microporous volumes that are accessible by diffusion only, a lumped kinetic model (Seidel-Morgenstern, 2020) was selected to describe the temporal change of the solute bulk concentration c_i of solute i:

$$\frac{\partial c_i}{\partial t}(x,t) = -\ u_{int}\frac{\partial c_i}{\partial x}(x,t) + D_{app,i}\frac{\partial^2 c_i}{\partial x^2}(x,t) - \frac{1-\varepsilon_t}{\varepsilon_t}\frac{\partial q_i}{\partial t}(x,t), \tag{6}$$

where x represents the axial position within the column, t is the time, D_{app} denotes the apparent dispersion coefficient, u_{int} is the interstitial velocity, ε_t represents the void fraction, and q_i represents the concentration of the i-th solute with respect to the adsorber skeleton volume.

The column model is complemented with Danckwerts boundary conditions

$$\frac{\partial c_i}{\partial x}(0,t) = \frac{u_{int}}{D_{app,i}}(c_i(0,t) - c_{in,i}(t)), \tag{7}$$

$$\frac{\partial c_i}{\partial x}(L,t) = 0, \tag{8}$$

where $c_{in,i}$ is the prescribed concentration of species i at the inlet of the column.

3 | MATERIALS AND METHODS

3.1 | Chromatographic instrumentation

The prototypical Fibro units with PrismA protein A ligands used in this study covered laboratory to pilot scale, ranging from matrix

TABLE 1 Summary of component-specific adsorption model parameters.

Model parameter	Unit	Meaning
Protein radius a_i	[m]	A protein is represented by a sphere with radius a_i.
Equilibrium coefficient $k_{eq,i}(pH)$	[−]	pH-dependent equilibrium constant derived from the application of the law of mass action.
Kinetic constant $k_{kin,i}$	[s^{-1}]	Measure for the rate of adsorption/desorption.
Specific adsorber surface to volume ratio $A_{s,i}$	[m^{-1}]	Adsorber surface per adsorber skeleton volume accessible by the mAb.
Activity coefficient parameter $K_{s,i}$	[M^{-1}]	Influence of salt concentration on the asymmetric activity coefficient

volumes (or membrane volumes, MV) of 4.3 mL (small scale Fibro PrismA) to 40 mL (medium scale Fibro PrismA), up to 160 mL (pilot scale Fibro PrismA). Experiments were performed on three different chromatography systems: ÄKTA avant 150, ÄKTA pilot 600, and ÄKTA ready with Low Flow Kit (all Cytiva, Little Chalfont), each controlled with the software UNICORN 7.0.2. The systems were chosen fitting to the volumetric flow rate recommended to operate the specific Fibro units. Accordingly, the ÄKTA avant 150 was combined with the 4.3 mL small scale unit, the ÄKTA pilot 600 with the 40 mL medium scale Fibro unit, and the ÄKTA ready with the 160 mL pilot scale Fibro unit. It should be pointed out once again that the units used in this study were prototypes that differ slightly from those commercially available in geometry (compare with HiTrap™ Fibro PrismA and HiScreen™ Fibro PrismA units datafile, 2022). The system characteristics were determined with salt step change experiments, the Fibro unit size measurements and porosity of the functional fiber layer and non-woven layer were determined experimentally. Detailed experiment information can be found in Section 3.3.

3.2 | Buffers and feedstock

System and column-specific effects were determined with a step change experiment in which a 50 mM NaCl equilibration buffer was replaced with a mobile phase with 300 mM NaCl with 1% acetone. To perform mAb capture in pH-controlled bind-and-elute mode, a buffer with 50 mM Tris and 50 mM NaCl at pH 7 was used for equilibration and a first wash phase. A second high-salt wash was performed with a 50 mM acetate buffer with additional 1 M NaCl at pH 5.5. pH step elution started at pH 6 and went down to pH 3.4 using 50 mM acetate buffers containing 50 mM NaCl. In case of linear pH gradient elutions, lower pH ranges were used to ensure complete elutions: The gradients started with a 50 mM acetate buffer containing 30 mM NaCl at pH 5 and ended with a 50 mM acetate buffer containing 50 mM NaCl at pH 3. Sanitization was performed with 0.5 M NaOH.

The antibody feedstock used in this study is derived from industrial CHO cultivation. The clarified cell culture fluid (pH = 7.2, 13 mS/cm) with an antibody titer of 4.7 g/L was filtered before loading and included a monomer species, as well as high molecular weight (HMW) and low molecular weight (LMW) variants, and host cell proteins (HCPs) which were not analyzed further within this case study.

3.3 | Experimental design

The ÄKTA avant 150 and the ÄKTA pilot 600 systems as well as the respective Fibro units (4.3 and 40 mL) were characterized with salt step change experiments at 3.5 and 7 MV/min, and 4 and 8 MV/min, respectively. The ÄKTA ready with the 160 mL Fibro prototype was characterized with a salt step change experiment at 4 MV/min.

To study the adsorption behavior of the mAb, both gradient and step elution experiments were performed at the lab-scale (ÄKTA avant 150 with small scale Fibro PrismA prototype). The pH gradient experiments with different gradient slopes were performed at 3.5 MV/min, a similar experiment with partial breakthrough was performed with flow rates of 3.5 and 7 MV/min. The experiments performed at gradient lengths of 21.5 and 34.4 MV are designed to determine the change of elution pH as a function of gradient slope, similar to the experimental design used for Yamamoto method (Yamamoto et al., 1983) but without analytical parameter determination. The pH step elution experiment was performed at 3.5 MV/min at small scale and 4 MV/min on the other scales. The lab-scale experiment was used for model calibration, and the ones on the two larger scales for model validation. Moreover, a pH step elution experiment was performed at twice the original flow rate to validate the model at laboratory and medium scale. All step elution experiments at medium and pilot scale followed the same approach: after equilibration for 5 MV, the Fibro units were loaded with 28–30 g/L_{MV}, followed by low salt and high salt washes of 9 MV. The step elution lasted for 6 MV, and the sanitization 4 MV. Subsequent to this, the system was re-equilibrated for 7 MV. The small scale step experiment used the same sequence of phases but each duration in MV was chosen 14% shorter.

An overview of the performed scale-dependent system and column characterization experiments, as well as model calibration and validation experiments can be found in Table 2.

3.4 | Numerical methods

The simulations were performed using the GoSilico Chromatography Modeling Software version 1.12.0, which is based on ChromX (Hahn et al., 2015). A finite element method with linear elements was used together with discretization in time using the Fractional step θ time-stepping algorithm (Hindmarsh et al., 2005).

3.5 | Model parameter estimation and model-based scale-up

The systems and Fibro units were modeled using dispersed plug flow reactors (DPFRs) and continuously stirred tank reactors (CSTRs). Model parameters were estimated from the salt step change experiments. The flow rate dependent CSTR and DPFR effects are system/unit specific and were kept constant when continuing model calibration with bind-elute experiments.

The adsorption parameter estimation was performed sequentially using the experimental results obtained on small scale Fibro unit. pH was simulated as a mobile phase modifier according to Equation 6). All parameters of the equilibrium adsorption isotherm were expected to be scale- and flow-independent and estimated simultaneously. The initial estimation was performed with an adaptive simulated annealing algorithm (Ingber, 1993) using all four

TABLE 2 Overview of characterization, calibration, and validation experiments.

	Experimental conditions	Flow rate (MV/min)
System characterization		
ÄKTA avant 150	Step change with high salt buffer	3.5, 7
ÄKTA pilot 600		4, 8
ÄKTA ready		4
Fibro unit characterization		
4.3 mL small scale Fibro PrismA prototype	Step change with high salt buffer	3.5, 7
40 mL medium scale Fibro PrismA prototype		4, 8
160 mL pilot scale Fibro PrismA prototype		4
Calibration at lab-scale (ÄKTA avant 150 with small scale Fibro PrismA prototype)		
Linear gradient experiments	22 and 34 MV gradient elution, mAb sample in 100 mM NaCl	3.5
mAb breakthrough	Step elution, mAb sample in 50 mM NaCl	3.5, 7
Step experiment	Step elution, mAb sample in 100 mM NaCl	3.5, 7
Validation by cross-scaling		
ÄKTA pilot 600 with 40 mL Fibro PrismA	Step elution, mAb sample in 100 mM NaCl	4, 8
ÄKTA ready with 160 mL Fibro PrismA		4

lab-scale experiments at a flow rate of 3.5 MV/min and the normalized least squares error norm. Model parameters were finally refined using a Levenberg-Marquardt algorithm (Agarwal & Mierle, 2022).

The model uncertainty was evaluated with forward finite differences to compute the approximate parameter covariance matrix and confidence intervals. After model calibration and quality assessment, the model was used for in silico process scale-up by applying only the scale-specific fluid dynamic parameters and keeping the molecule-specific adsorption parameters determined in small scale constant.

3.6 | Evaluation of flow rate dependent binding kinetics

A detailed analysis of flow rate dependent binding effects was performed independently from the main study and is discussed in Section 4.3. For this, an ÄKTA avant with a HiTrap Fibro PrismA (HiTrap™ Fibro PrismA and HiScreen™ Fibro PrismA units datafile, 2022) unit of 0.4 mL was used. Loading till breakthrough with a second purified industrial mAb, followed by pH step elution was performed at different flow rates ranging from 5 to 40 MV/min. 20 mM phosphate buffer containing 150 mM NaCl (pH 7.4) was used as equilibration and wash buffer (attained after 100% breakthrough when the UV cell was saturated). The pH step elution is induced with 50 mM acetate buffer (pH = 3.5). Afterward, cleaning-in-place is performed with 0.5 M NaOH. The HiTrap unit was loaded with 1 g/L mAb buffer exchanged into 20 mM phosphate buffer (pH = 7.4) containing 150 mM NaCl.

4 | RESULTS AND DISCUSSION

4.1 | System and column characterization

To describe the systems precisely, that is, as individually configured, each ÄKTA system is represented in the model as a composition of system tubing and equipment items such as restrictors (i.e., pump restrictor), valves (i.e., injection valve, column valve) and sensors (i.e., UV cell, conductivity cell) as present and measurable in the real system (ÄKTA avant chromatography system, 2022; ÄKTA pilot 600 chromatography system, 2022; ÄKTA ready and ÄKTA ready XL Flow Kits, 2022). Figure 2 gives an overview of the system configuration with and without a Fibro unit attached. Characterizing these two cases independently allows differentiation between system-specific or Fibro unit-specific fluid dynamic effects. The ÄKTA avant system is modeled starting at the injection valve, and, separately, starting

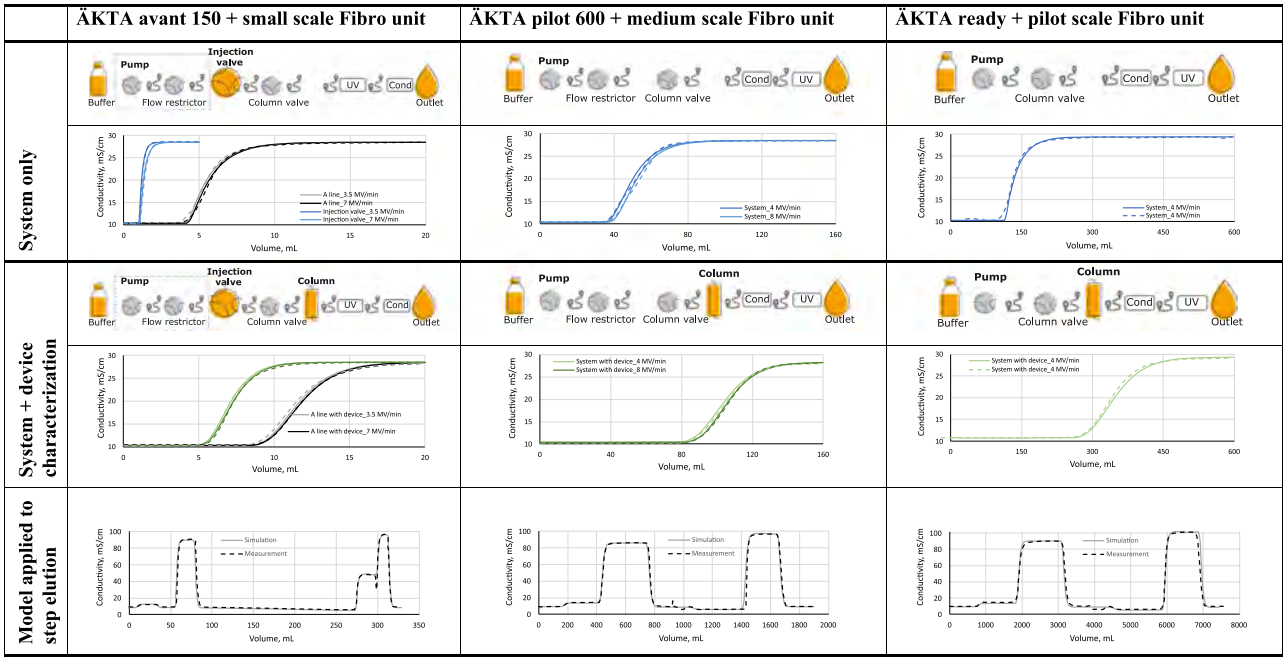

FIGURE 2 System configuration and Fibro PrismA unit characterization. Dashed lines represent the experiment, solid lines the simulation signal of the calibrated model. Lighter colored curves show experiments performed at lower (3.5 or 4 MV/min), darker colored curves the corresponding experiments at higher flow rates (7 or 8 MV/min). The conductivity curves in the bottom row show validation runs based on the system + device model, all at lower flow rate.

TABLE 3 Fibro unit geometries and flow rate-dependent apparent dispersion parameters. More information can be found in the Supporting Information.

Property	Unit	Small scale Fibro unit		Medium scale Fibro unit		Pilot scale Fibro unit
Membrane volume V	[mL]	4.31		40.12		160.48
Functionalized membrane thickness L	[mm]	2.2		2.2		2.2
Total porosity ε_t	[−]	0.676		0.676		0.676
Flow rate	[MV min^{-1}]	3.5	7	4	8	4
	[mm s^{-1}]	0.1283	0.3780	0.1467	0.2933	0.1467
Apparent dispersion $D_{app,salt}$	[mm^{2}s^{-1}]	0.0512	0.1058	0.0252	0.0385	0.0385

from the buffer line. The different results highlight the significant impact of the flow path composition: While the tubing length does not change enough to affect the band broadening, the retention time and mixing effects increase when the sample is not directly injected at the injection valve but applied via the buffer line (pump wash included). This is due to additional equipment items such as pump restrictor or mixer valve.

The chromatograms in Figure 2 visualize the calibrated system models, in which the measured, dashed curves fit the simulated, solid conductivity traces well. The larger the applied flow rate, the more significant is the dispersion in the tubing and the Fibro unit (see Supporting Information and Table 3). Both the tubing as well as devices installed are system and scale specific. Therewith, the determined tubing dispersion coefficient (depending on tubing diameter and length) as well as the devices' mixing effects and delays (depending on void volume) cannot be compared directly to each other. However, it is safe to assume that the axial dispersion coefficient of the tubing decreases for increasing tubing diameter, while the device mixing effects increase with increasing void volume. The determined Fibro units' apparent dispersion coefficients depends on the device design. In this regard, the small prototype deviates from the two larger ones as it is constructed differently. However, the design is similar for the medium and pilot scale units as the internal void volume increases for the large Fibro unit but not the dispersion effects for the membrane itself. All considered measured or

estimated parameters are listed in detail in the Supporting Information.

After finalizing the fluid dynamic model at all scales, it was validated with three exemplary experiments from the calibration set, illustrated in the bottom row of Figure 2 (experiments performed at low flow rate, 3.5 MV for ÄKTA avant and 4 MV/min for ÄKTA pilot and ready). The measured conductivity is well described by the simulation. This shows that the simple salt step change experiments are sufficient for calibration and the resulting model with flow rate-dependent dispersion parameters is applicable to more complex chromatography methods with differently concentrated buffer solutions.

4.2 | Model calibration with bind-and-elute experiments

To describe the mAb-protein A ligand interaction, the newly developed affinity isotherm was calibrated by curve fitting. The resulting parameters are listed in Table 4. Assuming that neither the equilibrium coefficient nor the blocking function (see Equation 5) is flow-dependent (assumption discussed in detail in Section 4.3), the model is calibrated based on two low-loaded gradient experiments, one partial breakthrough and one step experiment performed at 3.5 MV/min at lab-scale. The simulated chromatograms are shown in Figure 3 together with the respective measured UV signals. The breakthrough profile was simulated with a nonbinding species with the inlet concentration adjusted to match the observed UV level. Further, to account for UV detector saturation, the simulated UV traces were limited to 3000 mAU. The curves agree well, and model quality was assessed with the help of calculated approximate confidence intervals. Subsequently, using a step elution at a flow rate of 7 MV/min, the apparent dispersion coefficient for the mAb was estimated again with unchanged isotherm parameters. The determined 95% confidence intervals for the adsorption model are small and indicate that a change of parameters values has an impact on the goodness of fit (see Table 4). An exception is the large confidence interval of the K_s parameter, which means that the influence of the salt concentration changes is not well quantifiable from the set of calibration experiments. As the process is pH-driven, this remaining uncertainty was considered acceptable. The estimated specific surface area is smaller than that for the bead-based resin Capto S ImpAct by a factor of 8–9 (Briskot, Hahn, Huuk, Wang, et al., 2021) which fits well to the ratio of surface area per gram given in Figure 1. In comparison to a packed column, the apparent dispersion parameter value is slightly larger for the lab-scale setup, but still in the same order of magnitude (0.32–0.78 mm²/s for Capto S ImpAct [Briskot, Hahn, Huuk, Wang, et al., 2021]), despite the significantly higher flow rates. The differences in the values for the two flow rates of 3.5 and 7 MV/min are not significant, especially considering the confidence intervals. The comparably large confidence interval indicates that it is not well determinable from these bind-and-elute experiments. Additional experiments under nonbinding conditions could reduce the uncertainty.

By plotting the log k_{eq} term from Equation (2) over pH as shown in Table 4, strong adsorption of the mAb species is

TABLE 4 Calibrated model parameters. The approximate 95% confidence interval expressed as a percentage of the parameter value is given in brackets.

Parameter	Unit	ÄKTA avant 150	ÄKTA pilot 600	ÄKTA ready
A_s	[m^{-1}]	8.22e + 07 (±0.07%)		
$D_{app,mAb}$ at low flow rate	[mm^2s^{-1}]	1.4698 (± 17.4%)	0.2449	0.2449
$D_{app,mAb}$ at high flow rate	[mm^2s^{-1}]	1.0937 (± 37.0%)	0.1133	n.a.
Porosity	[%]	67.6		
a	[m]	5.5×10^{-9}		
k_{eq0}	[−]	7944.74 (±2.11%)		
k_{eq1}	[pH^{-1}]	5.5214 (±2.94%)		
k_{eq2}	[pH^{-2}]	−1.8564 (±3.18%)		
k_{kin}	[s^{-1}]	0.2743 (±4.98%)		
K_S	[M^{-1}]	−1.185 (±25.40%)		

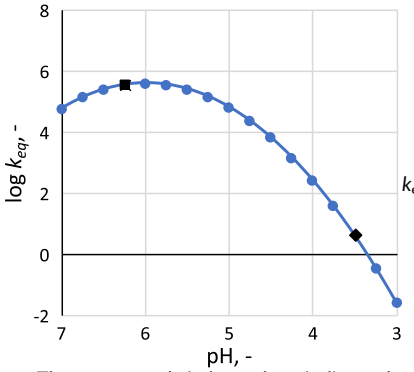

k_{eq} plot of CPA parameters. The square and circle markers indicate the pH value of the loading buffer and elution buffer, respectively.

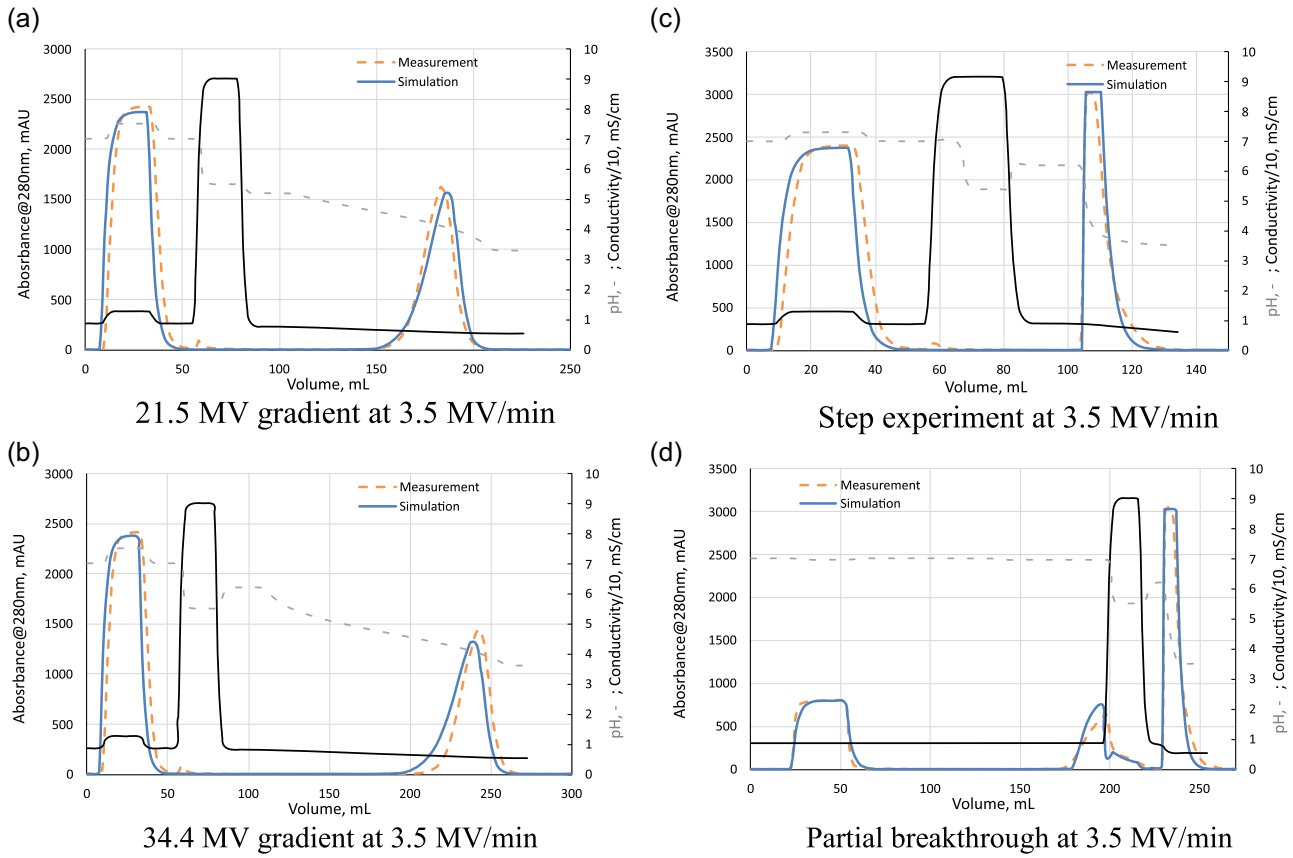

FIGURE 3 Model calibration on ÄKTA avant 150 with small scale Fibro PrismA. The orange, dashed line represents the experimental results, the blue, solid line the simulated UV curve. The grey, dash-dotted line represents the pH, the conductivity signal is printed in black.

confirmed for the loading buffer conditions at pH 6.2. Desorption conditions are present when injecting the elution buffer (pH 3.5), as log k_{eq} becomes smaller than 1. For comparison, the log k_{eq} value reported in Lane (2018) for a different mAb and adsorber combination at pH 7 was 3–4 which is similar to the magnitude reported here. The inverse value of k_{kin}, which is approximately 3.65, is within in the range of 0.75–10 reported for IgG's in Sandoval et al. (2012); and the slightly negative K_s value is in the same order of magnitude as observed for the pH-controlled mixed-mode process in Hahn et al. (2022).

4.3 | Influence of flow rate on mAb-Fibro interactions

To investigate the influence of the flow rate on adsorption/desorption processes in detail, experiments with various flow rates were performed with a HiTrap Fibro unit, which was overloaded with a second mAb (exemplary breakthrough curves are illustrated in Figure 4a, left) and eluted with a pH step (see Figure 4a, right). The mAb breakthrough curves indicate that the attainable dynamic binding capacity at 50% breakthrough increases slightly with decreasing flow rate.

This might be caused by the probability of mAb/ligand interaction increasing the slower the flow conditions are. Besides, some binding sites might be more likely reachable by diffusion, even when this is not a substantial factor in this convection-dominated system. For flow rates faster than 10 MV/min, the observed behavior did not change further in this study. The breakthrough curves overlap and indicate no further reduction in accessibility of binding sites or unfavorable binding kinetics. From a modeling perspective, neither the equilibrium term nor the blocking function of the chosen model can be flow dependent by definition. The kinetic constant might be considered flow-dependent such that a higher flow rate decreases the (re-) binding likelihood. However, the desorption rate seems unaffected as the elution peak tailing is similar for different flow rates. Thus, to describe the observed behavior under slower flow, a major rework of the model structure is needed, as well as more precise experimental data, which are beyond the scope of this study.

Transferring these findings to the main case study, it was to be expected that an increase of the flow rate from 4 to 8 MV/min would

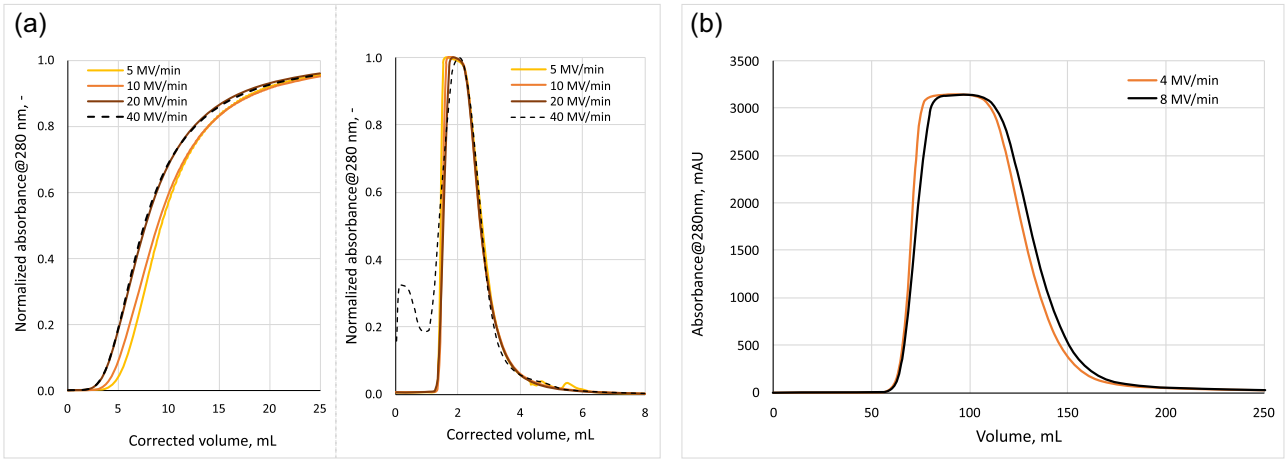

FIGURE 4 Two studies of flow rate dependent adsorption/desorption effects. (a) The presented experiments were performed with a second mAb species on an ÄKTA avant with HiTrap Fibro PrismA. Left: breakthrough curves at different flow rates. Right: pH-step induced elution. (b) The presented experimental curves show an overlay of the elution peaks at 4 and 8 MV/min performed on ÄKTA pilot 600 with 40 mL Fibro prototype. For better visualization, the *x*-axis begins with the respective starting point of the individual process step, that is, the loading phase or elution phase.

have little influence on the elution peak shape of the mAb capture step experiments. The result of such an experiment with the ÄKTA pilot 600 and the 40 mL Fibro unit is shown in Figure 4b. The elution peak shapes are similarly curved as hypothesized, therewith confirming the observations made with the HiTrap unit. Thus, adsorption model parameter determination can be done at a constant flow rate with low risk of loss of predictive power as long as the unit is not overloaded.

4.4 | Model validation and scale-up

The model validity for an elevated flow rate of 7 MV/min at lab-scale was evaluated with a partial breakthrough and a step elution experiment illustrated in Figure 5a. As expected, no significant change in peak shape in either the model or the experimental data occurred. The goodness of fit for the breakthrough and elution peak is the same as for the low flow rate.

Next, the standard step elution experiment was scaled up in silico. Initially, the same ratio of $D_{app,salt}$ to $D_{app,mAb}$ as observed for the lab-scale system was used to predict the outcome of the step elution experiment on the ÄKTA pilot system with 40 mL Fibro unit. However, the calculated $D_{app,mAb} = 0.72\ mm^2/s$ lead to an increased peak tailing compared to the experimental chromatogram (data not shown). A re-estimation of the $D_{app,mAb}$ parameter for the pilot Fibro unit for both flow rates lead to the values given in Table 4. $D_{app,mAb}$ was found to be 10 times larger then $D_{app,salt}$ but not 30 times larger as for the lab-scale unit. One possible cause could be that D_{app} does not only model the dispersive effects along the functionalized membrane, but also the back mixing at the inlet according to Equation (7). The fact that the flow path is split for the lab-scale prototype (c.f (HiTrap™ Fibro PrismA and HiScreen™ Fibro PrismA units datafile, 2022)) but not for the other scales may account for differences in mixing behavior. In contrast, the further scale-up from 40 to 160 mL worked as expected with the same newly determined $D_{app,mAb} = 0.24\ mm^2/s$ value at 4 MV/min.

The resulting chromatograms for the ÄKTA pilot system with the 40 mL Fibro unit and two different flow rates are shown in Figure 5b and for the ÄKTA ready system with 160 mL Fibro unit for 4 MV/min in Figure 5c. The simulated curves result from using the system-specific fluid dynamic model (Figure 2) together with the determined adsorption model parameters from Section 4.2.

All runs show very good agreement with the simulated curves. This confirms that accurate scale-up predictions are possible if the model is calibrated with few a laboratory-scale experiments and if the differences in system configuration and fluid dynamics are taken into account. The protein-ligand interactions can be assumed to be scale-invariant.

As shown in Table 5, the measured and predicted elution pool volume and mAb yield are overall, in good agreement. The reduced yield of the pilot scale experiment is likely caused by the visible breakthrough at the end of the load phase which was not predicted by the simulation. Overall, the consistently high yields and fast processing times show that Fibro units are a potential alternative to standard bead-based protein A resins.

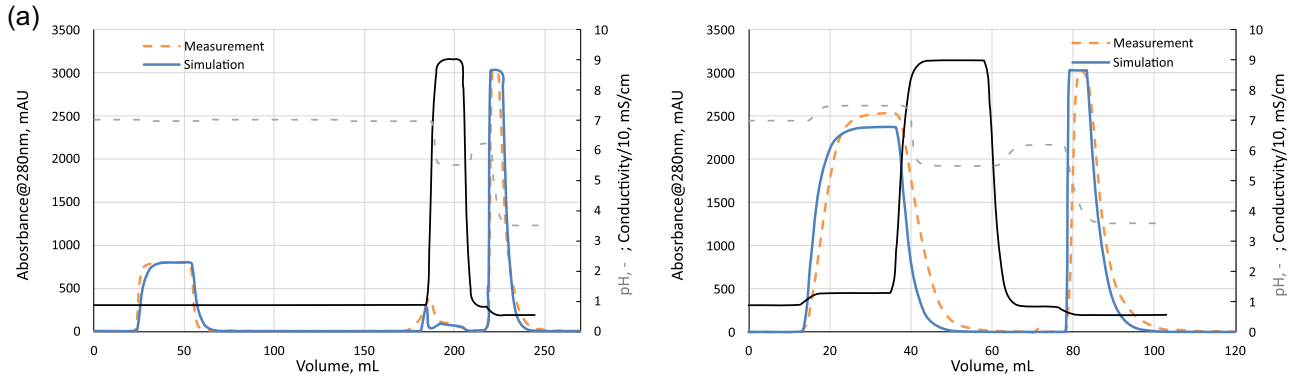

Laboratory scale: Partial breakthrough experiment (left) and step elution (right) at 7 MV/min on ÄKTA avant with 4.3 mL small scale Fibro unit

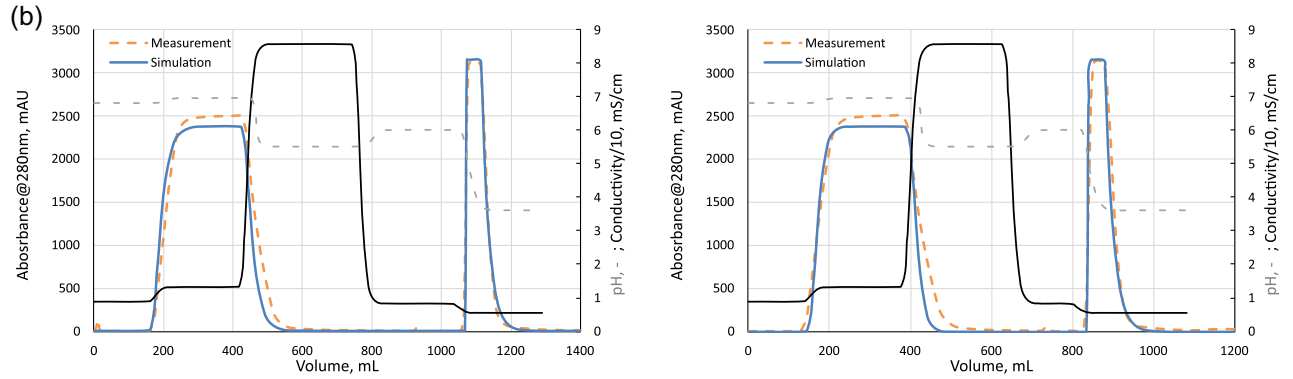

Medium scale: Step experiments at 4 MV/min (left) and 8 MV/min (right) on ÄKTA pilot 600 with 40 mL Fibro unit

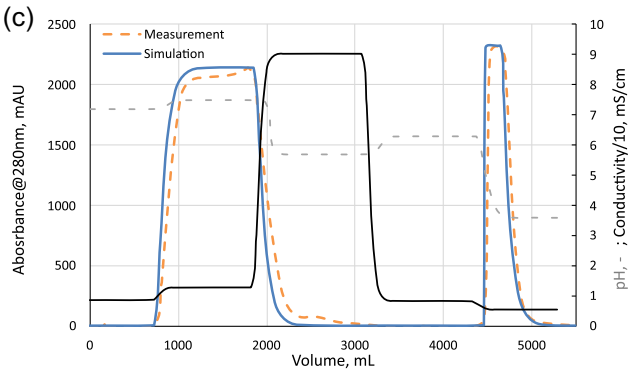

Pilot scale: Step experiment at 4 MV/min on ÄKTA ready with 160 mL Fibro unit

FIGURE 5 Validation experiments at different scales. The orange, dashed line represents the experimental chromatogram; the blue, solid line the simulated UV curve. pH is shown as dash-dotted line in grey, the conductivity signal as solid line in black.

TABLE 5 Comparison of mAb fraction yield predicted by simulation and validated experimentally for the step experiments at 3.5 or 4 MV/min at different scales.

Scale	Experimental results		Simulation predictions	
	Fraction volume (MV)	Yield (%)	Fraction volume (MV)	Yield (%)
ÄKTA avant with small scale Fibro unit	5.3	97.8	5.6	99.9
ÄKTA pilot with 40 mL Fibro unit	3.0	97.4	3.0	98.8
ÄKTA ready with 160 mL Fibro unit	3.5	94.5	3.2	99.2

5 | CONCLUSIONS

In this study, we examined three different sized Fibro PrismA prototypes experimentally and simulatively. To be able to distinguish precisely between scale-independent thermodynamics and scale-dependent fluid dynamics, a thorough system characterization with pulse experiments with and without a Fibro unit inline was carried out for each scale. The thermodynamic model was then only calibrated on laboratory scale. To describe the affinity chromatography, the surface coverage function from the colloidal particle adsorption model was used in combination with a pH-dependent stoichiometric model and a finite rate of adsorption kinetics. Separating the flow rate-dependent system and device characteristics from the mAb adsorption, the lab-scale-calibrated model could be applied successfully to predict elevated flow rates as well as the behavior of the 9- to 37-fold larger medium-scale and pilot-scale prototypes. As only four experiments with mAb feedstock were used for model calibration, the presented method allows rapid development of fiber-based protein A processes with limited material expenditure, and subsequent scale-up using only few pulse experiments for system characterization.

ACKNOWLEDGMENTS

The authors thank Till Briskot, who developed the type of adsorption models used in Hahn et al. (2022), as well as this study, and thus created an essential basis for this work.

CONFLICTS OF INTEREST STATEMENT

The authors affiliated to Cytiva declare, that the HiTrap Fibro PrismA unit, the ÄKTA systems, as well as the software packages UNICORN and GoSilico Chromatography Modeling Software used in the manuscript are commercial products from Cytiva.

DATA AVAILABILITY STATEMENT

Research data are not shared.

ORCID

Tobias Hahn http://orcid.org/0000-0001-7030-2037

Tatjana Trunzer https://orcid.org/0000-0003-4444-0860

REFERENCES

Agarwal, S., & Mierle, K. (2022). *Ceres solver*. The Ceres Solver Team. https://github.com/ceres-solver/ceres-solver

ÄKTA Avant Chromatography System. https://www.cytivalifesciences.com/en/us/shop/chromatography/chromatography-systems/akta-avant-p-06264

ÄKTA Pilot 600 Chromatography System. https://www.cytivalifesciences.com/en/us/solutions/bioprocessing/products-and-solutions/downstream-bioprocessing/akta-pilot-600

ÄKTA Ready and ÄKTA Ready XL Flow Kits. https://www.cytivalifesciences.com/en/us/shop/chromatography/chromatography-flow-kits/akta-ready-flow-kits-p-04247

Benner, S. W., Welsh, J. P., Rauscher, M. A., & Pollard, J. M. (2019). Prediction of lab and manufacturing scale chromatography performance using mini-columns and mechanistic modeling. *Journal of Chromatography A*, *1593*, 54–62. https://doi.org/10.1016/j.chroma.2019.01.063

Briskot, T., Hahn, T., Huuk, T., & Hubbuch, J. (2021). Protein adsorption on ion exchange adsorbers: A comparison of a stoichiometric and non-stoichiometric modeling approach. *Journal of Chromatography A*, *1653*, 462397. https://doi.org/10.1016/j.chroma.2021.462397

Briskot, T., Hahn, T., Huuk, T., Wang, G., Kluters, S., Studts, J., Wittkopp, F., Winderl, J., Schwan, P., Hagemann, I., Kaiser, K., Trapp, A., Stamm, S. M., Koehn, J., Malmquist, G., & Hubbuch, J. (2021). Analysis of complex protein elution behavior in preparative ion exchange processes using a colloidal particle adsorption model. *Journal of Chromatography A*, *1654*, 462439. https://doi.org/10.1016/j.chroma.2021.462439

Czok, M., & Guiochon, G. (1990). Aligned fiber columns for size-exclusion chromatography. *Journal of Chromatography A*, *506*, 303–317. https://doi.org/10.1016/s0021-9673(01)91586-9

Dimartino, S., Boi, C., & Sarti, G. C. (2011). Influence of protein adsorption kinetics on breakthrough broadening in membrane affinity chromatography. *Journal of Chromatography A*, *1218*(26), 3966–3972. https://doi.org/10.1016/j.chroma.2011.04.062

Gavara, P., Bibi, N., Sanchez, M., Grasselli, M., & Fernandez-Lahore, M. (2015). Chromatographic characterization and process performance of column-packed anion exchange fibrous adsorbents for high throughput and high capacity bioseparations. *Processes*, *3*(1), 204–221. https://doi.org/10.3390/pr3010204

Gavara, P. R., Cabrera, R., Vennapusa, R. R., Grasselli, M., & Fernandez-Lahore, M. (2012). Preparation, characterization, and process performance of composite fibrous adsorbents as cation exchangers for high throughput and high capacity bioseparations. *Journal of Chromatography B*, *903*, 14–22. https://doi.org/10.1016/j.jchromb.2012.06.027

Ghose, S., Hubbard, B., & Cramer, S. M. (2007). Binding capacity differences for antibodies and Fc-fusion proteins on protein A chromatographic materials. *Biotechnology and Bioengineering*, *96*(4), 768–779. https://doi.org/10.1002/bit.21044

Hahn, R., Bauerhansl, P., Shimahara, K., Wizniewski, C., Tscheliessnig, A., & Jungbauer, A. (2005). Comparison of protein A affinity sorbents. *Journal of Chromatography A*, *1093*(1–2), 98–110. https://doi.org/10.1016/j.chroma.2005.07.050

Hahn, R., Schlegel, R., & Jungbauer, A. (2003). Comparison of protein A affinity sorbents. *Journal of Chromatography B*, *790*(1–2), 35–51. https://doi.org/10.1016/s1570-0232(03)00092-8

Hahn, T., Geng, N., Petrushevska-Seebach, K., Dolan, M. E., Scheindel, M., Graf, P., Takenaka, K., Izumida, K., Li, L., Ma, Z., & Schuelke, N. (2023). Mechanistic modeling, simulation, and optimization of mixed-mode chromatography for an antibody polishing step. *Biotechnology Progress*, *39*, 3316. https://doi.org/10.1002/btpr.3316

Hahn, T., Huuk, T., Heuveline, V., & Hubbuch, J. (2015). Simulating and optimizing preparative protein chromatography with ChromX. *Journal of Chemical Education*, *92*(9), 1497–1502. https://doi.org/10.1021/ed500854a

Hahn, T., Wang, G., Läufer, T., Vasalas Peralvarez, M., Huuk, T., & Hubbuch, J., (2018). *Mechanistic extension of a hydrophobic interaction chromatography model to account for pH changes and mixed-mode binding*. Presented at Recovery of Biological Products XVIII, October 8, 2018.

Hardick, O., Dods, S., Stevens, B., & Bracewell, D. G. (2012). Nanofiber adsorbents for high productivity downstream processing. *Biotechnology and Bioengineering*, *110*(4), 1119–1128. https://doi.org/10.1002/bit.24765

Hardick, O., Dods, S., Stevens, B., & Bracewell, D. G. (2015). Nanofiber adsorbents for high productivity continuous downstream processing. *Journal of Biotechnology*, *213*, 74–82. https://doi.org/10.1016/j.jbiotec.2015.01.031

Hindmarsh, A. C., Brown, P. N., Grant, K. E., Lee, S. L., Serban, R., Shumaker, D. E., & Woodward, C. S. (2005). SUNDIALS. *ACM Transactions on Mathematical Software*, *31*(3), 363–396. https://doi.org/10.1145/1089014.1089020

HiTrap™ Fibro PrismA and HiScreen™ Fibro PrismA Units Datafile, (2022). https://cdn.cytivalifesciences.com/api/public/content/digi-33339-pdf

Hjelm, H., Hjelm, K., & Sjöquist, J. (1972). Protein A from *Staphylococcus aureus*. Its isolation by affinity chromatography and its use as an immunosorbent for isolation of immunoglobulins. *FEBS Letters*, *28*(1), 73–76. https://doi.org/10.1016/0014-5793(72)80680-x

Hunt, S., Larsen, T., & Todd, R. J. (2017). Modeling preparative cation exchange chromatography of monoclonal antibodies. In *Preparative Chromatography for Separation of Proteins* (pp. 399–427). https://doi.org/10.1002/9781119031116.ch13

Ingber, L., (1993). Adaptive simulated annealing (ASA). https://github.com/ingber/adaptive-simulated-annealing

Kelley, B., Blank, G., & Lee, A. (2008). Downstream processing of monoclonal antibodies: Current practices and future opportunities. In *Process Scale Purification of Antibodies*, (pp. 1–23). https://doi.org/10.1002/9780470444894.ch1

King, J.-K., & Pinto, N. G. (1992). Short fibrous supports for preparative chromatographic separations of biomolecules. *Journal of Chromatography A*, *609*(1–2), 61–68. https://doi.org/10.1016/0021-9673(92)80149-o

Lane, V. (2018). *Computational characterization of protein A—Antibody binding*, Carnegie Mellon University. https://doi.org/10.1184/R1/7571438.V1

Lienqueo, M. E., Mahn, A., Salgado, J. C., & Shene, C. (2011). Mathematical modeling of protein chromatograms. *Chemical Engineering & Technology*, *35*(1), 46–57. https://doi.org/10.1002/ceat.201100282

Liu, H. F., Ma, J., Winter, C., & Bayer, R. (2010). Recovery and purification process development for monoclonal antibody production. *mAbs*, *2*(5), 480–499. https://doi.org/10.4161/mabs.2.5.12645

Marcus, R. K., Davis, W. C., Knippel, B. C., LaMotte, L., Hill, T. A., Perahia, D., & Jenkins, J. D. (2003). Capillary-channeled polymer fibers as stationary phases in liquid chromatography separations. *Journal of Chromatography A*, *986*(1), 17–31. https://doi.org/10.1016/s0021-9673(02)01835-6

Mollerup, J. M. (2006). Applied thermodynamics: A new frontier for biotechnology. *Fluid Phase Equilibria*, *241*(1–2), 205–215. https://doi.org/10.1016/j.fluid.2005.12.037

Mollerup, J. M. (2008). A review of the thermodynamics of protein association to ligands, protein adsorption, and adsorption isotherms. *Chemical Engineering & Technology*, *31*(6), 864–874. https://doi.org/10.1002/ceat.200800082

Montes Sanchez, F. J., Martin del Valle, E., Galan Serrano, M. A., & Cerro, R. L. (2004). Modeling of monolith-supported affinity chromatography. *Biotechnology Progress*, *20*(3), 811–817. https://doi.org/10.1021/bp034343n

Pabst, T. M., Thai, J., & Hunter, A. K. (2018). Evaluation of recent protein A stationary phase innovations for capture of biotherapeutics. *Journal of Chromatography A*, *1554*, 45–60. https://doi.org/10.1016/j.chroma.2018.03.060

Podgornik, A. (2022). Characterization of a convection-based support microstructure through a flow resistance parameter. *Journal of Separation Science*, *45*(12), 1984–1996. https://doi.org/10.1002/jssc.202100955

Ramos-de-la-Peña, A. M., González-Valdez, J., & Aguilar, O. (2019). Protein A chromatography: Challenges and progress in the purification of monoclonal antibodies. *Journal of Separation Science*, *42*(9), 1816–1827. https://doi.org/10.1002/jssc.201800963

Reck, J. M., Pabst, T. M., Hunter, A. K., Wang, X., & Carta, G. (2015). Adsorption equilibrium and kinetics of monomer–dimer monoclonal antibody mixtures on a cation exchange resin. *Journal of Chromatography A*, *1402*, 46–59. https://doi.org/10.1016/j.chroma.2015.05.007

Sandoval, G., Andrews, B. A., & Asenjo, J. A. (2012). Elution relationships to model affinity chromatography using a general rate model. *Journal of Molecular Recognition*, *25*(11), 571–579. https://doi.org/10.1002/jmr.2223

Schwan, P. (2019). *Prot-A capture model—From batch to continuous*. Presented at Chromatography Modeling Days, May 28, 2019.

Seidel-Morgenstern, A. (2020). Modeling of chromatographic processes. In *Preparative Chromatography*, (pp. 311–354). https://doi.org/10.1002/9783527816347.ch6

Shukla, A. A., Hubbard, B., Tressel, T., Guhan, S., & Low, D. (2007). Downstream processing of monoclonal antibodies—Application of platform approaches. *Journal of Chromatography B*, *848*(1), 28–39. https://doi.org/10.1016/j.jchromb.2006.09.026

Singh, A., & Pinto, N. G. (1995). Polymeric short-fiber chromatographic supports for downstream processing of biomolecules. *Reactive Polymers*, *24*(3), 229–242. https://doi.org/10.1016/0923-1137(94)00088-m

Tejeda-Mansir, A., Montesinos, R., & Guzmán, R. (2001). Mathematical analysis of frontal affinity chromatography in particle and membrane configurations. *Journal of Biochemical and Biophysical Methods*, *49*(1–3), 1–28. https://doi.org/10.1016/s0165-022x(01)00196-8

Thomas, H. C. (1944). Heterogeneous ion exchange in a flowing system. *Journal of the American Chemical Society*, *66*(10), 1664–1666. https://doi.org/10.1021/ja01238a017

Winderl, J., Hahn, T., & Hubbuch, J. (2016). A mechanistic model of ion-exchange chromatography on polymer fiber stationary phases. *Journal of Chromatography A*, *1475*, 18–30. https://doi.org/10.1016/j.chroma.2016.10.057

Yamamoto, S., Nakanishi, K., Matsuno, R., & Kamikubo, T. (1983). Ion exchange chromatography of proteins prediction of elution curves and operating conditions. I. Theoretical considerations. *Biotechnology and Bioengineering*, *25*(6), 1465–1483. https://doi.org/10.1002/bit.260250605

Yang, Y., Velayudhan, A., Ladisch, C. M., & Ladisch, M. R. (1992). Protein chromatography using a continuous stationary phase. *Journal of Chromatography A*, *598*(2), 169–180. https://doi.org/10.1016/0021-9673(92)85045-u.

SUPPORTING INFORMATION

Additional supporting information can be found online in the Supporting Information section at the end of this article.

Received: 30 January 2023 | Revised: 11 September 2023 | Accepted: 21 September 2023

DOI: 10.1002/bit.28572

ARTICLE

BIOTECHNOLOGY AND BIOENGINEERING WILEY

High throughput screening for rapid and reliable prediction of monovalent antibody binding behavior in flowthrough mode

Julius Klemens Lorek | Hanne Sophie Karkov | Finn Matthiesen | Maria Dainiak

Purification Technologies, Novo Nordisk A/S, Maaloev, Denmark

Correspondence
Maria Dainiak, Purification Technologies, Novo Nordisk A/S, DK-2760 Maaloev, Denmark.
Email: MD@NOVONORDISK.com

Funding information
Novo Nordisk A/S

Abstract

Flowthrough (FT) anion exchange (AEX) chromatography is a widely used polishing step for the purification of monoclonal antibody (mAb) formats. To accelerate downstream process development, high throughput screening (HTS) tools have proven useful. In this study, the binding behavior of six monovalent mAbs (mvAbs) was investigated by HTS in batch binding mode on different AEX and mixed-mode resins at process-relevant pH and NaCl concentrations. The HTS entailed the evaluation of mvAb partition coefficients (K_p) and visualization of results in surface-response models. Interestingly, the HTS data grouped the mvAbs into either a strong-binding group or a weak-binding/FT group independent of theoretical Isoelectric point. Mapping the charged and hydrophobic patches by in silico protein surface property analyses revealed that the distribution of patches play a major role in predicting FT behavior. Importantly, the conditions identified by HTS were successfully verified by 1 mL on-column experiments. Finally, employing the optimal FT conditions (7–9 mS/cm and pH 7.0) at a mini-pilot scale (CV = 259 mL) resulted in 99% yield and a 21–23-fold reduction of host cell protein to <100 ppm, depending on the varying host cell protein (HCP) levels in the load. This work opens the possibility of using HTS in FT mode to accelerate downstream process development for mvAb candidates in early research.

KEYWORDS
flowthrough chromatography, high throughput screening

1 | INTRODUCTION

Pharmaceutical antibody products have become one of the most important therapeutic modalities in the biopharmaceutical industry. The importance of developing an efficient downstream process (DSP) for the recovery and purification of monoclonal antibodies (mAbs) is underlined by its significant proportion of the total manufacturing costs (Hummel et al., 2019; Shukla et al., 2007). Generally, commercial production of mAbs is based on a platform process that includes affinity capture on ProteinA-based chromatography resin followed by purification and polishing steps by cation exchange (CEX) and anion exchange (AEX) or mixed mode (MM) chromatography. Variations to the process include hydrophobic interaction (HIC) and hydroxyapatite chromatography (Chahar et al., 2020; Liu et al., 2010; Shukla et al., 2007). Platform strategies together with the implementation of integrated continuous manufacturing allow for a considerable reduction of manufacturing costs (Chahar et al., 2020; Cooney & Konstantinov, 2015; Feidl et al., 2020; Ichihara et al., 2018; Khanal & Lenhoff, 2021; Rathore et al., 2015). However, the platform approach only defines the overall purification scheme. Optimization of DSP unit operations is required for new mAb-based drug candidates due to significant physicochemical differences among mAbs and emerging novel mAb modalities, for example, bispecific, monovalent and sweeping mAbs (Igawa et al., 2016; Merchant et al., 2013; Saleh et al., 2021; Shukla et al., 2007; Spiess et al., 2015) that behave differently in the chromatographic steps. One amino acid substitution

of tryptophan with lysine in the H-CDR3 was shown to have an impact on chromatographic behavior in CEX (Saleh et al., 2021). Thus, the speed and high costs of DSP development remain challenging in bringing new pharmaceutical mAbs to the market.

Automation and miniaturization by high throughput process development (HTPD) allows for significant reduction of process development costs and time-to-market. High throughput screening (HTS) methods in robotic format provide fast and systematic screening of a broad range of process parameters of mAb variants during the selection of lead candidates. Batch binding screening in combination with mechanistic and molecular modeling are powerful tools in HTPD (Bensch et al., 2005; Coffman et al., 2008; Gronemeyer et al., 2014; Nfor et al., 2010; Silva et al., 2022). 96-well plate is a widely used format in HTS of chromatographic parameters (Bergander et al., 2008; Charlton, 2006; Coffman et al., 2008; Dainiak et al., 2006; Kelley et al., 2008; Liu et al., 2006; McDonald et al., 2016; Stein & Kiesewetter, 2007). Application of RoboColumns (Wiendahl et al., 2008), 96-well column formats Atoll-Bio (Wierling et al., 2007), and miniaturization to 384-well format and microfluidics have also been described (Kittelmann et al., 2015; Silva et al., 2022).

Cramer et al. have used the 96-well membrane-bottomed plates across different studies to screen displacers for displacement chromatography (Cramer et al., 2005; Rege et al., 2005). Microtiter filter plates filled with a well-defined volume of chromatography resins have been applied for the determination of dynamic binding capacity (Bergander et al., 2008) and HTS of chromatographic separations (Coffman et al., 2008; McDonald et al., 2016). Application of monolithic mini-columns in 96-well plate format for screening for optimal conditions for the separation of cells and for affinity tags for immobilized metal affinity chromatography have also been described (Dainiak et al., 2006; Hanora et al., 2005).

mAbs have been subject to HTS studies on many different types of resins for positive chromatography in bind-elute mode. Kramarczyk et al. screened the batch binding and elution conditions (pH and salt) for the separation of mAbs from aggregates on different HIC resins (Kramarczyk et al., 2008). Wensel et al. used HTS for identifying optimal purification conditions of a mAb selection on ceramic hydroxyapatite by evaluating the partition coefficient (K_p) of mAbs with changing salt concentration and pH (Wensel et al., 2008). Kelley et al. designed a screen for an adsorptive CEX step to determine salt concentrations to effectively bind and elute an mAb on eight different CEX resins at four given pH. They successfully identified differences in binding affinity between the tested resins, which is apparent by comparing the elution profiles of the HTS (Kelley et al., 2008). McDonald et al. applied an HTS for evaluating the binding behavior of a library of eight mAbs on two different CEX resins with changing pH and counterion concentrations. They used K_p for mapping the binding of mAbs and impurities. Various findings from the logK_p screen could be verified in experiments made on packed-bed columns. The logK_p screen exceled as an adequate predictor for mAb binding behavior on CEX resins because tendencies in elution time of selected mAbs in a gradient could be predicted, the end of an elution in a gradient could be correlated to logK_p with high accuracy and the elution pool volume could be estimated based on the logK_p screens. Furthermore, trends in high molecular weight protein (HMWP) and host cell protein (HCP) clearance could be confirmed on packed beds with the help of cross plots and separation factor analysis.

In the mAb purification platform, positive chromatography steps are generally followed by negative AEX, MM, or HIC chromatography steps to provide further clearance of HCPs, nucleic acids, aggregates, and endotoxin. Flowthrough (FT) mode purifications have become an integral part of continuous manufacturing processes (Feidl et al., 2020; Ichihara et al., 2018; Khanal & Lenhoff, 2021) and have been successfully applied for the purification of new mAb modalities, for example, knob-into-hole bispecific mAbs (Chen et al., 2022). Several HTS studies have been described for optimization of the FT chromatography. Chen et al. have screened pH and salt concentrations for FT chromatography on Capto Adhere ImpRes and Capto Butyl ImpRes to identify optimal conditions for the removal of HMWP during the purification of bispecific mAbs (Chen et al., 2022). Design of experiment (DOE) screening in 96-well plates was conducted to evaluate product yield and clearance of HCP and DNA as a function of pH and conductivity in an integrated FT purification of mAbs on activated carbon, AEX, and CEX resins (Ichihara et al., 2018). mAb loading up to 1500 mg mAb/mL resin was used in the screenings. Petroff et al. employed batch binding screens for FT AEX of mAbs in 96-well filter plates as one of the high throughput (HTP) chromatography strategies to provide a systematic approach for establishing characterization testing ranges for formal characterization of biotherapeutic processes. The testing ranges identified in batch binding screens provided narrower DOE testing ranges and earlier identification of nonlinear performance regions (Petroff et al., 2016). Kelley et al. have described an analysis of mAb adsorption on AEX resins at 48 different combinations of pH and counterion concentrations for the FT step (Kelley et al., 2008). Two protein loads were evaluated: 5 mg/mL giving a K_p value in the linear region of the equilibrium binding isotherm, and 133 mg/mL which is close to the equilibrium binding capacity Q_{133}. A close correlation of Q_{133} to the logK_p was observed, showing a nearly linear dependency over a wide range of these parameters. To challenge the resins with high protein load, filter plate configuration in which fluid passes through the small volume of resin by means of centrifugation or vacuum filtration had to be employed. Though less than 500 mg of protein was used for screening, further reduction of protein amounts may be required when screening libraries of mAb-based drug candidates for processability on multiple resins, either due to low levels of expression of mAb variants in the early research phase or due to the necessity to perform many various screening assays limiting compound's availability.

The present study investigates the correlation of K_p values from batch binding data obtained with low protein load on AEX and MM resins with the yield obtained in the FT on-column tests to enable fast identification of conditions suitable for scale-up and minimizing further the amount of protein required for process development.

The described method is done in robotic format and employs a binding phase in suspension followed by centrifugation and transfer of the supernatants to a 96-well analytical plate for measuring nonbound protein. A similar batch binding method has been used for protein-purification-parameter screening method in deep-well plates allowing the processing of crude extracts (Thiemann et al., 2004).

In this study interactions of six monovalent antibodies (mvAbs) differing in mutations in Fc fragment with AEX and MM resins were investigated. Evaluation of adsorption on HIC resins at low NaCl concentrations was included in the study to elucidate the hydrophobic nature of the mvAb interactions in comparison to the MM ligands. HIC in FT mode under no-salt conditions have been previously described for the purification of mAbs (Ghose et al., 2013).

The nature of patch-dominated retention has been discussed in the literature for many years (Brown et al., 2018; Robinson et al., 2018; Roush et al., 1994). To improve the understanding of the mvAbs–resin interactions in the present paper, in silico protein surface property analyses were conducted employing electrostatic potential (EP) maps and spatial-aggregation propensity (SAP) tools. The latter was originally developed for the identification of hydrophobic aggregation-prone motifs in mAbs (Chennamsetty, Helk, et al., 2009). Previously, EP and SAP maps have been shown to be valuable tools in providing insight into molecular interactions of complex proteins with chromatographic ligands and explaining unique multimodal selectivity (Karkov, Krogh, et al., 2015; Karkov, Woo, et al., 2015; Robinson et al., 2018, 2020; Sakhnini et al., 2019). In silico molecular evaluations and modeling in concert with chromatographic investigations were also applied for creating quantitative structure-activity relation models to predict the elution behavior of Fabs on various resins (Robinson et al., 2017). Saleh et al. introduced a multiscale model based on homology modeling, quantitative structure–property relationships, and mechanistic chromatography modeling for in silico prediction of elution profiles of mAbs in CEX (Saleh et al., 2023). The present study explores the potential of using HTS with in silico protein surface property tools to predict the behavior of complex molecules and accelerate the early-stage development of a chromatographic FT step.

2 | MATERIAL AND METHODS

2.1 | Production and preparation of mvAbs

The six homologous mvAbs were selected as representatives of a novel mAb format to address methods development and optimization of an FT polishing step using HTS. All six mvAbs had identical Fab fragments and differed merely by specific sets of mutations in the Fc fragment providing slight differences in the theoretical mass and Isoelectric point (pI) values (Table 1). The mvAbs were expressed transiently in a human embryonic kidney cell culture. The subsequent purification from the harvest was performed on an ÄKTA™ Xpress system in a two-step purification with capture on MabSelect™ SuRe™ (Cytiva) and preparative size-exclusion with Superdex ® 200 (Cytiva). The pooled fractions were analyzed with analytic SE-HPLC (Phenomenex BioSep-SEC-s3000 column) and had a purity of >95%. The masses of all six mvAbs were verified with liquid chromatography-mass spectrometry (Waters MassPREP Desalt - cat. no. 186004032). The concentration of the pools was determined based on a UV/Vis spectrum (A_{280}) with a Lunatic instrument from UNCHAINED LABS. Before the HTS experiment, the mAbs load solutions were buffer exchanged in 20 mM Bis-Tris, pH 6.5 buffer using PD-10 desalting columns (Cytiva). For the on-column AEX experiments, the mvAbs were buffer exchanged to 20 mM Bis-Tris, 70 mM NaCl. For the on-column MM runs, the mvAbs were buffer exchanged into 20 mM Bis-Tris, 150 mM NaCl, pH 5.0.

TABLE 1 List of tested mvAbs 1–6 with average theoretical mass in g/mol, molar extinction-coefficient in (1/cm×1/(g/L)), and theoretical pI which is calculated based on the primary sequence.

Antibody	Avg. mass (g/mol)	A280 Extinc. (1/cm×1/(g/L))	Theoretical pI
mvAb 1	98938.1	1.662	8.02
mvAb 2	98918.0	1.744	7.76
mvAb 3	98684.0	1.606	8.24
mvAb 4	98663.9	1.688	8.02
mvAb 5	98595.8	1.719	7.49
mvAb 6	98285.4	1.612	7.78

Abbreviations: mvAb, monovalent mAbs; pI, Isoelectric point.

2.2 | HTP batch binding experiments

The batch binding experiments were conducted with a Freedom Evo 200 robot (Tecan). The robot was equipped with a 96-multichannel liquid handling arm with exchangeable tips, a robot moving arm for moving plates, a BioShake 3000 (Q Instruments GmbH) for mixing of the batch mixtures and an integrated Hettich centrifuge Rotana 46 RSC (Andreas Hettich GmbH & Co. KG) for separation of solid and liquid content. All tested resins including Poros 50 HQ, Source 30Q, Q Sepharose FF (AEX); Capto Adhere, Capto Adhere ImpRes (MM); Capto Phenyl, Phenyl Sepharose FF, Toyopearl SuperButyl 550-C (HIC) were stored in 20% v/v of 100% EtOH solution in H_2O at 4°C and washed with three repetitive cycles of centrifugation and resuspending in deionized water to remove the residual EtOH. After the last centrifugation, the resin solution was adjusted to 30% v/v in deionized water. A total of 40 µL of the 30% v/v in H2O-washed resin slurries was then added manually per well into the batch binding microtiter plate before placement on the Tecan robot. For the batch binding experiments on AEX and MM/HIC, two different setups were used. For the AEX batch binding experiments, three different pH conditions (pH 6.0, 6.5, 7.0) were evaluated. For pH 6.0 and 6.5, 20 mM His buffer with

300 mM NaCl buffer were mixed in different ratios, ending up with a tested range of 0–150 mM NaCl. For pH 7.0, a 25 mM Bis-Tris buffer was mixed with 25 mM Bis-Tris, 300 mM NaCl in different ratios. For MM and HIC, two different pH conditions (5.0 and 7.0) were tested. The pH 5.0 condition was established by mixing a 25 mM sodium acetate solution with 25 mM sodium acetate and 1 M NaCl, ending up with a tested range of 0–500 mM NaCl. For pH 7.0, 20 mM Bis-Tris was mixed with 20 mM Bis-Tris, 1 M NaCl in different ratios. The pH adjustment in the buffers was done by adding the required amounts of 1 M NaOH and 1 M HCl. The addition of the respective buffers (100 µL of total buffer in every well) into wells was performed by the Tecan robot. After adding 100 µL of buffer, 50 µL deionized water, and 10 µL of protein solution were added to the manually added 40 µL resin slurry, the microtiter plate was moved into the Bio Shake 3000 frame, where the microtiter plate was shaken for 10 min with a frequency of 3500 rpm. Thereafter, the Tecan robot moving arm placed the microtiter plate into the Hettich centrifuge, where a centrifugation step at 2000*g* for 10 min to separate resin and supernatant followed. The supernatant (=nonbound fraction) was then transferred into another 96-well plate for size-exclusion ultra performance liquid chromatography (SE-UPLC) analysis to determine the protein concentration in the nonbound fraction.

2.3 | On-column pulse experiments

The on-column experiments were performed with a column volume (CV) of 1 mL. Poros 50 HQ, Source 30Q, and Capto Adhere were packed manually in columns with 0.5 cm inner diameter, whereas Q Sepharose FF and Capto Adhere ImpRes were prepacked (HiTrap, inner diameter: 0.7 cm). The chromatography runs were performed on an ÄKTA™ 150 (Cytiva) evaluating the A_{280}-detected amount of protein in the FT fraction, which was defined as collected volume between sample application and the start of rise in conductivity. At the column outlet, parameters including UV absorption at 280 nm, pH, conductivity, and concentration of elution buffer were monitored. Recording and archiving of the chromatograms was performed by Unicorn 7.4. The program for the runs started with a 5 CV equilibration phase with equilibration buffer and a flow rate of 156 cm/h before the sample (adjusted to 5 mg/mL resin) was applied with a predefined volume followed by a 5–10 CV wash step with equilibration buffer. Equilibration buffer for AEX was 20 mM Bis-Tris, 70 mM NaCl, and for MM 20 mM Bis-Tris, 150 mM NaCl, pH 5.0. The three-step elution (36 CV) was performed with elution buffers consisting of 20 mM Bis-Tris, 500 mM NaCl, pH 7.0 for AEX, and 25 mM sodium acetate, 500 mM NaCl, pH 5.0 for MM. The first step of elution was 0%–20% elution buffer in 30 CV followed by 20%–100% elution buffer in 3 CV and ending with a 100% elution buffer hold for 3 CV. The flow rate for the load, wash, and elution steps was maintained at 31 CV/h, translating to 158 and 81 cm/h for the manually packed and prepacked columns, respectively.

2.4 | On-column scale-up experiments

The scale-up experiments were performed with 259 mL Poros 50 HQ (5 cm I.D.). The ÄKTA™ Avant 150 monitored UV absorption at 280 nm, pH, conductivity, and concentration of elution buffer. Monitoring and archiving the runs was performed by Unicorn 7.4. Two runs were performed under similar conditions. The program of the run started with a 2 CV equilibration with 25 mM Bis-Tris buffer pH 7.0 and a flow rate of 134 cm/h. The flow rate was consistent throughout the program, excluding cleaning in place (CIP) with 1 M NaOH where a flow rate of 61 cm/h was used. The loading phase, which is subsequent to the equilibration, was 38–39 CV. Following the load, the column was washed with an equilibration buffer (1 CV).

The load was coming from a previous CEX bind-and-elute chromatography step and was diluted with dilution buffer 75 mM Bis-Tris, pH 7.0 until a conductivity at 8–9 mS/cm and pH 7.0 were reached. Finally, an end volume of 9.73 L with a total protein amount of 36.6 g were reached as a load for run 1, whereas run 2 had a volume of 9.98 L with a protein amount of 42.7 g. Thus, the load was 141 and 165 mg/mL resin for run 1 and 2, respectively.

2.5 | Analytics

For controlling the adjustments of the load concentrations for HTP batch binding experiments as well as on-column experiments, an OD_{280} measurement with the Nanodrop 2000c spectrophotometer was performed. The measured absorption was then divided by the respective molar extinction coefficient (Table 1) to obtain the concentration in mg/mL.

The measurement of the protein concentrations in the nonbound fractions of the HTP batch binding experiments were measured with a SE-UPLC on a Waters Acquity H class UPLC instrument (Waters Corp.) with an ACQUITY UPLC Protein BEH SEC column (200 Å, 1.7 µm, 4.6 mm × 150 mm) from Phenomenex. The flow rate was adjusted to 0.3 mL/min and the temperature was 25°C. The optical path length was 1 cm. The running buffer was 50 mM NaH_2PO_4, 50 mM NaCl, 2-propanol (5% v/v), pH 6.8. For the analysis, 10 µL of sample were injected with an isocratic run time of 10 min per injection. The generated peaks were then integrated with the software Empower (Waters Corp.) and concentrations were calculated using the following equation:

Equation for calculation of concentration with A is the area at 280 nm in uV*s, Q is the flow rate in µL/sec, V is the injection volume in µL, ϵ is the molar extinction coefficient at 280 nm, c is the concentration in mg/mL.

$$c\ (\mathrm{mg/mL}) = A \times \frac{\frac{Q}{V}}{\epsilon} \times \frac{MW}{1000000}. \quad (1)$$

For the on-column experiments, the determination of the amount of protein recovered in the FT fraction was calculated from the peak area in the chromatograms using Unicorn 7.4 software. As for the 259 mL scale-up experiment, the measurement of protein content in

the FT fraction was performed by an analytic SE-HPLC with a BioSep-SEC-S3000 column (Phenomenex, 5 µm, 300 × 7.8 mm) integrated in the Waters Alliance HPLC system. The sample was run at 30°C with a flow rate of 1 mL/min for 20 min under isocratic conditions and a running buffer with the following composition: 78 mM NaH2PO4, 122 mM Na2HPO4, 300 mM NaCl, 2-propanol (10% v/v), pH 7.0 (RT). The protein was detected with measuring the absorbance at 280 nm. Again Equation (1) served to determine the concentration.

2.6 | Surface-response models

The K_p values were calculated from the amount of protein detected in solution after separating the solid and liquid phase with the following equation:

Formula for calculation of K_p value.

$$K_p = \frac{c(\text{bound protein})}{c(\text{nonbound protein})}. \quad (2)$$

For the creation of contour plots, a surface-response model was computed. Therefore, a function that returns the least-squares solution to a linear matrix equation was used. The function was then used to perform a second-order polynomial fit of the experimental data with two factors. As described by McDonald et al., the base-10 logarithm of the K_p values was computed for the model, to account for the wide range of measured K_p values (McDonald et al., 2016). With the model, a logK_p value as a function of pH and NaCl-concentration could be predicted based on Equation (3):

Formula used in the model for prediction of logK_p value where a, b, c, d, e and f are coefficients of the surface-response model fit.

$$Log\ K_p = a + b \times c(\text{NaCl}) + c \times \text{pH} + d \times c(\text{NaCl}) \times \text{pH} + e \times c(\text{NaCl})^2 + f \times \text{pH}^2. \quad (3)$$

For graphical means, the formula served to calculate a mesh, which was then visualized graphically in the contour plots. The contour plot is a visualization technique to display a three-dimensional (3D) function on a two-dimensional (2D) plot, where the variation in the response (logK_p, z-axis) as a function of two input variables (NaCl concentration (x-axis) and pH (y-axis)) is depicted.

The significance of each parameter in Equation (3) was classified as significant with a t test by McDonald et al. ($p \leq 0.05$) (McDonald et al., 2016).

For mapping the binding behavior with the logK_p value of all mvAbs in a surface-response model, the determined amounts of mvAb in the nonbound fraction were used as an input for the model and the highest measured protein response in each data set was determined as the protein load in the model. The logK_p range used for modeling was between 0 and 2 based on McDonald et al., as values <−0.5 and >2.5 are more prone to suffer from erroneous measurements (McDonald et al., 2016).

2.7 | Protein surface property analyses

Homology modeling was employed to create 3D structures of mvAb 1 and mvAb 4 using the drug discovery software program Molecular Operating Environment (MOE) version 2019-0102 developed by Chemical Computing Group. The homology model was created by the superposition of the Fab crystal structure of mvAb 1 and mvAb 4 on both Fab moieties of the full 1HZH.pdb antibody structure. The original 1HZH.pdb Fab moieties were removed, and new peptide bonds were created between the new Fab's and the 1HZH.pdb followed by structure preparation, protonation, and energy minimization of the final molecule using the standard protocols in MOE. Protein Patches were calculated using the Surfaces and Maps application with default settings. 2D maps were used to visualize and compare the calculated protein surface patches.

3 | RESULTS AND DISCUSSION

3.1 | HTP batch binding experiments can discover differences in binding behavior of homologous mvAbs on AEX and MM resins

The binding behavior of mvAbs 1–6 were initially evaluated in HTP batch binding experiments using the Tecan liquid handling system. All six mvAbs were screened on three AEX resins, two MM resins, and three HIC resins at varying pH and NaCl concentrations, which resulted in 152 tested conditions for each mvAb and 912 conditions for all six mvAbs. The experimental pH values were selected well below the theoretical pI of all mvAbs (Table 1) to allow nonbinding conditions for the FT step that is based on repulsive interactions between overall positive charges on the protein and positively charged ligands, although, patches of negative charge may still exist allowing the opportunity for retention. Indeed, despite meeting this requirement, the HTP batch binding experiments revealed that some of the mvAbs did bind.

Interestingly, when visualizing the binding data of the six mvAbs on Poros 50 HQ (AEX resin) at pH 7.0 and Capto Adhere (MM resin) at pH 5.0 in a gradient of increasing NaCl, the mvAbs could be distinguished into two different groups: a weak binding or FT group comprising mvAb 1, 3, and 6 that is represented by blue colors and a strong binding group which is represented by mvAbs 2, 4, and 5 in warm colors (Figure 1). At pH 7.0, approx. 80% of weak binding and 90%–100% of strong binding mvAbs were retained by Capto Adhere resin (Figure 1a). As seen in Figure 1, the weak binding mvAb group showed 86%–100% of detected mvAb in the nonbound fraction on AEX at 0–150 mM NaCl pH 7.0 and 76%–96% on MM resin at 0–70 mM NaCl and pH 5.0, whereas the stronger binding group exhibited a significantly lower level of nonbound mvAb on AEX resin at 0–100 mM NaCl (Figure 1b) and at all NaCl concentrations examined on MM resin at pH 5.0 (Figure 1c). On AEX, the curve shape of the group of strong binding mvAbs showed a sigmoidal shape representing a decreasing binding with increasing NaCl until

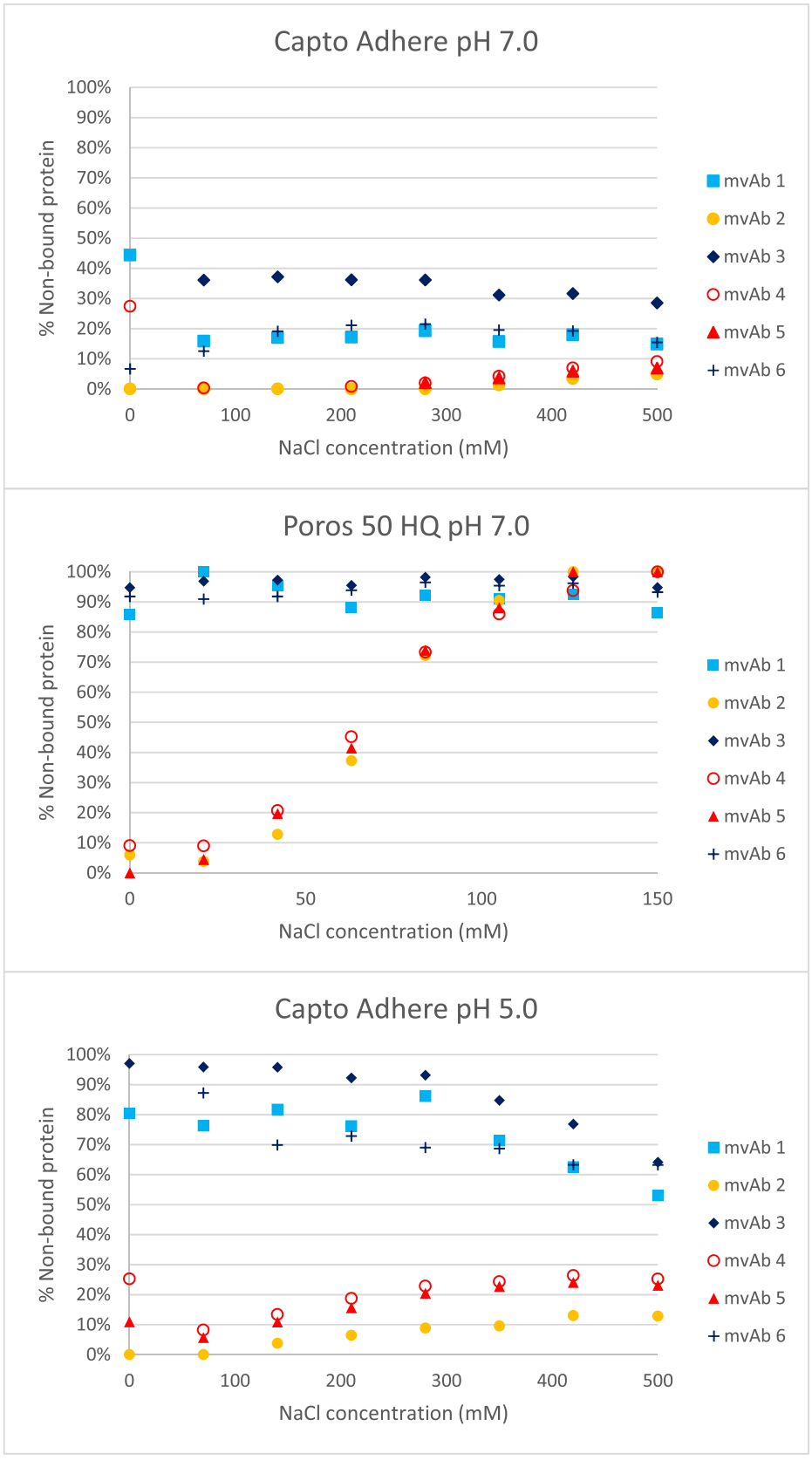

FIGURE 1 Percent of nonbound protein for high throughput screening batch binding experiments: a (top): Capto Adhere at pH 7.0 in NaCl range of 0–500 mM. b (middle): Poros 50 HQ at pH 7.0 in NaCl range of 0–150 mM. c (bottom): Capto Adhere at pH 5.0 in NaCl range of 0–500 mM.

86%–100% protein was nonbound at a NaCl concentration of >100 mM (Figure 1b). On MM resins, in contrast to the strong binding mvAbs, the weak binding mvAbs showed an increase of binding with rising NaCl whereas the strong binding mvAb groups showed the opposite behavior. These data indicate the different mechanisms of interactions between the two mvAb groups and MM ligands. Weak binding mvAbs showed increased retention with increasing NaCl concentrations starting after approx. 280 mM NaCl presumably due to increasing interaction with hydrophobic groups of the ligands. Strong binding mvAbs displayed a synergistic effect of hydrophobic and electrostatic interactions with the latter weakening as NaCl concentrations increased to 280 mM, where the amount of nonbound protein reached the plateau. Interestingly, despite having identical theoretical pI of 8.02, mvAb 1 and mvAb 4 behaved differently on Poros 50 HQ and Capto Adhere indicating that theoretical pI may be a poor predictor for mvAb binding behavior on AEX and MM resins (Table 1 and Figure 1) as in consistence with previous studies on correlations of protein pI and protein adsorption to ion exchanger (Noh et al., 2008). Furthermore, mAbs are prone to modifications that may occur during expression or due to chemical reactions giving rise to microheterogeneity and the presence of different pI isoforms. However, these charge variants are characterized by similarity of surface charge properties which makes their separations by IEX challenging (Baran et al., 2021). Separation of basic peaks in the force-oxidized mAbs by AEX-HPLC and separation by overloaded IEX and pH gradient have been described (Baran et al., 2021; Teshima et al., 2011).

Altogether, the two presented graphs in Figure 1 illustrate differences in binding behavior of homologous mvAbs on an AEX and MM resin that can be discovered in a fast and efficient way with miniaturized HTP batch binding experiments.

3.2 | logK_p-based surface-response models

In addition to the screen conducted on Poros 50 HQ and pH 7.0 (Figure 1b), the binding behavior of mvAbs 1–6 were also analyzed on further two AEX resins (Q Sepharose FF and Source 30Q) in a NaCl range from 0 to 150 mM at pH 6.0, 6.5, and 7.0. Figure 2 illustrates that mvAbs 1, 3, and 6 were found predominantly in the nonbound fraction at all studied conditions on all three AEX resins (dominating blue color). In contrast, mvAbs 2, 4, and 5 representing the mvAbs binding group showed retention on AEX resins with increasing pH at up to 100 mM NaCl. The contour plots show a clear difference in retention of mvAb 4 as compared with mvAbs 2 and 5. In particular, for mvAb 4 logK_p > 1 was observed around pH 7.0 on Poros 50 HQ and on Q Sepharose FF. MvAb 2 and mvAb 5 showed log K_ps > 1 even at pH 6.0–6.5 at up to 50 mM NaCl and logK_ps ~ 2.0 at pH 7.0 at up to 100–125 mM NaCl on all three resins. The data indicate that operating pH of 8.0–8.2 with a conductivity of up to 10 mS/cm which is normally used in the FT AEX step in the mAb platform process may not be applicable to the studied mvAbs (Liu et al., 2010). The difference in binding trends between the mvAbs points out the importance of screening for operating conditions.

Based on the obtained AEX plots from the HTP batch binding experiments, an evaluation of optimal FT conditions for scale-up verification experiments was performed. For mvAb 2, 4, and 5, the binding on Source 30Q appears distinguishably different to the other two AEX resins. Thus, the contour plots for Source 30Q show a slightly lower total area with an elevated logK_p range (>1, Figure 2, red color), which implies its higher suitability for the FT mode compared with the other two AEX resins for mvAbs 2, 4, and 5. It is worth mentioning that the selected resins have different characteristics including the type of ligand. Hence, Poros 50 HQ ligand is based on quaternary polyethylenimine whereas Q Sepharose FF and Source 30Q are based on quaternary amine as ligands (Information from manufacturers). Interestingly, Source 30Q showed a favorable suitability for FT compared with the other two AEX resins, despite having the same ligand such as Q Sepharose FF. However, other varying characteristics such as bead size/chemistry, ligand density, and porosity may be responsible for the observed differences of mvAb partition. pH 6.0 and NaCl concentrations >50–75 mM favored the distribution of mvAbs into the nonbound fraction for all three tested AEX resins. However, from a process perspective, a higher pH of 7 would be the more common choice since this pH covers a broader range of acidic HCPs (Ichihara et al., 2019). In this case, the required level of NaCl concentration for fractionizing mvAbs 4 and 5 into the nonbound fraction is higher with NaCl concentrations >100 mM that will also reduce binding and clearance of HCPs and potentially also aggregates, DNA, and viruses. For these mvAbs, other chromatographic modes, for example, HIC, can be considered instead of AEX as a polishing step.

Similar to mapping of mvAbs behavior on AEX resins, logK_p surface-response models for the screening of mvAbs 1–6 on MM-resins Capto Adhere and Capto Adhere ImpRes were created as presented in Figure 3. To adjust for the potential stronger binding on these MM resins, a wider range of NaCl concentration (0–500 mM) and pH 5.0–7.0 were screened in the small-scale HTP batch binding experiments. Looking at Figure 3, the categorization of the selected mvAbs into strong and weak binding mvAbs was once more apparent as in Figures 1 and 2. Hence, mvAbs 2, 4, and 5 representing the group of strong binding mvAbs showed under all tested conditions a logK_p that approximates 2 or higher (no color, model unable to predict logK_p out of range). In contrast, mvAbs 1, 3, and 6 showed distributions into nonbound fractions at lower pH (<6.5) and lower NaCl concentration. Here, the lower pH could again favor increased repulsive interactions as previously discussed, whereas the effect of NaCl concentration had an opposite trend on the binding behavior toward MM compared with AEX. This could be due to an increasing salting out of the proteins at elevated NaCl concentrations that promoted the binding toward the hydrophobic part of the MM resin. In case of mvAb 1, 3, and 6, the binding to Capto Adhere was stronger than to Capto Adhere ImpRes, which becomes apparent by a smaller range of lower logK_ps (blue color at the bottom left corner of plots in Figure 3). While ligand chemistry is the same for both MM

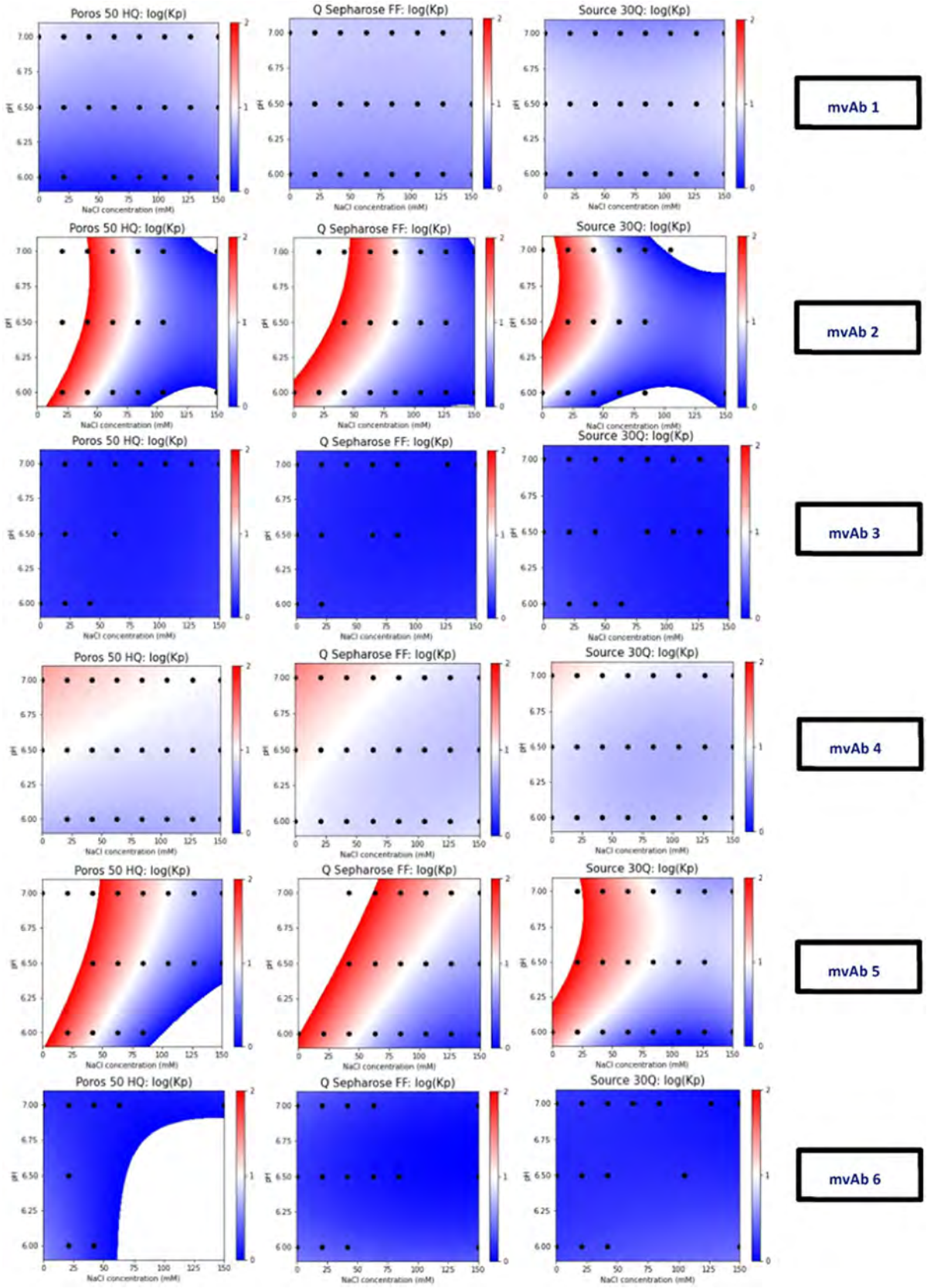

FIGURE 2 Mapping the binding of monovalent mAbs (mvAbs) 1–6 on Poros 50 HQ (left panel), Q Sepharose FF (central panel), and Source 30Q (right panel) at NaCl concentrations ranging from 0 to 150 mM and pH 6.0–7.0. The black dots represent the real data points, whereas noncoloured areas represent logK_p values that were not predictable by the model.

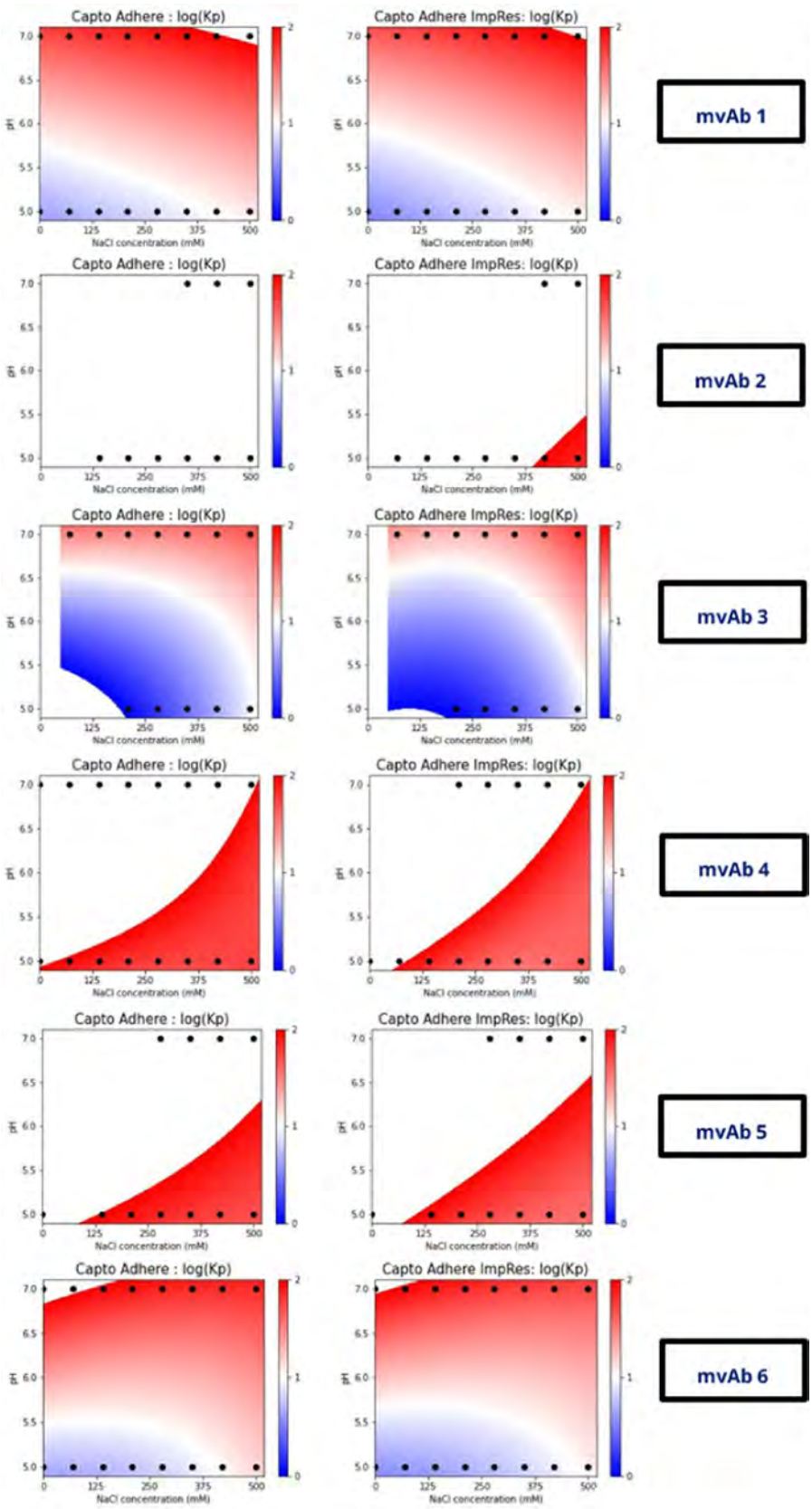

FIGURE 3 Mapping the binding of monovalent mAbs (mvAbs) 1–6 on Capto Adhere (left panel) and Capto Adhere ImpRes (right panel) at NaCl concentrations ranging from 0 to 500 mM and pH 5.0 & 7.0. The black dots represent the real data points. Noncoloured areas represent logK_p values that were out of range.

resins, ligand density is 80–110 µmol/mL resins for Capto Adhere ImpRes and 90–120 µmol/mL for Capto Adhere (information from manufacturer). Thus, the range is shifted toward higher values for Capto Adhere than Capto Adhere ImpRes which could explain the observed differences in log*K*p range. It is noteworthy, that the macropore radius and effective pore diffusivity for several model proteins was shown to be somewhat smaller for Capto Adhere ImpRes than for Capto Adhere (Roberts et al., 2020) that could also potentially effect the kinetics of batch adsorption of mvAb on these two resins.

Selecting Capto Adhere resins for polishing in FT mode, pH 5.0 and NaCl concentrations of 0–210 mM would be most favorable for mvAbs 1, 3, and 6 based on the visual analysis of the contour plots and logK_p data. In this NaCl range, 81%–86% (logK_p 0.59–0.45) and 90%–96% (logK_p 0.28–0.21) of, for example, mvAb 1 were found in nonbound fraction for Capto Adhere and Capto Adhere ImpRes, respectively.

To get insight into the HIC characteristics of the mvAbs, small-scale batch binding experiments were performed on the HIC resins: Capto Phenyl, Phenyl Sepharose FF, and Toyopearl SuperButyl 550-C at NaCl concentrations ranging from 0 to 500 mM and pH 5.0 and 7.0 (similar to HTS setup with MM). The data showed that mvAbs 1–6 fractionized dominantly into the nonbound fraction. This hints toward the complexity of the interaction of MM resins, as it is difficult to predict the binding behavior.

In general, the batch binding format used in this study allowed for reducing the required amount of each mvAb to approx. 10 mg.

3.3 | Protein surface property analyses

Despite similar theoretical pI of 8.02, mvAb 1 and 4 exhibited different binding and FT behaviors in the HTP batch binding experiments (Table 1). To get a deeper insight into these observed differences, in silico protein surface property analyses were carried out on mvAb 1 and 4 representing the weak binding and strong binding groups, respectively, as identified in Figures 1, 2, and 3. Previously, it has been shown that the in silico identification of hydrophobic surface patches can serve as a tool for predicting aggregation propensities (Chennamsetty, Voynov, et al., 2009) and explain chromatographic behavior of Fab fragments on MM resins (Karkov, Krogh, et al., 2015; Karkov, Woo, et al., 2015). Here, we aimed to characterize the surface properties with an easy-to-implement procedure including 2D maps focused on the Fc-region of mvAbs 1 and 4, where the differences in primary sequence were localized. Also in the literature it has been shown that mAbs exhibit preferential orientation of the Fc region toward positively charged surfaces while the Fab part toward negatively charged surfaces as shown by Monte Carlo simulations (Zhou et al., 2004).

Figure 4 shows the identified surface patches on the two mvAbs displayed in 2D view allowing visual assessment of the relative positions of the patches. Comparing the 2D maps, most of the negatively charged patches on mvAb 4 (Figure 4b) are clustered together, whereas the fewer anionic patches on mvAb 1 are highly distributed all over the Fc (Figure 4a). This could explain the stronger retention of mvAb 4 on AEX observed in the experimental data (Figure 2) with the negatively charged clusters creating stronger electrostatic interactions with the AEX resin. In addition, the strong binding of mvAb 4 on Capto Adhere and Capto Adhere ImpRes observed under all experimental conditions could be explained by the proximity of hydrophobic patches close to the negatively charged clusters on mvAb 4 (center of 2D map around patch 2, Figure 4b), potentially creating a strong MM ligand binding site.

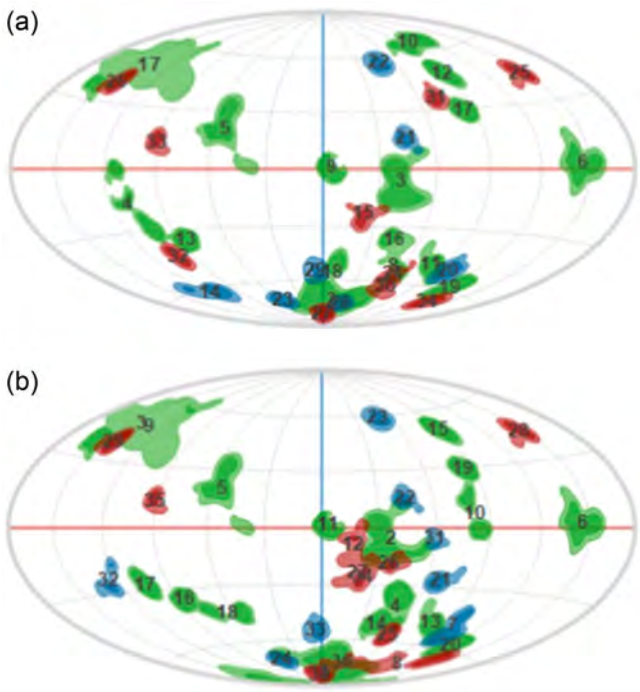

FIGURE 4 Two-dimensional (2D) maps of protein surfaces for monovalent mAbs (mvAb) 1 (a) and 4 (b) with identified patches on the surface. Hydrophobic patches are depicted in green, anionic patches in red, and cationic patches in blue.

3.4 | Verification of HTS data in 1 mL packed columns

The HTP batch binding experiments revealed a significant difference in binding and FT behavior of the tested mvAbs on AEX and MM and addressing Source 30Q as a beneficial AEX resin for FT chromatography in 200 µL scale (Figure 2). The scaled-up 1 mL column experiments aimed at verifying whether observed differences in partition of protein into bound/nonbound fractions with AEX resins could be translated to FT behavior on-column. Therefore, on-column pulse experiments of mvAbs 1 and 4 representing each defined group of weak binding and strong binding, respectively, on 1 mL-packed Poros 50 HQ, Q Sepharose FF, and Source 30Q were performed. Based on Figure 2, 70 mM NaCl and pH 7.0 were selected for the pulse experiments, at which condition differences in logK_p were identifiable for mvAb 1 and 4.

In Table 2, the percentage of recovered mvAbs 1 and 4 in the FT fractions for the pulse experiments conducted on the 1 mL AEX columns Poros 50 HQ, Q Sepharose FF, and Source 30Q are presented. Figure 5 represents the associated chromatograms for the respective chromatographic runs. The FT fraction is defined as the volume captured between the sample application and start of increase in conductivity in the gradient for mvAb 4. For both mvAb 1 and 4, 5 mg/mL resin were loaded in each run.

In Figure 5, the contrast in binding behavior between mvAb 1 and 4 becomes apparent which is consistent with the $\log K_p$ observations made in Figure 2. Thus, mvAb 1 could be entirely recovered in the FT fractions for all three AEX resins at 70 mM NaCl and pH 7.0, which is not the case for mvAb 4, where solely Source 30Q approximates the FT recovery with 95%, whereas Poros 50 HQ and Q Sepharose FF show significantly lower FT recoveries with 20% and 10%, respectively (Table 2) and elution peaks at 9.8–10.1 mS/cm in the gradient. At high protein loads used in process FT conditions, product retention at pH 7.0 and conductivity below 10 mS/cm will result in yield loss as predicted by HTP batch binding data and potentially effecting capacity for HCPs binding.

TABLE 2 Calculated percentage of recovered mvAb 1 and 4 in flowthrough fractions for each resin used in the anion exchange chromatography pulse experiments from peak area with Unicorn 7.4.

	% Flowthrough		
	Poros 50 HQ	Q Sepharose FF	Source 30Q
mvAb 1	>95	>95	>95
mvAb 4	~20	~10	~95

Abbreviation: mvAb, monovalent mAbs.

The weaker binding of mvAb 4 on Source 30Q in comparison to the other two AEX resins seen in the HTP batch binding experiments could be verified in on-column pulse experiments identifying Source 30Q as the most favorable choice of resin for mAb 4 in the AEX resin selection. Also, the higher retention of mvAb 4 to AEX resins first observed in HTS and confirmed here on 1 mL packed column experiments support the hypothesis from the in silico protein surface property analysis, that the cluster of negative charges on the surface of mvAb 4 may cause the higher retention to AEX ligands in contrast to mvAb 1 (Figure 4).

Similar to the pulse experiments conducted on 1 mL AEX resins, pulse experiments of mvAbs 1 and 4 on the MM resins Capto Adhere and Capto Adhere ImpRes were performed to evaluate the predictions made in the HTP batch binding experiments. mvAbs 1 and 4 were selected at 150 mM NaCl and pH 5.0 with a load corresponding to 5 mg/mL resin. The small-scale batch binding experiment predicted a strong binding of mvAb 4 on both MM resins at any condition examined, whereas for mvAb 1 a $\log K_p < 0.5$ on both resins indicating low retention were predicted (Figure 3). Those predicted trends in binding behavior could be confirmed in the on-column pulse experiments presented in Figure 6. Thus, a calculated percentage of mvAb in FT fraction of 100% for mvAb 1 on both Capto Adhere and Capto Adhere ImpRes was determined, whereas 0% was determined for mvAb 4 on both MM resins where the mvAb was solely encountered in the CIP step.

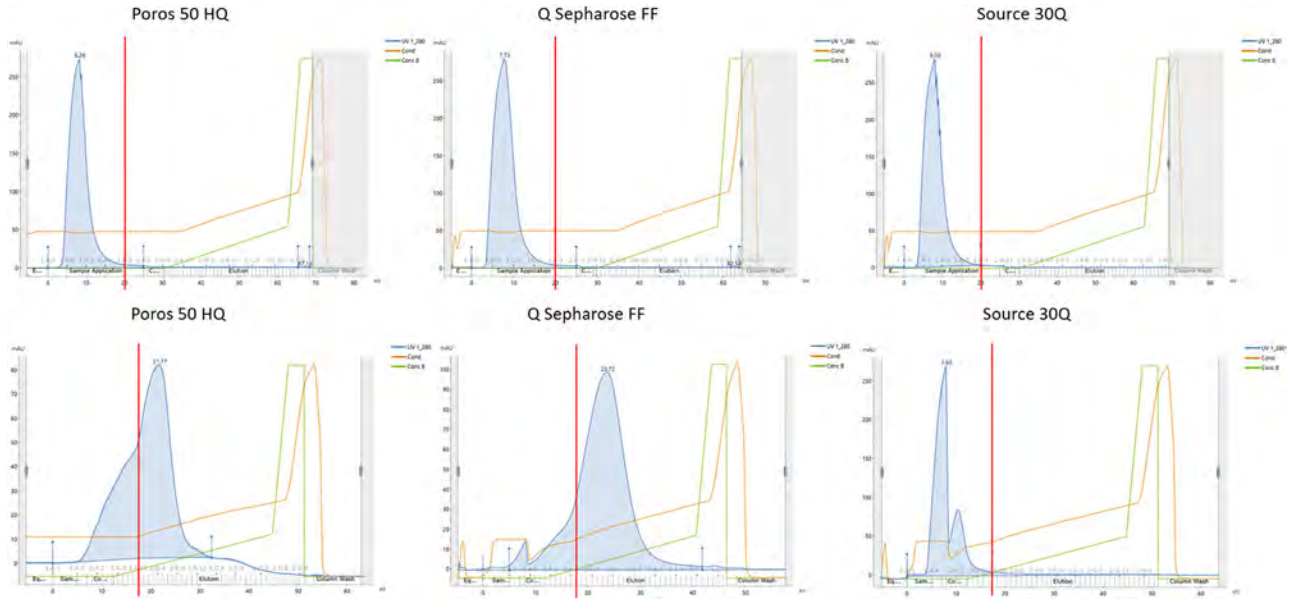

FIGURE 5 Chromatograms for anion exchange chromatography runs performed for monovalent mAbs (mvAb) 1 and 4 (from top to bottom) on different anion exchange chromatography resins (Poros 50 HQ, Q Sepharose FF, Source 30Q, from left to right) at 70 mM NaCl and pH 7.0. The product peaks are depicted in blue. The flowthrough fractions were all collected material until red lines, including sample application and wash. Wash phases for mvAb 1 and mvAb 4 differed and were 10 CV and 5 CV, respectively. X-axis shows volume in mL whereas y-axis represents absorption at 280 nm in mAU (light absorbance in O.D280 mili-arbitrary units).

Altogether, the 1 mL on-column pulse experiments on AEX and MM resins confirmed the predictions made by the HTP batch binding experiments on identifying differences in binding between mvAbs 1 and 4 (theoretical pI = 8.02) and identifying a trend in resin suitability for FT chromatography. This consistency in observed binding underlines the usefulness of robotic liquid handling systems conducting the HTP batch binding experiments. Hence, early process development is accelerated

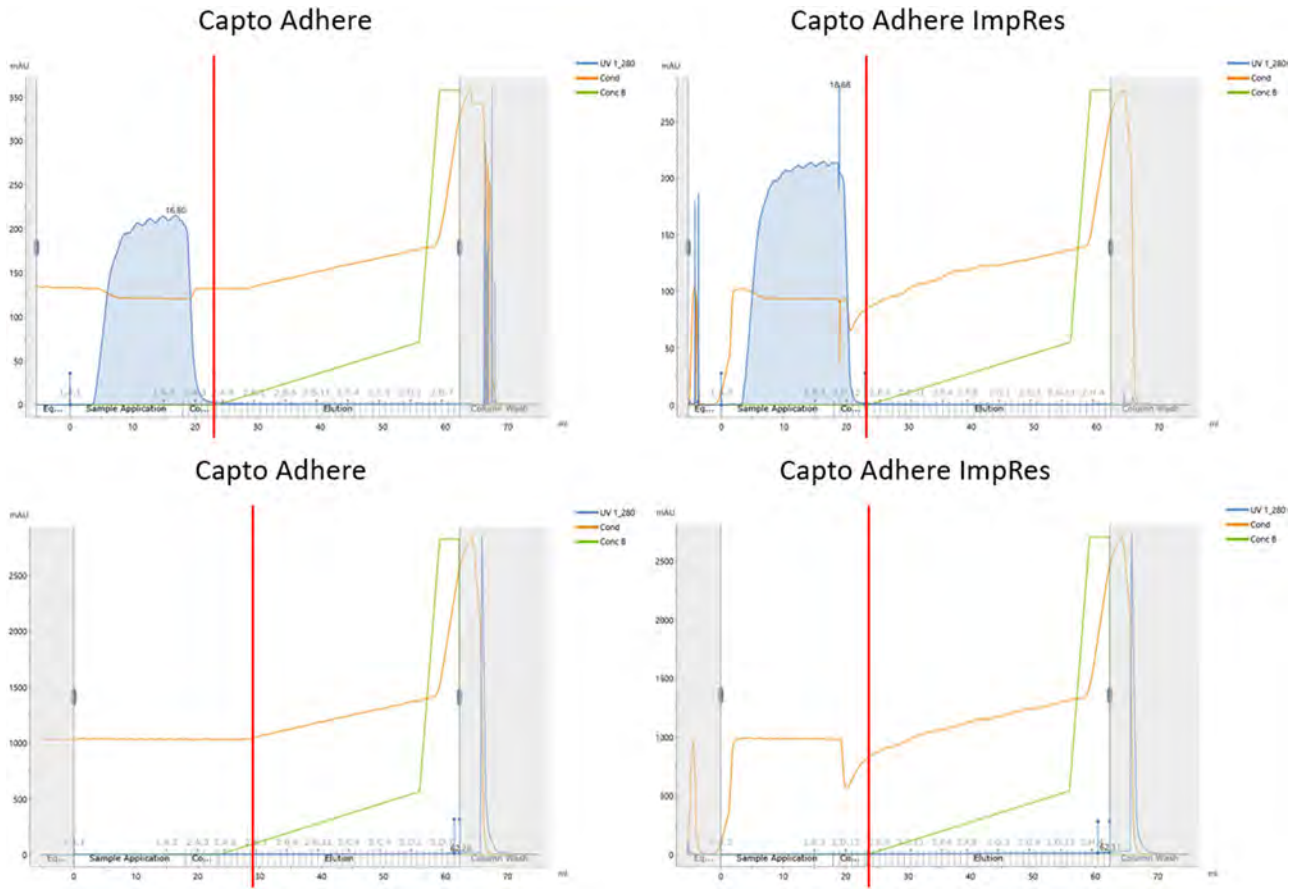

FIGURE 6 Chromatograms for mixed-mode runs performed for monovalent mAbs (mvAb) 1 and 4 (from top to bottom) on Capto Adhere and Capto Adhere ImpRes at 150 mM NaCl and pH 5.0. The flowthrough fractions are marked by red lines. The product peaks are depicted in blue. X-axis shows volume in mL whereas y-axis represents absorption at 280 nm in mAU (light absorbance in O.D280 mili-arbitrary units).

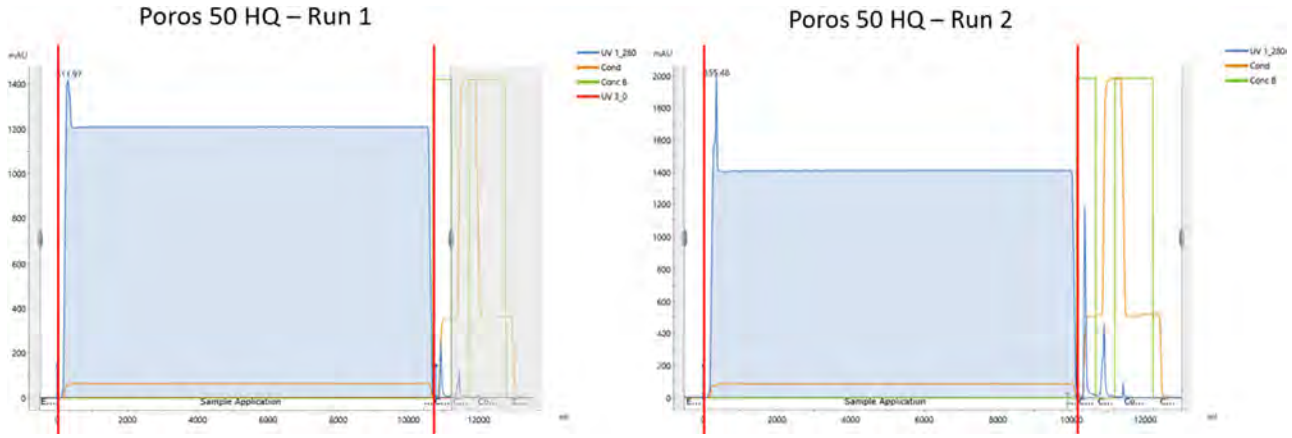

FIGURE 7 Chromatograms for Poros 50 HQ runs 1 and 2 performed for monovalent mAbs (mvAb) 1 (run 1 left, run 2 right) at loading conditions of 75 mM NaCl and pH 7.0. The flowthrough fractions are marked by red lines. The product peaks are depicted in blue. X-axis shows volume in mL whereas y-axis represents absorption at 280 nm in mAU (light absorbance in O.D280 mili-arbitrary units).

considerably by narrowing down the design space for scale-up experiments.

3.5 | Performance of selected FT AEX conditions in mini pilot-scale

The HTS data obtained for mvAb 1 indicate nonbinding (FT) of the mvAb to the AEX resins in all experimental conditions examined (Figure 2, logK_p < 1). While low conductivity range can be advantageous for HCP retention, dilution needed for achieving conductivity below 7 mS/cm in the product pool from the previous CEX purification step is not desirable in the production scale as it would lead to high water consumption, long processing time and low volumetric productivity in both the FT AEX step and the final ultrafiltration/diafiltration (UF/DF) step. Therefore, 7–9 mS/cm and pH 7.0 were selected as the experimental conditions for scale-up purification of mvAb 1 on 259 mL Poros 50 HQ packed columns as shown in Figure 7.

The HTS batch binding experiments of mvAb 1 on Poros 50 HQ showed at selected conditions a weak binding toward the resin with a logK_p 0–0.2 (Figure 2). This trend of weak mvAbs 1 binding is confirmed in the measured percentage of recovered protein in the FT. Thus, >95% of loaded mvAb1 were recovered in the FT fractions of run 1 and 2. Importantly, a reduction of HCPs from 1667–1882 ppm to 71–88 ppm was obtained. HMWP levels in the load were 0.8%–1.0% and within the acceptance limit. Even though the purification in mini-pilot scale was performed with material from a stable cell line expression, the yield predicted in small-scale batch binding experiments that used transient expressed material translated well.

4 | CONCLUSION

In this study, HTS in FT mode in AEX and MM chromatographic systems exceled as a useful tool for accelerating DSP development. HTS batch binding experiments facilitated a rapid identification of differences in the binding behavior of six homologous mvAbs and trends in resin suitability that served as accurate predictors for mvAb behavior in on-column pulse (1 mL) and scale-up mini-pilot (259 mL) experiments. Surprisingly, despite maintaining an experimental pH well below the theoretical pI for the mvAbs, half of the investigated mvAbs displayed binding characteristics instead of FT which could be explained by the in silico protein surface analyses. Our results could promote the economical usefulness of integrating HTS in DSP development, that could significantly decrease required resources in terms of time and raw materials.

The presented study could be extended by including more resins or different mAb modalities to further explore the applicability of HTS in DSP development. Furthermore, the evaluation of HTS for predicting separation of mvAbs from different impurities could be performed. The molecular interactions of mvAbs and respective ligands could be simulated in silico to deepen the insight into the observed complexity of mvAb binding. Finally, the batch binding data could be combined with mechanistic modeling tools such as developed for FT chromatography (Hess et al., 2023) to enable the on-column verification experiments to be substituted by simulations which could provide even faster predictions of large-scale FT processes.

AUTHOR CONTRIBUTIONS

Julius Klemens Lorek performed the study, did drafting, and wrote most parts of the paper. Hanne Sophie Karkov did Structural (surface-property) modeling, wrote part of the paper. Finn Matthiesen did LogKp Surface-Response Modeling. Maria Dainiak designed the study, wrote part of the paper.

ACKNOWLEDGMENTS

The authors acknowledge the assistance of Vibeke Rode and Mie Mandal Mortensen for laboratory support and Thomas Egebjerg for protein expression and Anette Henriksen for creating the homology models. This study was funded by Novo Nordisk A/S.

CONFLICT OF INTEREST STATEMENT

The authors declare no conflict of interest.

DATA AVAILABILITY STATEMENT

The data that support the findings of this study are available from the corresponding author upon reasonable request.

ORCID

Julius Klemens Lorek http://orcid.org/0000-0001-9387-9461
Maria Dainiak http://orcid.org/0000-0001-6851-7207

REFERENCES

Baran, K., Zimoch, P., Stańczak, A., Piątkowski, W., & Antos, D. (2021). Separation of charge variants of a monoclonal antibody by overloaded ion exchange chromatography. *Journal of Chromatography A*, *1658*, 462607.

Bensch, M., Schulze Wierling, P., von Lieres, E., & Hubbuch, J. (2005). High throughput screening of chromatographic phases for rapid process development. *Chemical Engineering\& Technology: Industrial Chemistry-Plant Equipment-Process Engineering-Biotechnology*, *28*(11), 1274–1284.

Bergander, T., Nilsson-Valimaa, K., Oberg, K., & Lacki, K. M. (2008). High-throughput process development: Determination of dynamic binding capacity using microtiter filter plates filled with chromatography resin. *Biotechnology Progress*, *24*(3), 632–639.

Brown, M. R., Burnham, M. S., Lute, S. C., Johnson, S. A., Walsh, A. A., Brorson, K. A., & Roush, D. J. (2018). Defining the mechanistic binding of viral particles to a multi-modal anion exchange resin. *Biotechnology Progress*, *34*(4), 1019–1026.

Chahar, D. S., Ravindran, S., & Pisal, S. S. (2020). Monoclonal antibody purification and its progression to commercial scale. *Biologicals*, *63*, 1–13.

Charlton, H. (2006). Chromatography process development using 96-well microplate formates. *BioPharm. International*, *19*, 20–26+.

Chen, S. W., Hoi, K. M., Mahfut, F. B., Yang, Y., & Zhang, W. (2022). Effective flow-through polishing strategies for knob-into-hole bispecific antibodies. *Bioresources and Bioprocessing*, *9*(1), 98.

Chennamsetty, N., Helk, B., Voynov, V., Kayser, V., & Trout, B. L. (2009). Aggregation-prone motifs in human immunoglobulin G. *Journal of Molecular Biology*, *391*(2), 404–413.

Chennamsetty, N., Voynov, V., Kayser, V., Helk, B., & Trout, B. L. (2009). Design of therapeutic proteins with enhanced stability. *Proceedings of the National Academy of Sciences*, *106*(29), 11937–11942.

Coffman, J. L., Kramarczyk, J. F., & Kelley, B. D. (2008). High-throughput screening of chromatographic separations: I. Method development and column modeling. *Biotechnology and Bioengineering*, *100*(4), 605–618.

Cooney, C. L., & Konstantinov, K. B. (2015). White paper on continuous bioprocessing. *Journal of Pharmaceutical Sciences*, *104*, 813–820.

Cramer, S., Rege, K., Dordick, J., & Tugcu, N. (2005). *High throughput screening of potential displacer molecules* (Patent No. US20050176937A1). Google Patents.

Dainiak, M. B., Galaev, I. Y., & Mattiasson, B. (2006). Affinity cryogel monoliths for screening for optimal separation conditions and chromatographic separation of cells. *Journal of Chromatography A*, *1123*(2), 145–150.

Feidl, F., Vogg, S., Wolf, M., Podobnik, M., Ruggeri, C., Ulmer, N., Wälchli, R., Souquet, J., Broly, H., Butté, A., & Morbidelli, M. (2020). Process-wide control and automation of an integrated continuous manufacturing platform for antibodies. *Biotechnology and Bioengineering*, *117*(5), 1367–1380.

Ghose, S., Tao, Y., Conley, L., & Cecchini, D. (2013). Purification of monoclonal antibodies by hydrophobic interaction chromatography under no-salt conditions. *mAbs*, *5*(5), 795–800.

Gronemeyer, P., Ditz, R., & Strube, J. (2014). Trends in upstream and downstream process development for antibody manufacturing. *Bioengineering*, *1*(4), 188–212.

Hanora, A., Bernaudat, F., Plieva, F. M., Dainiak, M. B., Bülow, L., Galaev, I. Y., & Mattiasson, B. (2005). Screening of peptide affinity tags using immobilised metal affinity chromatography in 96-well plate format. *Journal of Chromatography A*, *1087*(1–2), 38–44.

Hess, R., Yun, D., Saleh, D., Briskot, T., Grosch, J.-H., Wang, G., Schwab, T., & Hubbuch, J. (2023). Standardized method for mechanistic modeling of multimodal anion exchange chromatography in flow through operation. *Journal of Chromatography A*, *1690*, 463789.

Hummel, J., Pagkaliwangan, M., Gjoka, X., Davidovits, T., Stock, R., Ransohoff, T., Gantier, R., & Schofield, M. (2019). Modeling the downstream processing of monoclonal antibodies reveals cost advantages for continuous methods for a broad range of manufacturing scales. *Biotechnology Journal*, *14*(2), 1700665.

Ichihara, T., Ito, T., & Gillespie, C. (2019). *Polishing approach with fully connected flow-through purification for therapeutic monoclonal antibody. Engineering in Life Sciences*, *19*, 31–36.

Ichihara, T., Ito, T., Kurisu, Y., Galipeau, K., & Gillespie, C. (2018). Integrated flow-through purification for therapeutic monoclonal antibodies processing. *mAbs*, *10*(2), 325–334.

Igawa, T., Haraya, K., & Hattori, K. (2016). Sweeping antibody as a novel therapeutic antibody modality capable of eliminating soluble antigens from circulation. *Immunological Reviews*, *270*(1), 132–151.

Karkov, H. S., Krogh, B. O., Woo, J., Parimal, S., Ahmadian, H., & Cramer, S. M. (2015). Investigation of protein selectivity in multimodal chromatography using in silico designed Fab fragment variants. *Biotechnology and Bioengineering*, *112*(11), 2305–2315.

Karkov, H. S., Woo, J., Krogh, B. O., Ahmadian, H., & Cramer, S. M. (2015). Evaluation of selectivity in homologous multimodal chromatographic systems using in silico designed antibody fragment libraries. *Journal of Chromatography A*, *1426*, 102–109.

Kelley, B. D., Switzer, M., Bastek, P., Kramarczyk, J. F., Molnar, K., Yu, T., & Coffman, J. (2008). High-throughput screening of chromatographic separations: IV. ion-exchange. *Biotechnology and Bioengineering*, *100*(5), 950–963.

Khanal, O., & Lenhoff, A. M. (2021). Developments and opportunities in continuous biopharmaceutical manufacturing. *mAbs*, *13*(1), 1903664.

Kittelmann, J., Ottens, M., & Hubbuch, J. (2015). Robust high-throughput batch screening method in 384-well format with optical in-line resin quantification. *Journal of Chromatography B*, *988*, 98–105.

Kramarczyk, J. F., Kelley, B. D., & Coffman, J. L. (2008). High-throughput screening of chromatographic separations: II. Hydrophobic interaction. *Biotechnology and Bioengineering*, *100*(4), 707–720.

Liu, H. F., Ma, J., Winter, C., & Bayer, R. (2010). Recovery and purification process development for monoclonal antibody production. *mAbs*, *2*(5), 480–499.

Liu, J., Yang, T., Ladiwala, A., Cramer, S. M., & Breneman, C. M. (2006). High throughput determination and QSER modeling of displacer DC-50 values for ion exchange systems. *Separation Science and Technology*, *41*(14), 3079–3107.

McDonald, P., Tran, B., Williams, C. R., Wong, M., Zhao, T., Kelley, B. D., & Lester, P. (2016). The rapid identification of elution conditions for therapeutic antibodies from cation-exchange chromatography resins using high-throughput screening. *Journal of Chromatography A*, *1433*, 66–74.

Merchant, M., Ma, X., Maun, H. R., Zheng, Z., Peng, J., Romero, M., Huang, A., Yang, N., Nishimura, M., Greve, J., Santell, L., Zhang, Y. W., Su, Y., Kaufman, D. W., Billeci, K. L., Mai, E., Moffat, B., Lim, A., Duenas, E. T., … Yansura, D. G. (2013). Monovalent antibody design and mechanism of action of onartuzumab, a MET antagonist with anti-tumor activity as a therapeutic agent. *Proceedings of the National Academy of Sciences*, *110*(32), E2987–E2996.

Nfor, B. K., Noverraz, M., Chilamkurthi, S., Verhaert, P. D. E. M., van der Wielen, L. A. M., & Ottens, M. (2010). High-throughput isotherm determination and thermodynamic modeling of protein adsorption on mixed mode adsorbents. *Journal of Chromatography A*, *1217*(44), 6829–6850.

Noh, H., Yohe, S. T., & Vogler, E. A. (2008). Volumetric interpretation of protein adsorption: Ion-exchange adsorbent capacity, protein pI, and interaction energetics. *Biomaterials*, *29*(13), 2033–2048.

Petroff, M. G., Bao, H., Welsh, J. P., van Beuningen – de Vaan, M., Pollard, J. M., Roush, D. J., Kandula, S., Machielsen, P., Tugcu, N., & Linden, T. O. (2016). High throughput chromatography strategies for potential use in the formal process characterization of a monoclonal antibody. *Biotechnology and Bioengineering*, *113*(6), 1273–1283.

Rathore, A. S., Agarwal, H., Sharma, A. K., Pathak, M., & Muthukumar, S. (2015). Continuous processing for production of biopharmaceuticals. *Preparative Biochemistry and Biotechnology*, *45*(8), 836–849.

Rege, K., Ladiwala, A., & Cramer, S. M. (2005). Multidimensional high-throughput screening of displacers. *Analytical Chemistry*, *77*(21), 6818–6827.

Roberts, J. A., Kimerer, L., & Carta, G. (2020). Effects of molecule size and resin structure on protein adsorption on multimodal anion exchange chromatography media. *Journal of Chromatography A*, *1628*, 461444.

Robinson, J., Roush, D., & Cramer, S. (2018). Domain contributions to antibody retention in multimodal chromatography systems. *Journal of Chromatography A*, *1563*, 89–98.

Robinson, J., Roush, D., & Cramer, S. M. (2020). The effect of pH on antibody retention in multimodal cation exchange chromatographic systems. *Journal of Chromatography A*, *1617*, 460838.

Robinson, J. R., Karkov, H. S., Woo, J. A., Krogh, B. O., & Cramer, S. M. (2017). QSAR models for prediction of chromatographic behavior of homologous Fab variants. *Biotechnology and Bioengineering*, *114*(6), 1231–1240.

Roush, D. J., Gill, D. S., & Willson, R. C. (1994). Electrostatic potentials and electrostatic interaction energies of rat cytochrome b5 and a

simulated anion-exchange adsorbent surface. *Biophysical Journal*, *66*(5), 1290–1300.

Sakhnini, L. I., Pedersen, A. K., León, I. R., Greisen, P. J., Hansen, J. J., Vester-Christensen, M. B., Bülow, L., & Dainiak, M. B. (2019). Optimizing selectivity of anion hydrophobic multimodal chromatography for purification of a single-chain variable fragment. *Engineering in Life Sciences*, *19*(7), 490–501.

Saleh, D., Hess, R., Ahlers-Hesse, M., Beckert, N., Schönberger, M., Rischawy, F., Wang, G., Bauer, J., Blech, M., Kluters, S., Studts, J., & Hubbuch, J. (2021). Modeling the impact of amino acid substitution in a monoclonal antibody on cation exchange chromatography. *Biotechnology and Bioengineering*, *118*(8), 2923–2933.

Saleh, D., Hess, R., Ahlers-Hesse, M., Rischawy, F., Wang, G., Grosch, J.-H., Schwab, T., Kluters, S., Studts, J., & Hubbuch, J. (2023). A multiscale modeling method for therapeutic antibodies in ion exchange chromatography. *Biotechnology and Bioengineering*, *120*(1), 125–138.

Shukla, A. A., Hubbard, B., Tressel, T., Guhan, S., & Low, D. (2007). Downstream processing of monoclonal antibodies—application of platform approaches. *Journal of Chromatography B*, *848*(1), 28–39.

Silva, T. C., Eppink, M., & Ottens, M. (2022). Automation and miniaturization: Enabling tools for fast, high-throughput process development in integrated continuous biomanufacturing. *Journal of Chemical Technology\& Biotechnology*, *97*(9), 2365–2375.

Spiess, C., Zhai, Q., & Carter, P. J. (2015). Alternative molecular formats and therapeutic applications for bispecific antibodies. *Molecular Immunology*, *67*(2), 95–106.

Stein, A., & Kiesewetter, A. (2007). Cation exchange chromatography in antibody purification: pH screening for optimised binding and HCP removal. *Journal of Chromatography B*, *848*(1), 151–158.

Teshima, G., Li, M.-X., Danishmand, R., Obi, C., To, R., Huang, C., Kung, J., Lahidji, V., Freeberg, J., Thorner, L., & Tomic, M. (2011). Separation of oxidized variants of a monoclonal antibody by anion-exchange. *Journal of Chromatography A*, *1218*(15), 2091–2097.

Thiemann, J., Jankowski, J., Rykl, J., Kurzawski, S., Pohl, T., Wittmann-Liebold, B., & Schlüter, H. (2004). Principle and applications of the protein-purification-parameter screening system. *Journal of Chromatography A*, *1043*(1), 73–80.

Wensel, D. L., Kelley, B. D., & Coffman, J. L. (2008). High-throughput screening of chromatographic separations: III. Monoclonal antibodies on ceramic hydroxyapatite. *Biotechnology and Bioengineering*, *100*(5), 839–854.

Wiendahl, M., Schulze Wierling, P., Nielsen, J., Fomsgaard Christensen, D., Krarup, J., Staby, A., & Hubbuch, J. (2008). High throughput screening for the design and optimization of chromatographic processes--miniaturization, automation and parallelization of breakthrough and elution studies. *Chemical Engineering\& Technology: Industrial Chemistry-Plant Equipment-Process Engineering-Biotechnology*, *31*(6), 893–903.

Wierling, P. S., Bogumil, R., Knieps-Grünhagen, E., & Hubbuch, J. (2007). High-throughput screening of packed-bed chromatography coupled with SELDI-TOF MS analysis: Monoclonal antibodies versus host cell protein. *Biotechnology and Bioengineering*, *98*(2), 440–450.

Zhou, J., Tsao, H.-K., Sheng, Y.-J., & Jiang, S. (2004). Monte Carlo simulations of antibody adsorption and orientation on charged surfaces. *The Journal of Chemical Physics*, *121*(2), 1050–1057.

RESEARCH ARTICLE

ADVANCED THERAPEUTICS
www.advtherap.com

An Adaptable Antibody-Based Platform for Flexible Synthetic Peptide Delivery Built on Agonistic CD40 Antibodies

Mohamed Eltahir, Ida Laurén, Martin Lord, Aikaterini Chourlia, Leif Dahllund, Anders Olsson, Aljona Saleh, A. Jimmy Ytterberg, Annika Lindqvist, Oskar Andersson, Helena Persson, and Sara M. Mangsbo**

The agonistic potentials of therapeutic anti-CD40 antibodies have been profiled in relation to antibody isotype and epitope specificity. Still, clinical impact relies on a well-balanced clinical efficacy versus target-mediated toxicity. As CD40-mediated immune activation must rely on a combination of stimulation of antigen-presenting cells (APCs) alongside antigen presentation, for efficient T cell priming, alternative approaches to improve the therapeutic outcome of CD40-targeting strategies should focus on providing optimal antigen presentation together with CD40 stimulation. Herein, a bispecific antibody targeting CD40 as a means to deliver cargo (i.e., synthetic peptides) into APCs through a non-covalent, high-affinity interaction between the antibody and the cargo peptide, further referred to as the Adaptable Drug Affinity Conjugate (ADAC) technology, has been developed. The ADAC platform demonstrated a target-specific $CD4^+$ and $CD8^+$ T cell expansion in vitro and significantly improved peptide-specific $CD8^+$ T cell proliferation in vivo. In addition, the strategy dramatically improved the in vitro and in vivo half-life of the synthetic peptides. Future applications of ADAC involve pandemic preparedness to viral genetic drift as well as neoepitope vaccination strategies where the bispecific antibody is an off-the-shelf product, and the peptide antigen is synthesized based on next-generation sequencing data mining.

1. Introduction

Antigen delivery in the form of synthetic peptide-based vaccines has commonly been performed using lipid or nanoparticle-based technologies with and without the addition of adjuvants.[1,2] Depot delivery of peptide-based drugs using these formulations can prevent rapid degradation and drug clearance, but trimmed peptides (HLA-matched epitopes) delivered in a lipid-based formulation have also been reported to trap expanded antigen-specific cells.[3] Vector-based antigen delivery can lead to antigen competition of potent viral epitopes, thereby hampering anti-tumor responses, which may be tackled using a shift in vector between the prime and the boost delivery time-point.[4] Antibody-based delivery platforms can be utilized by conjugating proteins or peptides, forming antibody-drug conjugates where the antigen is the cargo. This approach has been studied using several dendritic cell (DC) protein targets such as c-type lectins (e.g., DEC-205, Dectin-1, CD207, LOX-1, and others) and non-lectins like mannose receptors, integrins, and CD40.[5]

However, not all targets and antibodies facilitate both activation of the DC along with enabling antigen uptake. Furthermore, it is important that the receptor-mediated internalization should not lead to a loss of antigen on the surface, but rather a recycling of the targeted antigen, and possibly an increased expression over time as activation takes place. Targeting the CD40 receptor on DCs for antigen delivery via coupling of the antigen to an

M. Eltahir, I. Laurén, M. Lord, A. Chourlia, S. M. Mangsbo
Department of Pharmacy
Science for Life Laboratory
Uppsala University
Husargatan 3, Uppsala Box 580 751 24, Sweden
E-mail: mohamed.eltahir@igp.uu.se; sara.mangsbo@farmaci.uu.se

The ORCID identification number(s) for the author(s) of this article can be found under https://doi.org/10.1002/adtp.202200008

DOI: 10.1002/adtp.202200008

L. Dahllund, A. Olsson, O. Andersson, H. Persson
SciLifeLab Drug Discovery and Development
Science for Life Laboratory – Stockholm
Tomtebodavägen 23A, Solna 171 65, Sweden

L. Dahllund, A. Olsson, O. Andersson, H. Persson
School of Engineering Sciences in Chemistry
Biotechnology and Health
Royal Institute of Technology (KTH)
Tomtebodavägen 23A, Solna 65, Sweden

A. Saleh, A. J. Ytterberg, A. Lindqvist
Department of Pharmacy
SciLifeLab Drug Discovery and Development Platform
Uppsala University
Husargatan 3, Uppsala Box 580 751 24, Sweden

anti-CD40 antibody has been shown to elicit superior $CD8^+$ cross-priming and a CD8-specific immune memory response.[5–8] Besides this, the use of anti-CD40 antibody conjugates also results in the achievement of robust adjuvant response at a lower dose, which is vital in limiting the toxic effects of systemic anti-CD40 therapy.[6]

Each tumor is unique, and there is a growing interest in neoantigen vaccination. However, individualized peptide-based vaccines are challenging to produce, formulate, and deliver.[9] Herein we have built a protein-based platform, in the form of a bispecific tetravalent antibody, for optimized targeting, activation of DCs and improved antigen uptake. The platform uses an affinity-based approach, further named the Adaptable Drug Affinity Conjugate (ADAC) technology, where the cargo peptide antigen is non-covalently linked to an agonistic anti-CD40 antibody. The high-affinity interaction, accomplished via a second binding domain through a peptide-Tag (pTag), ensures the binding of the cargo antigen to the antibody and its release within the cell.

Several strategies have been investigated to deliver the agonistic CD40 signal to the DCs where the tumor antigens are present to ensure the appropriate adjuvant effect of agonistic anti-CD40 antibodies. These include administering anti-CD40 antibodies intratumorally, where tumor antigen shedding ensures antigen and antibody lymph node drainage, leading to antigen presentation and immune stimulation at the same site.[10–12] Besides posing superior efficiency over systemic administration, this approach reduces adverse effects.[12] However, it may lead to the expansion of tumor-associated myeloid-derived suppressor cells.[13] Another approach involves the covalent coupling of the tumor antigen to an anti-CD40 antibody. This conjugation approach has been tested experimentally with several antigens, including herpes simplex glycoprotein,[6] an influenza peptide split virus or whole virus vaccines,[7] and with the A20 lymphoma idiotype.[8] This approach has shown better immunogenicity and superior efficiency at a lower dose of vaccination than non-linked antigen material mixed with the antibody.

However, conjugating the tumor antigens to the anti-CD40 antibody is a laborious and challenging process, and the final product is rigid and unadaptable due to the nature of the chemical conjugation. ADAC is a flexible platform for antigen-adjuvant delivery to the relevant antigen-presenting cells (APCs) through CD40. This approach enables the antibody development as an adjuvant product, whereas the peptide synthesis and release through regulatory process approval is a separate entity rather than a specific drug market approval. By avoiding the need for complex chemical conjugation, the ADAC platform provides a versatile approach for varying the tumor antigen, thereby facilitating the personalization of cancer patient therapy and offering a feasible way to manage vaccine adaptation with viral genetic drift in a pandemic situation.

2. Experimental Section

2.1. In Vitro and In Vivo Materials and Reagents

B3Z, pmel-1, or OT-II cells were used for the T cell proliferation and activation assays. B3Z is a T cell hybridoma expression T cell receptor (TCR) that recognizes MHC-I loaded with $OVA_{257-264}$ albumin peptide (SIINFEKL). B3Z cells express β-galactosidase under the interleukin (IL)-2 promoter, converting chlorophenol Red-β-D-galactopyranoside (CPRG) substrate and enabling detection of B3Z activation via absorbance readout.[14] The pmel-1 transgenic strain expresses the TCR specific for MHC-I/$hgp100_{25-33}$ (KVPRNQDWL).[15] The OT-II transgenic strain consists of T cells expressing the TCR specific for the MHC-II/peptide $OVA_{323-339}$ (ISQAVHAAHAEINEAGR).[16] $CD8^+$ T cells from pmel-1 or $CD4^+$ T cells from OT-II splenocytes were isolated by harvesting spleens and inguinal lymph nodes from adult B6. Cg-Thy1a/Cy Tg (TcraTcrb)8Rest/J transgenic mice (pmel-1 mice) or C57BL/6-Tg-(TcraTcrb)425Cbn/Crl transgenic mice, (OT-II mice), respectively (The Jackson Laboratory). The organs were carefully mashed and passed through 70 µm cell strainers to achieve single-cell suspensions, and red blood cells were lysed using RBC lysis buffer (eBioscience). For in vitro experiments, pmel-1 $CD8^+$ cytotoxic T cells were isolated using Dynabeads Untouched Mouse CD8 Cells Kit, and the OT-II $CD4^+$ helper T cells were isolated using Dynabeads Untouched Mouse CD4 Cells Kit (both from Invitrogen). Long bones from transgenic human CD40 mice were kindly provided by Dr. Peter Ellmark (Alligator Biosciences, Lund, Sweden). Bone marrow progenitor cells were isolated from the long bones and differentiated to bone marrow-derived dendritic cells (BMDC) (described below). For in vivo experiments, pmel-1 and OT-II mice (The Jackson Laboratory) were bred and housed in the Uppsala Biomedical Center's (BMC) animal facility. For in vivo experiments, all animals were between 8–15 weeks of age at the time of the experiment. Both female and male mice were used in the in vivo experiments. For a given single experiment, one gender, female or male mice, we used.

2.2. Antibody Constructs

The tetravalent bispecific antibodies used in these studies are composed of an anti-CD40 monoclonal antibody and a tag moiety binding part. The two anti-CD40 antibodies used were CP-870.893 or 1150/1151 (further on named 1150), described in WO 2015/09 1853. Genes encoding the variable parts of the heavy chain, VH, and light chain, VL, were kindly provided by Dr. Peter Ellmark (Alligator Biosciences, Lund, Sweden). The VH and VL regions were PCR amplified and inserted into modified versions of the pIgG vector (GenBank: MK988448.1), using the In-Fusion HD Plus Cloning Kit (Clontech, #638 909). Two antibodies of each clone were constructed, differing in IgG subclass, IgG1 or IgG2. CP-870893 of the IgG1 and IgG2 subclasses were named CP-1 and CP-2, respectively. Analogously, the two subclass variants of the 1150 antibody were denoted 1150–1 and 1150–2 (**Table 1**). Based on these parental constructs, tetravalent bispecific antibodies, named Bispecific/Tagged-peptide antibody (BiTag), were constructed through fusion with one of two different anti-Tag single-chain variable fragments (scFv); 14GIIICII or FITC8. 14GIIICII originates in a mouse IgG1 antibody, previously generated by immunization of mice with a linear B-cell epitope of tetanus toxin (amino acid sequence FIGITELKKLESKINKVF).[17] Hybridoma sequencing, outsourced to Absolute Antibody (Redcar, United Kingdom), was performed by proprietary next-generation sequencing (NGS)-based technology. The VH and VL

Table 1. List of parental and BiTag antibodies used in the different in vitro and in vivo models.

Antibody	Isotype of anti-CD40	Anti-CD40 antibody	scFv	Location of scFv	Bispecific
Bi1-CP	h-IgG1	CP-870.893	Anti-pTag	CH3	Yes
Bi2-CP	h-IgG2	CP-870.893	Anti-pTag	CH3	Yes
Bi3-CP	h-IgG1	CP-870.893	Anti-pTag	CL	Yes
Bi9-1150	h-IgG1	1150	Anti-pTag	CH3	Yes
Bi10-1150	h-IgG2	1150	Anti-pTag	CH3	Yes
Bi11-1150	h-IgG1	1150	Anti-pTag	CL	Yes
Bi17-CP	h-IgG2	CP-870.893	Anti-fTag	CH3	Yes
CP-1	h-IgG1	CP-870.893	–	–	No
CP-2	h-IgG2	CP-870.893	–	–	No
1150-1	h-IgG1	1150	–	–	No
1150-2	h-IgG2	1150	–	–	No

regions were successfully assembled and sequenced, and based on these, a gene encoding an scFv was formed by fusing the VH to the VL, N-terminal to C-terminal, via a glycine-serine linker ((Gly4Ser)4). Protein expression and subsequent surface plasmon resonance (SPR) experiments suggested that the scFv fully retained the antigen-binding ability of its full-length parental IgG counterpart (data not shown). PCR amplification and In-Fusion cloning was subsequently used to fuse the 14GIIICII scFv gene to the four anti-CD40 vector constructs, either to the C-terminal end of a heavy (CH3) or light chain (CL) through a (Gly4Ser)2 linker. Altogether, this procedure gave rise to six BiTag constructs. An overview of these is shown in Table 1, and a schematic representation is depicted in **Figure 1**. The final expression vectors were transformed into Escherichia coli cells and plasmid DNA isolated, and their intended designs were confirmed by DNA sequencing. In addition, a seventh BiTag antibody was constructed, named Bi17-CP. This BiTag is composed of the human anti-fluorescein scFv FITC8 (GeneBank, accession number AX814386.1) fused to the CH3 of CP-2 (Table 1). FITC8 was generated by phage display and bind fluorescein (in the context of this work, denoted fluorescent Tag [fTag]) with an affinity of ≈0.9 nM.[18] Cloning of this construct was outsourced to Absolute Antibody, using the same linker regions as described above.

2.3. Antibody Expression, Purification, and Biophysical Analyses

Parental and BiTag antibodies were expressed by transient transfection of human embryonic kidney cells in suspension. Transfection of plasmid DNA into ExpiHEK293FTM cells (ThermoFisher, #A14527) was performed using an ExpiFectamine 293 Transfection Kit (ThermoFisher, #A14525). After six days of cultivation at 37 °C, 8% CO2, 70% rH, and 125 rpm, the media supernatants were purified in two steps by affinity chromatography using a HiTrap Protein A HP column (Cytiva) and HiLoad 16/600 Superdex 200 size exclusion chromatography (SEC) (Cytiva) on an ÄKTA purifier system. The size exclusion pools were concentrated to a volume of ≈1 mL or a concentration of at least 1 mg mL^{-1} by Pierce Protein Concentrators (PES, 5–20 mL) with a molecular cut-off of 30 kDa (Thermo Scientific, #88 531). The

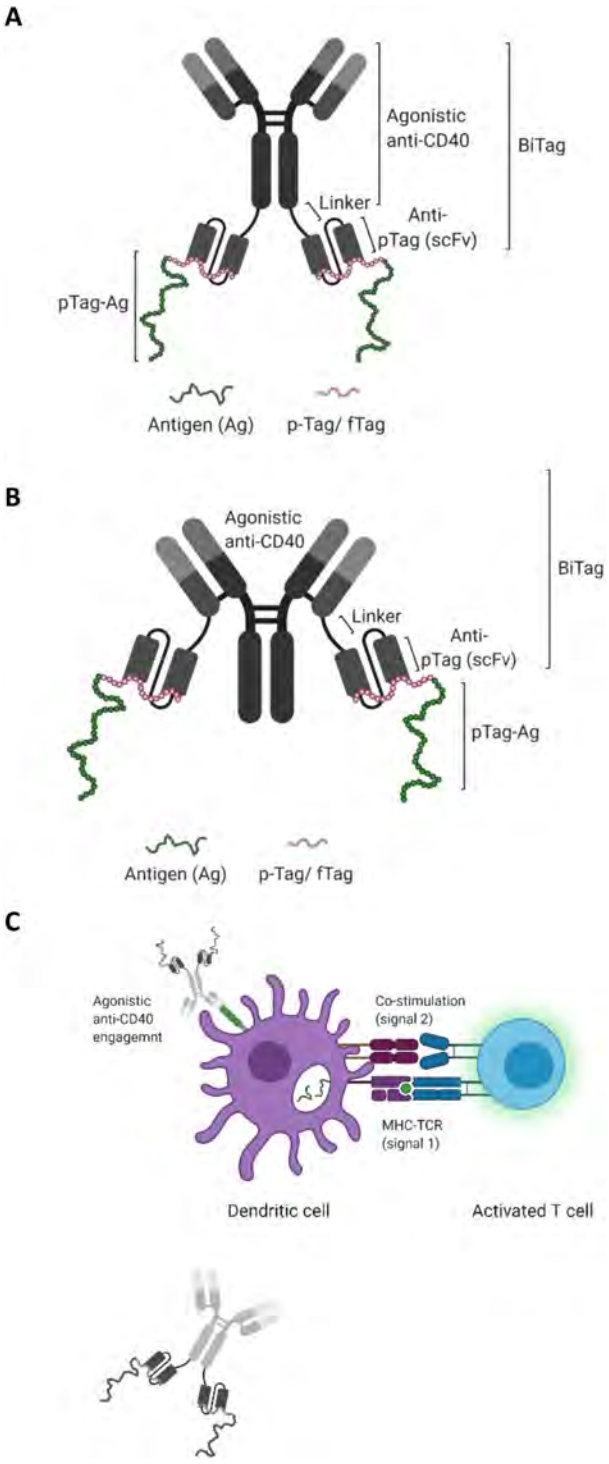

Figure 1. Illustration of the ADAC platform and target binding. Schematic representation of the design of the BiTag. A tetravalent bispecific antibody consists of an agonistic anti-CD40 hIgG1 or hIgG2 antibody covalently linked to two identical scFv targeting a linear pTag on the C-terminal of A) CH3 or B) CL. The peptide antigen is a synthetic long peptide with a constant pTag or fTag and a variable tumor antigen (Ag). C) The BiTag platform enables simultaneous delivery of antigen (signal 1) and co-stimulation to the T cells (signal 2), resulting in robust T cell activation. Illustrations are created with BioRender.com.

Table 2. List of peptide antigens (pTag-Ag) used for the different in vitro and in vivo models. Underlined: pTag sequence, Bold: T cell epitope (Ag).

Peptide	Peptide identity	Sequence
UU05	**pTag-SIINFEKL (long)**	FIGITELKKLESKINKVFLEQLE**SIINFEKL**AAAAAK
UU10	SIINFEKL (long)	LEQLE**SIINFEKL**AAAAAK
UU23	**pTag-SIINFEKL(short)**	FIGITELKKLESKINKVF**SIINFEKL**
UU24	**pTag-Biotin**	FIGITELKKLESKINKVF-Biotin
UU25	**pTag-OVA (protein)**	FIGITELKKLESKINKVF-OVA (protein)
UU30	**pTag-** gp100$_{25\text{-}33}$ **(long)**	FIGITELKKLESKINKVFAVGAL**KVPRNQDWL**GVPRQL
UU33	gp100$_{25\text{-}33}$ **(short)**	**KVPRNQDWL**
UU44	**fTag-** CMV pp65$_{495\text{-}503}$ **(long)**	FITC(Ahx)AGILAR**NLVPMVATV**QGQNLKY
UU60	**pTag-** OT-II$_{323\text{-}339}$ (long)	FIGITELKKLESKINKVFISQAVH**AAHAEINEA**GR

protein concentration of the purified proteins was determined by measuring absorbance at 280 nm. Purity and integrity of the antibodies were assessed by SDS-PAGE, and monomeric content was determined by analytical SEC performed using a Bio SEC-3 column (300A, 7.8 × 300 mm) (Agilent), connected to an Agilent 1260 Infinity system and using 0.15 M NaxHyPO4 pH 6.8 at a flow rate of 1 mL min^{-1}. Endotoxin levels were determined using an Endosafe PTS instrument (Charles River) and cartridges with a minimum detection limit of 0.05 EU/mL.

The particle size distribution of the purified antibodies was analyzed by dynamic light scattering (DLS) using a Zetasizer Ultra (Malvern Panalytical). Antibody aggregation was assessed by analytical SEC, as described above, after one freeze–thaw cycle at −80 °C. Subsequently, the purified proteins were aliquoted and stored at −80 °C. Antibody expression and purification of Bi17-CP were outsourced to Absolute Antibody, using a similar procedure as just described. In short, HEK293 cells were used as expression hosts, purification performed by protein A affinity purification followed by preparative SEC and quality assessed by SDS-PAGE, analytical SEC, and measurements of endotoxin levels. All antibody constructs stocks had endotoxin level <1 EU/mL and final endotoxin levels in cultures were never above 0.03 EU/mL.

2.4. Tagged Antigenic Peptides (pTag-Ag)

Synthetic long peptides (SLPs) were custom purchased from Capra Science (Sweden) or TAG Copenhagen (Denmark). **Table 2** describes the amino acid sequence of the SLPs used.

2.5. Characterization of Antigen Binding

Parental and BiTag antibodies were assayed for CD40 binding and either of the two tag moieties, pTag or fTag. Biotinylated antigens were immobilized into the wells of a 384 ELISA plate via streptavidin (2 μg mL^{-1}) at a concentration of 0.1 μg mL^{-1} for human CD40 (Acro-Biosystems, #CD0-H82E8) and the model pTag (FIGITELKKLESKINKVF-biotin, Capra Biosciences, Lund, Sweden), named UU24 (Table 2), in PBT (PBS + 0.5% bovine serum albumin [BSA] + 0.05% Tween20). In the case of Bi17-CP, binding to a fluorescein isothiocyanate (FITC)-labeled mouse antibody was assessed to confirm the binding of the anti-fTag scFv. After each incubation step, plates were washed 3–4 times with PBS supplemented with 0.05% Tween20. The purified antibodies, diluted to 0.2 μg mL^{-1}, were added to the wells. Detection of binding was performed using horseradish peroxidase (HRP)-labeled anti-human IgG kappa antibody (Southern Biotech), followed by incubation with the chromogen Ultra TMB-ELISA (Thermo-Scientific Pierce). Signal development was stopped by adding 1 M sulfuric acid, and the absorbance was measured at 450 nm.

Simultaneous binding of the two antigen-binding sites was assessed by ELISA and SPR-based approach. In ELISA, an Fc-fused CD40 protein (RnD Systems, #1493-CDB) was immobilized in the wells, the purified antibodies added, followed by the addition of biotinylated peptides; UU24 or a scrambled peptide (EKLINKLSKIFKGTIE). The binding was detected by HRP-labeled streptavidin (Sigma-Aldrich), and development was performed as above. In the SPR experiments, a Biacore T200 instrument (Cytiva) was used. The biotinylated pTag UU24 was captured onto a streptavidin-coated SPR biosensor chip (Cytiva). BiTag antibodies were injected, diluted to reach a response level between 200 and 300 RU, followed by the injection of 50 nM CD40-Fc (RnD Systems, #1493-CDB). The surfaces were regenerated with 10 mM glycine-HCl, pH 2.1. The running buffer used was HBS-EP+ (0.01 M HEPES, pH 7.4, 0.15 M NaCl, 3 mM EDTA, 0.05% [v/v] Tween 20), and all samples were diluted in this buffer before injection.

Affinity and kinetic constants of the parental and BiTag antibodies were assessed using single cycle kinetics (SCK) SPR approach. An anti-human Fab antibody (Cytiva, #28 958 325), functioning as a capture ligand, was immobilized through EDC/NHS chemistry onto all four surfaces of a CM5-S amine sensor chip according to the manufacturer's recommendations. Antibodies were injected and captured onto the chip surface. Three channels were used to capture different antibodies, whereas channel 1 was used as a reference surface. Threefold dilution series of five concentrations of the two human CD40 versions; the monomeric avi-tagged version (AcroBiosystems, #CD0-H82E8) and the dimeric Fc-fused variant (RnD Systems, #1493-CDB), were prepared in HBS-EP+ buffer and sequentially injected over the chip surfaces. More specifically, a concentration range of 12–1000 nM CD40-avi and 0.6–50 nM CD40-Fc were used to analyze the 1150-based parental and BiTag constructs. The corresponding ranges for the CP-870893-based antibodies were 1.2–100 and 0.6–50 nM. Following a dissociation phase of 600 to 1200

s, the surfaces were regenerated with 10 mM glycine-HCl (pH 2.1). Response curve sensorgrams were obtained after removing the reference channel's response and a reference cycle (running buffer instead of antigen). Reaction rate kinetics constants were calculated using the Biacore T200 evaluation software 3.1 using the 1:1 Langmuir binding model for all interactions except for 1150-based constructs together with CD40-avi. Here, the steady state binding model was found more feasible and it was used to get an estimation of the affinity (dissociation constant, K_D).

Similarly, the affinity to the pTag was measured using a capture-based SPR-approach. The 14GIIICII scFv was captured through an immobilized anti-FLAG antibody, and measurement was performed as previously described by Preger et al.[19] The corresponding binding of the BiTag antibodies was performed using capture through the anti-Fab antibody as described above. The pTag-Ag, UU30, was injected in threefold dilution series of five concentrations ranging between 0.62–50 nM, and reaction rate kinetics were calculated using the 1:1 Langmuir binding model as described.

2.6. Analysis of Binding to Fc gamma Receptors (FcγR) and Neonatal Fc Receptor (FcRn)

Binding to a panel of different Fc receptors was also measured by SPR using a Biacore T200 instrument of the four parental antibodies and all the BiTag antibodies except for Bi17-CP. Biotinylated CD40 (AcroBiosystems, #CD0-H82E8) was captured onto a streptavidin-coated SPR biosensor chip (Cytiva) to a response unit (RU) level ≈2000. The different antibodies were injected, aiming for RU levels of ≈240 and ≈320 for parental and BiTag antibodies, respectively. This step was followed by injection of 100 nM of the various human recombinant produced Fc receptors (R&D systems); FcRn (#8639-FC-050), FcγRIIIA, (#4325-FC-050), FcγRIIIB (#1597-FC-050/CF), and FcγRIIA(#1330-CD-050). For FcRn, a lower pH phosphate buffer (100 mM NaPO4, 150 mM NaCl, 0.05% Tween20, at pH 6.0) was used as a running and dilutant buffer, whereas HBS-EP+ (pH 7.4) was used for the other receptors. The surfaces were regenerated using 10 mM glycine-HCl (pH 2.1). The obtained sensorgrams were visually inspected, and the binding response of the bispecific antibodies was compared to the matching parental IgG, taking into account differences in antibody capture levels and molecular weights.

2.7. LC-MS/MS

All pTag peptides and tryptic antibody peptides from Bi10-1150 and 1150–2 were quantified using a TQ-S micro triple quadrupole mass spectrometer connected to an Acquity UHPLC system (Waters Corp). For the pTag peptides UU05, UU23, and UU30, the chromatographic separation was carried out using a BEH C8 column (1.7 μM, 2.1 × 50 mm) with a linear gradient from 0% to 100% mobile phase B within 1.6 min. A reversed-phase Acquity Peptide CSH C18 column (1.7 μm, 2.1 mm × 100 mm) was used for the tryptic antibody peptides, eluted using the following gradient: 0.0–1.0 min, 2% B; 1.10 min, 10% B; 3.1 min, 30% B; 3.6–4.1 min, 100%; B 4.2–6.0 min, 2% B. Mobile phases used consisted of: A) 0.1% formic acid in milliQ H2O and B) 0.1% formic acid in acetonitrile (ACN), and the flow rate was set to 0.5 mL min^{-1}.

All analytes were positively ionized in electrospray (ESI) and monitored in multiple reaction monitoring (MRM) mode with following transitions, collision energy (CE) and cone voltage (Cone): 718.8 > 810.3 (CE: 18 eV, Cone: 15 V) and 616.2 > 740.1 (CE: 12e V, Cone: 10 V) for UU30, 611.2 > 698.5 (CE: 16 eV, Cone: 35 V) and 763.8 > 698.5 (CE: 16 eV, Cone: 35 V) for UU23, 830.5 > 929.8 (CE: 25 eV, Cone: 25 V) and 830.5 > 972.4 (CE: 25 eV, Cone: 15 V) for UU05, 412.8 > 327.1 (CE: 10 eV, Cone 23 V) for GLPAPIEK 2+ (surrogate peptide for quantification of Bi10-1150 and 1150–2), and 423.9 > 662.7 (CE 10 eV, Cone: 23 V) for ALPAPIE[K]2+ (internal standard). The source parameters were set to 0.8 or 2.5 kV for capillary voltage for pTag peptides and tryptic antibody peptides, respectively, 150 °C for source temperature, 650 °C for desolvation gas temperature and 1200 L h^{-1} for desolvation gas flow.

2.8. In Vitro Peptide Stability Assay

UU05, UU23, or UU30 (1–10 μM) were incubated in mouse plasma (K2EDTA anticoagulant, Innovative Research LC), human plasma (sodium citrate anticoagulant, Uppsala University Hospital), or in PBS buffer (pH 7.5) with 2% BSA at 37 °C. The peptides were incubated alone, with the parental antibody 1150–1, or with the BiTag antibody Bi9-1150, at a molar ratio of 1:1 to 1:2 (antibody:peptide), for a duration between 4–24 h. The reaction was stopped at designated time points by adding three volumes of ice-cold methanol. The samples were vortexed and centrifuged for 20 min at 3220 × g at 4 °C, followed by evaporation of supernatant and subsequent reconstitution of dried material in (100 μL) of 2% ACN and 0.5% formic acid in water prior to analysis with LC-MS/MS.

2.9. In Vivo Peptide Stability Assay

C57BL/6 mice were injected using hock injection with the pTag-peptide UU30 +Bi10-1150 or UU30 + 1150–2. Each mouse received the same antibody dose of 2 mg kg^{-1} body weight. The peptide UU30 was co-injected at a molar ratio of 1:2 of antibody to the peptide. Plasma samples along with the draining popliteal and the draining inguinal lymph nodes were collected from the mice at the 0.5, 1.5, 4, and 8-hour time points, and the samples were analyzed for the presence of antibody and intact pTag-peptide. For sample preparation, lymph nodes were weighed individually (Micro balance, Sartorius micro M3P) and homogenized using Ultrasonic processors (Vibra-Cell VCX 130 with 3 mm microtip, SONICS). To each lymph node (popliteal; 0.35 to 3.8 mg, inguinal; 0.43–6.9 mg) 50 μL of 6.4 M urea in 0.1 M ammonium carbonate (ABC) buffer were added before processing. The total protein concentration of the lymph node preparation was measured with the tryptophan fluorescence method.[20] For the quantification of UU30 in the study samples, plasma or lymph node homogenate samples (20 μL) were precipitated with 80 μL methanol. After centrifugation for 20 min (13 000 RPM, MiniSpin Plus, Eppendorf), 85 μL were transferred to glass vials and evaporated (Genevac

EZ-2) before resuspension in 70 µL 5% ACN and 0.5% formic acid in water. Bi10-1150 and 1150–2 were quantified by tryptic digestion, SPE for sample concentration and clean up, followed by LC-MS/MS analysis using a signature peptide (GLPAPIEK, 2+) together with an isotopically labeled analog of the signature peptide as the internal standard. Fifteen (15 µL) microliters of plasma was diluted with 37 µL urea (9 M) in 100 mM ABC buffer on a LoBind 96-well plate (Greiner Bio-One 96-Well Conical Bottom) and denatured at ambient temperature for 20 min in a plate shaker at 440 rpm. Alternatively, 15 µL of lymph node homogenate already in 6.4 M urea were added to the plate. Five (5 µL) microliter of dithiothreitol were added (5 mM final concentration) to reduce denatured samples for 40 min at 350 rpm, followed by alkylation with 5 µL of iodoacetamide (10 mM final concentration) at ambient temperature. Unreacted iodoacetamide was quenched with 5 µL of dithiothreitol for 30 min. After dilution with 0.1 M ABC (pH 7.8, final urea concentration 1 M), trypsin was added to an enzyme:substrate (E:S) ratio of 1:20 for the plasma samples, and a median E:S ratio of 1:27 for the lymph node samples (90% of samples between 1:7–1:65). Samples were incubated at 37 °C overnight under agitation at 600 rpm. The reaction was stopped by adding 10% trifluoroacetic acid (2% final concentration), followed by centrifugation for 5 min at 4 °C and 805 × g. The digested samples were purified and concentrated using ProteinWorks µElution SPE Clean-up Kit: MCX (Mixed-Mode Cation-eXchange; Waters). The eluates were then diluted with 50 of µL 5% formic acid in water with stabile isotype labeled internal standard ALPAPIE[K] ($^{13}C_6$, $^{15}N_2$). A volume of 7.5 µL of sample aliquots was injected into LC-MS/MS system.

2.10. Bone Marrow Cell Isolation and BMDC Differentiation

Bone marrow precursor cells from femora and tibiae of adult transgenic human CD40-expressing mice (tghCD40) or wild type (WT) C57BL/6 mice were isolated under sterile conditions. After removing the soft tissue, the bones were disinfected with 70% ethanol before the bone marrow was cut-opened at the bone epiphyses. Bone marrow cells were flushed using IMDM until the bone core became white. Cell clumps were passed through a 70 µm cell strainer to form a single-cell suspension. The cells were washed by centrifugation before they were frozen in 10% DMSO FBS at −160 °C until the time of usage. For BMDC differentiation, bone marrow precursor cells were thawed and cultured for eight days in non-TCT plates at a concentration of 2.5×10^5 mL^{-1} in IMDM medium supplemented with 10% FBS, 1% penicillin/streptomycin, 1% HEPES, and 50 µM 2-mercaptoethanol in the presence of 20 ng mL^{-1} mGM-CSF. Half of the medium was exchanged on day 3 and day 6 and replaced with fresh complete IMDM with 20 ng mL^{-1} mGM-CSF. On day 8, cells were harvested by gently washing the plate with a pre-warmed medium and were run in flow cytometry to assess DC differentiation (CD11b and CD11c), hCD40 expression, and activation markers (CD86 and MHC-II).

2.11. BMDC Maturation and Activation

After eight days of differentiation of bone marrow precursors, 1×10^5 immature BMDC were plated per well in a 96-well TCT plate (Standard F, Sarstedt #83.3924). Different anti-CD40 antibodies, parental or BiTag (Table 1), were added to each well in a concentration ranging between 100–0.08 nM. BMDC were cultured for 48 h in IMDM medium with 20 ng mL^{-1} mGM-CSF before the supernatant was collected for IL-12 ELISA. Tests were run in duplicates.

2.12. In Vitro T Cell Activation/Expansion Assays (B3Z/pmel/OT-II)

After eight days of differentiation of bone marrow precursors, 25 000 immature BMDC were plated per well in a 96-well TCT plate (Standard F, Sarstedt #83.3924). Different concentrations of the SLPs UU5 and UU10 (for B3Z assay), UU30 (for pmel assay), or UU60 (for OT-II assay) (Table 2) with a different combination of the test anti-CD40 antibodies (Table 1) were added to the immature BMDC culture. After 24-hour incubation (2-hour incubation for UU60, with minimal disturbance of the cells, the supernatant containing the peptide/antibodies mix was removed, and the wells were washed by centrifugation twice with a pre-warmed IMDM to remove any remaining unbound peptide/Ab mix. For the T cell activation assay (B3Z assay), B3Z cells were co-cultured with BMDCs, and the co-culture was incubated for a further 24 h before the cells were lysed by adding the lysis β-mercaptoethanol buffer supplemented with the substrate CPRG. Cells were lysed to allow the β-galactosidase enzymatic activity to break down CPRG and lead to color change corresponding to the level of B3Z cell activation. Absorbance was read at 595 nm after 6 h. A positive control short peptide (SIINFEKL) (1 µM) was included in all experiments that activate B3Z and result in saturation of the colorimetric reaction and the absorbance readout. For the T cell expansion assay (pmel and OT-II assays), carboxyfluorescein succinimidyl ester (CFSE) (Thermo-Fisher) labeled pmel-1 or OT-II cells were co-cultured with BMDCs, and the co-culture was incubated at 37 °C/5% CO_2 for further 72 h before the pmel-1 cell expansion and activation were assessed using flow cytometry.

2.13. CD14$^+$ Monocyte and Peripheral blood mononuclear cells (PBMCs) Isolation, Human T Cell Expansion Assay

PBMCs were isolated from Buffy Coats, donated from healthy volunteers, by Ficoll separation using SepMate (Stemcell Technologies) together with cell density gradient Ficoll Paque Premium (GE Healthcare) according to the manufacturer's protocol. Furthermore, CD14$^+$ monocyte separation was performed with MACS human CD14 microbeads isolation kit (Miltenyi Biotec). Isolated CD14$^+$ cells were cultured for six days in complete RPMI 1640 medium with GlutaMAX, supplemented with 10% FBS, 1% of 100 IU/mL penicillin/streptomycin, 1% HEPES 1 M and 0.2% β-mercaptoethanol 50 mM (Gibco), along with 150 ng mL^{-1} hGM-CSF and 50 ng mL^{-1} hIL-4 (Peprotech) to drive differentiation into immature DCs. Half of the medium was exchanged every 2–3 days, supplemented with 150 ng mL^{-1} hGM-CSF and 50 ng mL^{-1} hIL-4 for the total volume medium. Immature monocyte-derived dendritic cells (moDC) were pulsed with the UU44 peptide, an fTag-CMV pp65 – HLA-A*0201 (NLVPM-VATV), for 24 h in the presence or the absence of the

BiTag or parental anti-CD40 antibodies. The cells were washed twice by centrifugation before the autologous T cell fraction of the buffy coat, isolated with a pan T cell purification kit (Miltenyi Biotec), was co-cultured with the pulsed moDC for seven days. CMV pp65-specific T cell expansion was assessed by flow cytometry using HLA-A*02:01 CMV pp65 tetramer (Clone: T01009) (MBLinternational).

2.14. Peptide Uptake and Intracellular Release

To study BiTag platform-mediated peptide uptake and intracellular release, the FITC-labeled peptide UU44 and the BiTag antibody Bi17-CP were used. In brief, UU44 has FITC attached to the N-terminal of the peptide as an fTag that is quenched when bound to the anti-FITC scFv of Bi17-CP. A pre-mixed UU44/Bi17-CP mixture, where FITC is quenched by binding to scFv, was incubated with moDCs at 37 °C to allow peptide/antibody uptake. The uptake process was terminated at the time points: 5 min, 0.5 h, 1 h, 2 h, 4 h, or 6 h by adding ice-cold PBS and keeping the cells on ice. The cells were washed to remove excess UU44. Trypan blue was used to quench (Q) the FITC signal to discriminate the extracellular FITC signal from the intracellular signal of UU44. The amount of intracellularly released (free) UU44 was quantified as a percentage of fluorescent cells using flow cytometry for each time point.

2.15. In Vivo T Cell Expansion Experiment

Adult C57BL/6 mice (18–20 g weight) were used for in vivo antigen uptake and T cell expansion model. Groups of C57BL/6 mice (6-10 mice) received 9–11 × 10^6 CFSE-labeled pmel-1 cells intravenously (i.v.) via tail vein injection and 1–3 × 10^5 tghCD40 or WT immature BMDC (right side footpad injection) on day 0. On day 1, different combinations of BiTag or parental anti-CD40 antibodies and the hgp100 containing pTag-Ag UU-30 or the control short hgp100 peptide UU33 (Table 2) were injected on the right-side hock to investigate the peptide uptake in vivo. After 3–6 days, the draining popliteal, draining inguinal, non-draining inguinal lymph nodes and spleens were harvested and passed via 70 µm cell strainers to achieve single-cell suspensions. Pmel-1 cell accumulation and activation were assessed in the lymph nodes and spleens by flow cytometry staining of CD90.1 and the T cell activation marker ICOS.

2.16. Flow Cytometry

The following anti-mouse fluorescent-labeled antibodies from BioLegend were used for flow cytometry (clone): anti-CD11c (N418), anti-CD11b (M1/70), anti-CD90.1 (OX-7), anti-ICOS (C398.4A), anti-I-A/I-E (M5/114.15.2), anti-CD86 (GL-1), anti-hCD40 (5C3) (from BD), anti-CD45 (30-F11), anti-CD3 (17A2), anti-CD4 (RM4-4), and anti-CD8 (53-6.7). The following anti-human fluorescent-labeled antibodies from BioLegend were used for flow cytometry (clone): anti-CD3 (UVHT1), anti-CD8 (SK1), anti-CD56 (NCAM), anti-TNFα (Mab11), and anti-IFNγ (4S.B3). For flow cytometry staining, 1–5 × 10^5 cells were pelleted in flow cytometry tubes/plates by centrifugation before the antibody staining cocktail was added to the cells. Cells were incubated at 4 °C for 20 min before being washed in PBS/1% BSA. A fixation/permeabilization step was performed using Cytofix/Cytoperm solution (BD) for intracellular cytokine staining. Cells were run in CytoFLEX Flow Cytometer (Beckman Coulter Life Sciences).

2.17. IL-12 ELISA

ELISA plates (Sarstedt 82.1581.200) were coated with purified anti-mouse IL-12 antibody (clone C15.6, BioLegend) overnight at 4 °C. Plates were blocked in PBS/1% BSA before diluted supernatant was added to the ELISA plate. Thereafter, secondary biotinylated anti-mouse IL-12 (clone C17.8, BioLegend) was added before Streptavidin/HRP (Code no. P0397, Dako) was incubated in the plate. Lastly, the ELISA reaction was developed by adding TMB buffer (34 028, Sigma), and the reaction was stopped by adding 1 M sulfuric acid. Absorbance was read at 450–570 nm.

2.18. Whole Blood Loop Assay (WBLA)

Blood loop experiments were performed as described previously.[21] In brief, whole blood samples were collected from healthy blood donors, and the blood was added to surface heparinized PVC loops together with the peptide/antibody of interest in the presence of brefeldin-A. The blood loops were attached to a circulating wheel to allow the blood to be in motion and prevent coagulation. After 4–6 h of incubation at 37 °C, the blood was collected, the red blood cells were lysed, and the blood samples were stained and analyzed with flow cytometry for intracellular cytokine release.

2.19. Ethical Considerations

All animal studies were approved by Uppsala regional ethical committee (ethical approval for animal experiments Dnr: C304214/16 (C42/14) and 5.8.18-02686/2019), and all human blood experiments were approved by Uppsala regional ethical committee (DNR 2017/165 and DNR 2018/206). Informed consent of all participating subjects was obtained.

2.20. Data and Statistical Analysis

Flow cytometry data were analyzed by FlowJo, LLC. GraphPad Prism 7 was used to plot the graphs and to perform statistical analysis. The sample size for the in vivo experiments was 3–14 animals per treatment group. All data are presented as mean ± SEM. Unpaired two-tailed non-parametric Mann–Whitney test or Kruskal Wallis test with Dunn's post-test were used to assess significant differences and obtain *p*-values.

3. Results

3.1. ADAC Design and Characterization

Targeting CD40 enhances DC antigen uptake and presentation to T cells, including cross-presentation to $CD8^+$ T cells.[22] Herein,

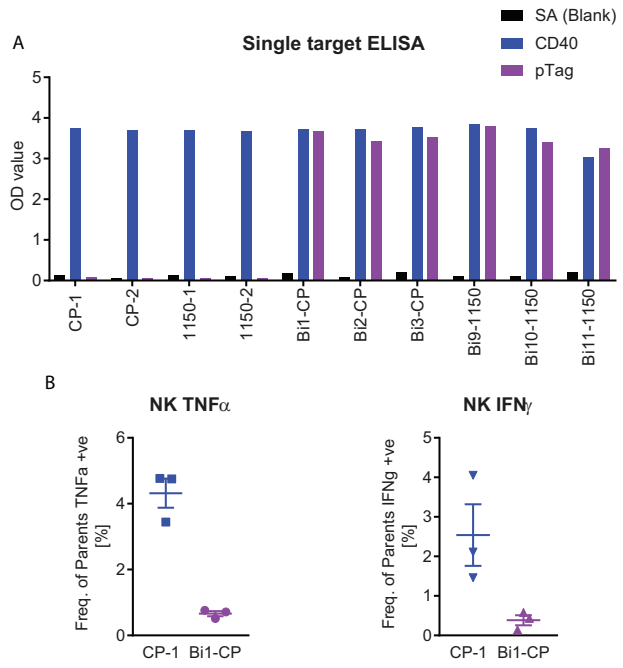

Figure 2. Target binding and FcγR mediated NK cell activation. A) Target binding was assessed by ELISA for the BiTag antibodies and their counterpart parental anti-CD40 antibodies (see Table 1). The antibody constructs were analyzed on microtiter plates coated with CD40-biotin-streptavidin (CD40, blue), UU24-biotin-streptavidin (pTag, magenta), or streptavidin only (SA, black). OD values (Abs 450 nm, y-axis) are the average of duplicates. B) NK cell activation following stimulation of whole human blood with Bi1-CP or the counterpart parental CP-1. Data are shown as mean +/−SEM.

a peptide delivery platform called ADAC was designed to contain a tetravalent bispecific antibody targeting CD40 and a peptide tag moiety, also called pTag. The bispecific antibody, also named BiTag, consists of a fully human agonistic anti-CD40 antibody covalently linked, via a glycine-serine peptide linker, to two identical scFv targeting the pTag (anti-pTag) (Figure 1). A set of seven BiTag constructs and four monoclonal anti-CD40 antibodies were designed and produced. Based on the literature, the roles of IgG subclass (IgG1 or IgG2), anti-CD40 antibody (CP-870893 or 1150), and the location of the anti-Tag fusion (CH3 or CL linkage) were evaluated (Figures 1A and 1B, and Table 1). The pTag-Ag is a SLP of 30–40 amino acid length consisting of two domains; a constant pTag, to which the scFv binds, and a variable peptide sequence that accommodates the antigenic epitope (Ag) of interest within a flanking sequence of amino acids. Herein, an 18-mer linear B cell epitope,[17] pTag, FITC[18] fTag, were used as the constant tag for concept evaluation (Table 2). The design of the BiTag allows for the simultaneous delivery of the agonistic CD40 signaling and the cargo antigen associated to the same DC, ensuring robust T cell activation (Figure 1C).

The biophysical characterization using SEC and DLS revealed minimal aggregation of the BiTag compared to the parental anti-CD40 antibodies (Figure S1, Supporting Information). The expressed BiTag and parental antibodies were confirmed to bind to their targets, CD40 and the pTag, by ELISA (**Figure 2**A). The BiTag antibodies bound CD40 within the same affinity range as the parental antibodies CP-870.893 or 1150, regardless of subclass or whether the scFv was fused to the antibody heavy or light chain as assessed by SPR (**Table 3**). As noted, there is a significant difference in measured K_D-values for the two CD40 constructs, likely explained by the difference in quaternary structures—the avi-tagged construct is monomeric, whereas CD40-Fc is, due to the Fc-fusion, dimeric leading to an avidity contribution. As K_D is used to describe the strength of a monovalent interaction, the report herein rather includes the apparent affinity (denoted as $^{app}K_d$) for the binding to CD40-Fc. As CD40 clusters on the cell surface, one may argue that the reported $^{app}K_d$ is more relevant for describing how these antibodies would interact with the target on cells, both in vitro and in vivo. SPR measurements also confirmed a high affinity for the synthetic peptide and the anti-pTag scFv in the form of BiTag (Table 3). The measured kinetic parameters are similar between the different BiTag and also very similar to values previously obtained for the scFv in soluble format (data not shown).

Importantly, using both ELISA and SPR-based sandwich experiments, BiTag antibodies were shown to simultaneously bind both their respective cognate targets (Figure S2, Supporting Information). Furthermore, SPR analyses indicated that the position of the scFv had no or minimal effect on the binding to FcRn. In contrast, a decrease in binding of a majority of the BiTag antibodies to Fcγ receptors analyzed was observed (**Table 4**). Most inhibition of binding was observed for FcγRIIIB, followed by FcγRIIA, while the least reduction in binding of the three was observed for FcγRIIIA. It should be noted that the overall kinetic profiles of the interactions to the FcγR do not seem to be affected when comparing the binding of the BiTag to its corresponding parental antibody. It is merely the level of response that changes (data not shown).

Next, a WBLA[17,21,23] was used to study the BiTag antibodies interaction with FcγRIIIA on natural killer (NK) cells using whole human blood. The WBLA has previously been shown to provide information on the interaction between monoclonal antibodies and the FcγRIIIA on NK cells, resulting in NK cell activation and cytokine release.[23] Using this system, two distinct profiles were noted based on antibody subclass, with NK cell activation taking place with IgG1 subclass but not IgG2 (Figure S3, Supporting Information). Although the SPR analyses indicated a retained FcγRIIIA binding for the BiTag of IgG1 subclass, Bi1-CP (Table 4), the parental CP-1 induced NK cell cytokine production in the WBLA, while the BiTag counterpart Bi1-CP did not (Figure 2B). This indicates that SPR analyses should always be complemented with biological readouts to fully understand the nature of how a bispecific antibody interacts with other cells.

3.2. Stability and DC Internalization of BiTag Platform Coupled Antigenic Peptide

Naked unmodified therapeutic peptides are fragile drug entities. To evaluate peptide half-life, intact pTag-Ag was evaluated over time in mouse and human plasma. This was performed using an in vitro stability experiment using the peptides UU05, UU23, and UU30 in PBS (pH 7.5) with 2% BSA and in plasma derived from mice or humans. During a 17-hour experiment, all three peptides had a half-life of ≈4 h up to no observed degradation in

Table 3. SPR analyses of target binding of parental and BiTag antibodies. The reaction rate kinetics constants (association rate constant [k_a [M^{-1} s^{-1}]], dissociation rate constant [k_d [s^{-1}]], and equilibrium of dissociation [K_D [nM]]) were calculated based on a 1:1 kinetic binding model for all interactions except for 1150-based antibody constructs together with CD40-avi. Here, the steady state binding model was used to get an estimation of K_D. For binding to CD40-Fc, the k_a and k_d contain an avidity component due to the dimeric nature of the antigen. Therefore, the apparent affinity constant ($^{App}K_D$) is used to describe these interactions.

	Binding to CD40-Fc			Binding to CD40-avi			Binding to pTag-Ag (UU30)		
Antibody	$^{app}K_D$ [nM]	k_a [1/Ms]	k_d [1/s]	K_D [nM]	k_a [1/Ms]	k_d [1/s]	K_D [nM]	k_a [1/Ms]	k_d [1/s]
Bi1-CP	0.14	2.3E+05	3.1E-05	15	8.4E+04	1.2E-03	1.0	5.3E+05	5.4E-04
Bi2-CP	0.16	1.9E+05	2.9E-05	14	8.6E+04	1.2E-03	0.9	6.0E+05	5.4E-04
Bi3-CP	0.12	2.4E+05	2.8E-05	14	7.8E+04	1.1E-03	0.9	4.8E+05	4.3E-04
Bi9-1150	1.5	2.7E+06	3.9E-03	1000 ± 300	–	–	0.9	5.8E+05	5.4E-04
Bi10-1150	1.7	2.6E+06	4.3E-03	1000 ± 300	–	–	1.2	6.4E+05	7.6E-04
Bi11-1150	1.7	2.1E+06	3.7E-03	1000 ± 300	–	–	0.7	5.4E+05	3.8E-04
Bi17-CP	0.17	1.8E+05	3.0E-05	14	8.2E+04	1.2E-03	No binding detected		
CP-1	0.12	2.0E+05	2.3E-05	15	7.6E+04	1.2E-03	No binding detected		
CP-2	0.16	2.0E+05	3.1E-05	14	8.2E+04	1.2E-03	No binding detected		
1150-1	1.8	1.5E+06	2.7E-03	1000 ± 300	–	–	No binding detected		
1150-2	1.4	1.5E+06	2.1E-03	1000 ± 300	–	–	No binding detected		

Table 4. Normalized binding response of the BiTag antibodies to FcRn and to three different FcγR; FcγRIIIA (CD16a), FcγRIIIB (CD16b), and FcγRIIA (CD32a). The binding response values were normalized based on the signal obtained for respective parental IgG to each of the different Fc receptors, and this value was set to 100%. The binding response for each sample was taken at the end of the association phase. ++ indicates a normalized binding response ≥80%, + indicates a normalized binding response <80% and – indicates that no binding was detected.

Antibody	FcRn	FcγRIIA	FcγRIIIA	FcγRIIIB
Bi1-CP	++	++	++	+
Bi2-CP	++	+	–	–
Bi3-CP	++	+	++	+
Bi9-1150	++	+	++	+
Bi10-1150	++	+	–	–
Bi11-1150	++	+	++	+
CP-1	++	++	++	++
CP-2	++	++	–	–
1150-1	++	++	++	++
1150-2	++	++	–	–

PBS, 2% BSA (Figure S4, Supporting Information). Compared to PBS, considerably rapid degradation of UU30 and UU05 was noted in mouse and human plasma, respectively. The half-life for UU30 in mouse plasma was 18 min, and the half-life for UU05 in human plasma was 6 min (Figure S5, Supporting Information).

Next, peptide integrity of UU30 and UU05 was studied in mouse and human plasma, respectively, in the presence of antibodies. The peptides were incubated at 37 °C with the mouse or human plasma alone, mixed with the 1150–1 parental antibody or with Bi9-1150. In mouse plasma, the binding of UU30 to the BiTag improved peptide stability with no detectable degradation of the peptide during the 4-hour experiment. In contrast, for the peptide alone or peptide mixed with the parental anti-CD40 antibodies without binding properties to the peptide, the half-life of the peptide was measured to be ≈19.5 min (**Figure 3**A). Moreover, in human plasma, binding of the peptide UU05 to Bi9-1150 resulted in slower degradation, with a half-life of 24 min compared to an average of 13 min when UU05 was incubated in the plasma alone or with the parental antibody 1150–1 (Figure 3B). Using protease inhibitors in mouse plasma displayed a prolonged half-life from 0.4 to 3.7 h. Notably, the increased stability of the BiTag-bound peptide, in this experiment Bi10-1150, did not synergize by the addition of protease inhibitors, and the half-life of Bi10-1150 bound UU30 with and without the protease inhibitors was 6.1 and 6.4 h, respectively (Figure S6, Supporting Information). This suggests the improved peptide stability by BiTag is likely via protection from degradation by proteases.

To confirm the protective properties of the ADAC technology in vivo, intact pTag-Ag and antibody in plasma and the draining popliteal and inguinal lymph nodes of C57BL/6 mice following hock injection with the UU30 peptide, mixed with either the 1150–2 parental antibody or with the Bi10-1150 was quantified. Each mouse received a 2 mg kg^{-1} body weight of antibody with the peptide UU30 co-injected at an antibody to the peptide molar ratio of 1:2. The mice were sampled at 0.5, 1.5, 4, and 8 h after vaccination. Plasma concentrations of the antibodies in the two different groups were in a close range, ranging from 8.5–55.0 (1.7–11 μg mL^{-1}) and 18.7–126.7 nM (2.8–19 μg mL^{-1}) for Bi10-1150 and 1150–2, respectively (Figure 3C). For the pTag-Ag, in the group treated with UU30 + 1150–2, no peptide was detectable in the plasma at any time point (LLOD ≈0.2 nM). In contrast, UU30 was detected at a concentration ranging from 10–65 nM in plasma when using the Bi10-1150 delivery strategy, corresponding to 2–14% of the injected dose if the mouse plasma volume is ≈0.9 mL. This supports the BiTag's protective effect on the antibody-bound peptide in vivo (Figure 3C). The plasma Bi10-1150:UU30 ratio dropped from 1.6 at the 0.5-hour time point to 0.4 at the 8-hour time point, indicating that UU30 had a shorter half-life in plasma than the BiTag (Figure 3D).

Both 1150–2 and Bi10-1150 antibodies were detectable at similar levels, in the lymph node, with the maximum average

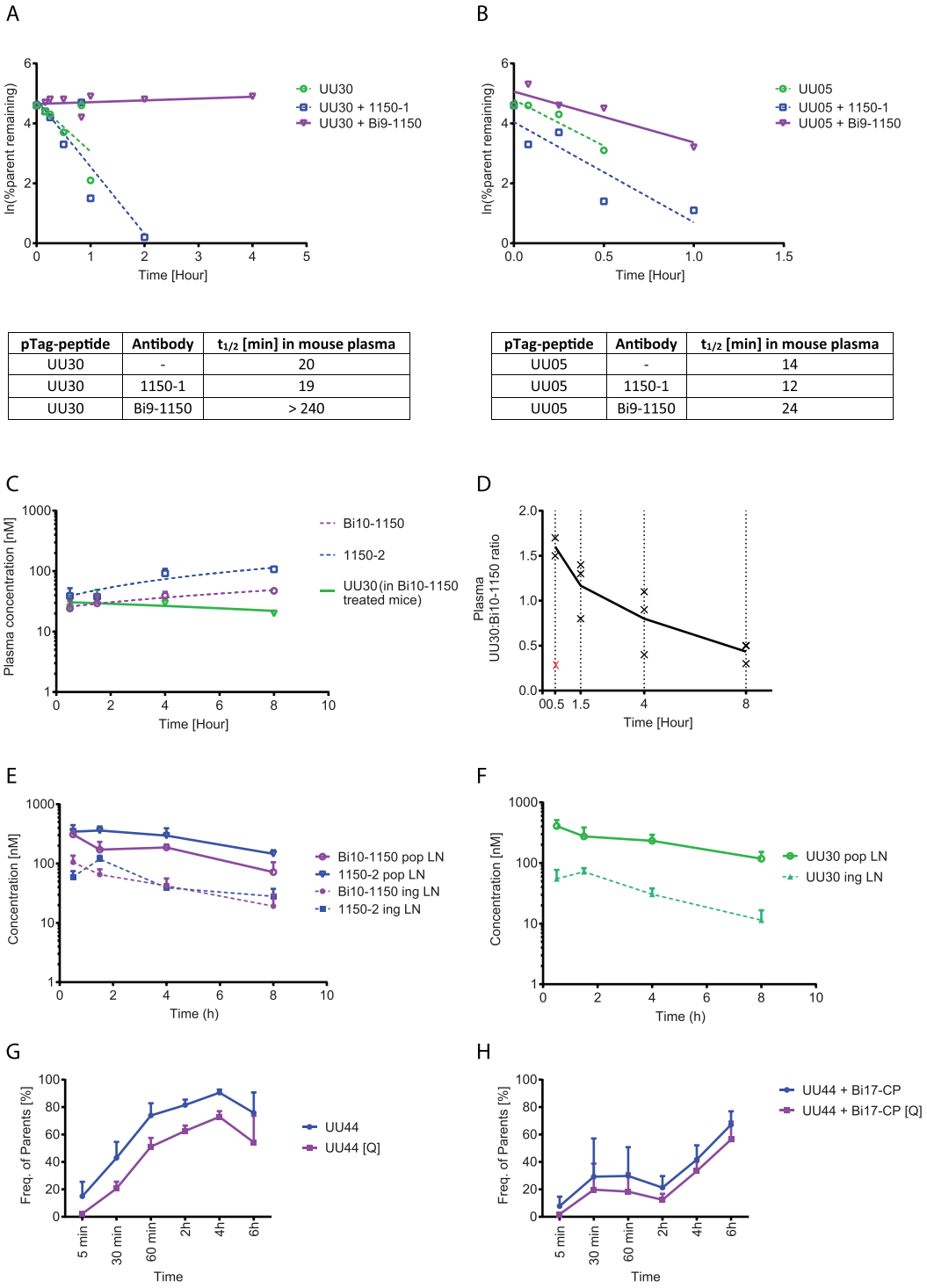

pTag-peptide	Antibody	$t_{1/2}$ [min] in mouse plasma
UU30	-	20
UU30	1150-1	19
UU30	Bi9-1150	> 240

pTag-peptide	Antibody	$t_{1/2}$ [min] in mouse plasma
UU05	-	14
UU05	1150-1	12
UU05	Bi9-1150	24

Figure 3. In vitro and in vivo peptide stability and intracellular release. In vitro peptide stability in A) mouse and B) human plasma. The pTag-peptide A) UU30 and B) UU05 were incubated for 4 h in the 37 °C plasma alone, mixed with the parental antibody 1150–1 or mixed with the BiTag antibody Bi9-1150. The remaining intact peptide concentration was detected using mass spectrometry. C) The in vivo integrity of UU30, 1150—2, and Bi10-1150 in mouse plasma were determined by mass spectrometry following vaccination in the hock at 2 mg mL^{-1} antibody and 1:2 Bi10-1150:UU30 or 1150–2:UU30 molar ratio. D) Bi10-1150:UU30 ratio in mouse plasma over time after the in vivo administration. Each dot represents the mean ($n = 3$) per time point E) Bi10-1150 and 1150–2 concentration in the draining popliteal and the draining inguinal lymph nodes following hock administrated vaccination. F) UU30 concentration in the draining popliteal and the draining inguinal lymph nodes following hock administrated vaccination with UU30 and Bi10-1150. G) Internalization kinetics for the fTag containing peptide UU44 by moDC. Trypan blue was used to quench extracellular peptides [Q]. H) Internalization kinetics for the fTag-containing peptide UU44 when complexed with the Bi17-CP by moDC. Trypan blue was used to quench extracellular peptides [Q]. Dots represent the mean. Error bars represent SEM. ln = natural log, BSA = bovine serum albumin, LN = lymph node, pop = popliteal, ing = inguinal.

concentration of 344.8 ± 172.7 and 309.8 ± 72.6 nM in the popliteal lymph node 0.5 h after administration for 1150–2 and Bi10-1150, respectively (Figure 3E). However, UU30 was only detected in the group treated with Bi10-1150, both when analyzing the popliteal and the inguinal lymph nodes (Figure 3F).

Next, peptide internalization and release were investigated when delivered by the ADAC strategy. A FITC tagged CMV $pp65_{495\text{-}503}$ (NLVPMVATV) peptide (fTag-NLV; UU44) was used to study the release of the cargo over time inside APC. A BiTag version Bi17-CP, which has the anti-fTag as a scFv, was used. First, the binding of Bi17-CP to the UU44 was confirmed by demonstrating that the Bi17-CP quenches the fluorescence signal upon fTag-Bi17-CP interaction (Figure S7, Supporting Information). To investigate the internalization kinetics, human moDCs were pulsed with the UU44 peptide either alone or when bound to Bi17-CP. The fluorescence signal was assessed when cells were stained with trypan blue to quench any extracellular fluorescent signal (UU44 [Q]) or without quenching the extracellular signal (Figure 3G,H). Pulsing the moDCs with UU44 alone resulted in a steady increase of the intracellular fluorescence with time, indicating the cells' continuous uptake in a closed system where peptides are not eliminated as would be the case in vivo (Figure 3G). When complexed with the BiTag Bi17-CP, the fluorescent signal of UU44 was initially low (quenched). After 2 h, the fluorescence increased steadily, indicating intracellular dissociation and release of the fTag-peptide from Bi17-CP takes place after 2 h and continues to be released up to 6 h (Figure 3H).

3.3. The BiTag Platform Activates DC and Enhances Antigen Uptake and Presentation In Vitro

To evaluate the agonistic property of the different BiTag and parental antibodies, BMDC from a tghCD40 mouse strain were used.[10] By stimulating immature BMDCs (imBMDCs), it was apparent that the BiTag retained the agonistic activity. Interestingly, while the 1150-based BiTag constructs showed comparable IL-12 production to their parental counterparts (**Figure 4**A), CP-870.893-based BiTag constructs induced a significant increase in DC IL-12 production compared to the parental CP-870.893 antibodies (Figure 4B,C).

Furthermore, while IgG2 isotype induced higher agonistic activity and IL-12 production in the format of the parental antibody, compared to the IgG1 format, this difference was less clear when comparing IgG1 and IgG2 of the BiTag versions of the antibody. Although puzzling, this effect could be attributed to changes in FcγR interaction that could be potentially induced by linking the scFv to the antibody backbone or clustering of the antibodies on the cell surface or an inherited feature unique to the transgenic BMDCs. An experiment to compare aggregated and 99% monomeric fractions of the bispecific antibodies was also performed to determine whether aggregation had any role in the results. There was no difference in the agonistic activity between aggregated and pure monomeric antibodies in the cell assay (data not shown). Of note, agonistic IL-12 stimulation was not observed when treating WT BMDC that lack human CD40 (Figure S8, Supporting Information); also supporting that there was no non-target mediated protein aggregation causing the stimulation.

T cell activation was studied by co-cultured tghCD40 BMDC with B3Z hybridoma cells.[14] Treatment of tghCD40 BMDCs with a mixture of BiTag antibodies and the pTag-Ag UU05, which is a pTag-OVA(SIINFEKL) (Table 2) mixture resulted in a substantial increase in $CD8^+$ T cell activation compared to treating the cells with the antigen UU05 alone (Figure 4D,E). Mixing parental agonistic anti-CD40 antibodies CP-1, CP-2, 1150–1, and 1150–2 with UU05 did not improve antigen presentation and T cell activation. Besides the pTag-Ag UU05, a B3Z co-culture with the BiTag antibodies with UU25, a whole OVA protein conjugated with a pTag at OVA:pTag of 1:4 ratio, or with the SLP UU10 that include the antigenic epitope SIINFEKL but lacks the pTag, was performed. Like UU05, pTag/UU25 combination displayed a synergistic activity and induced higher T cell activation compared to treatment with UU25 alone or with parental agonistic CD40 antibodies (Figure 4F). In contrast, BiTag antibodies had no added effect on T cell activation when a non-pTag containing peptide (UU10) was used as the antigenic peptide emphasizing the critical role of the pTag in facilitating the CD40 mediated antigen uptake (Figure 4G). To further verify the CD40-dependent peptide uptake, WT BMDCs that lack hCD40 as the target were used, where no DC activation or T cell proliferation was noted by UU05/BiTag stimulation (Figure 4H).

Although $CD8^+$ T cells can be cross-primed by DCs on many occasions, like viral infections,[24] $CD4^+$ T cells are crucial to support long-lasting, effective cytotoxic and memory $CD8^+$ T cell responses.[25] To explore the flexibility of the platform, murine tghCD40 BMDC or human moDCs were pulsed with a different set of pTag-Ag, UU60 and UU44. These pTag-Ag include the ovalbumin $OT\text{-}II_{323\text{-}339}$ CD4 epitope or the CMV pp65 $NLV_{495\text{-}503}$ CD8 epitope, respectively. In the OT-II model, the pulsing of BMDC with UU60 in the presence of Bi10-1150 resulted in an apparent increase in OT-II specific $CD4^+$ T cell proliferation and upregulation of the expression of the activation marker ICOS (Figures 4I and 4J). Notably, the pulsing of the BMDCs with the pTag-SLP containing irrelevant epitope did not induce any $CD4^+$ T cell proliferation (data not shown). In the CMV model, Bi17-CP treatment enhanced the NLV-specific $CD8^+$ T cells (Figure 4K). Notably, the parental antibody CP-2 resulted in a comparable response to the BiTag version of the antibody, likely because this peptide has an inherent long half-life and as the closed nature of the in vitro system does not provide other sources of eliminations pathways than degradation, there is no added benefit by the BiTag in this specific setup with this specific peptide. The co-stimulation dependence of the assay, in contrast to the B3Z assay that is co-stimulation independent, might have also played a role when excess antigen is present.

3.4. The BiTag Platform Enhances Peptide-Specific T Cell Proliferation and Activation In Vivo

Next, the in vitro T cell expansion and activation of gp100 specific $CD8^+$ T cells (pmel-1) were assessed when tghCD40 BMDCs were pulsed with the pTag-Ag UU30 that contains hgp100 as an antigen. The presence of either the parental or the BiTag antibodies enhanced the pmel-1 activation in vitro (**Figure 5**A). Because of the noted in vitro system's limitation, being a closed system not mimicking the in vivo situation where the molecular weight

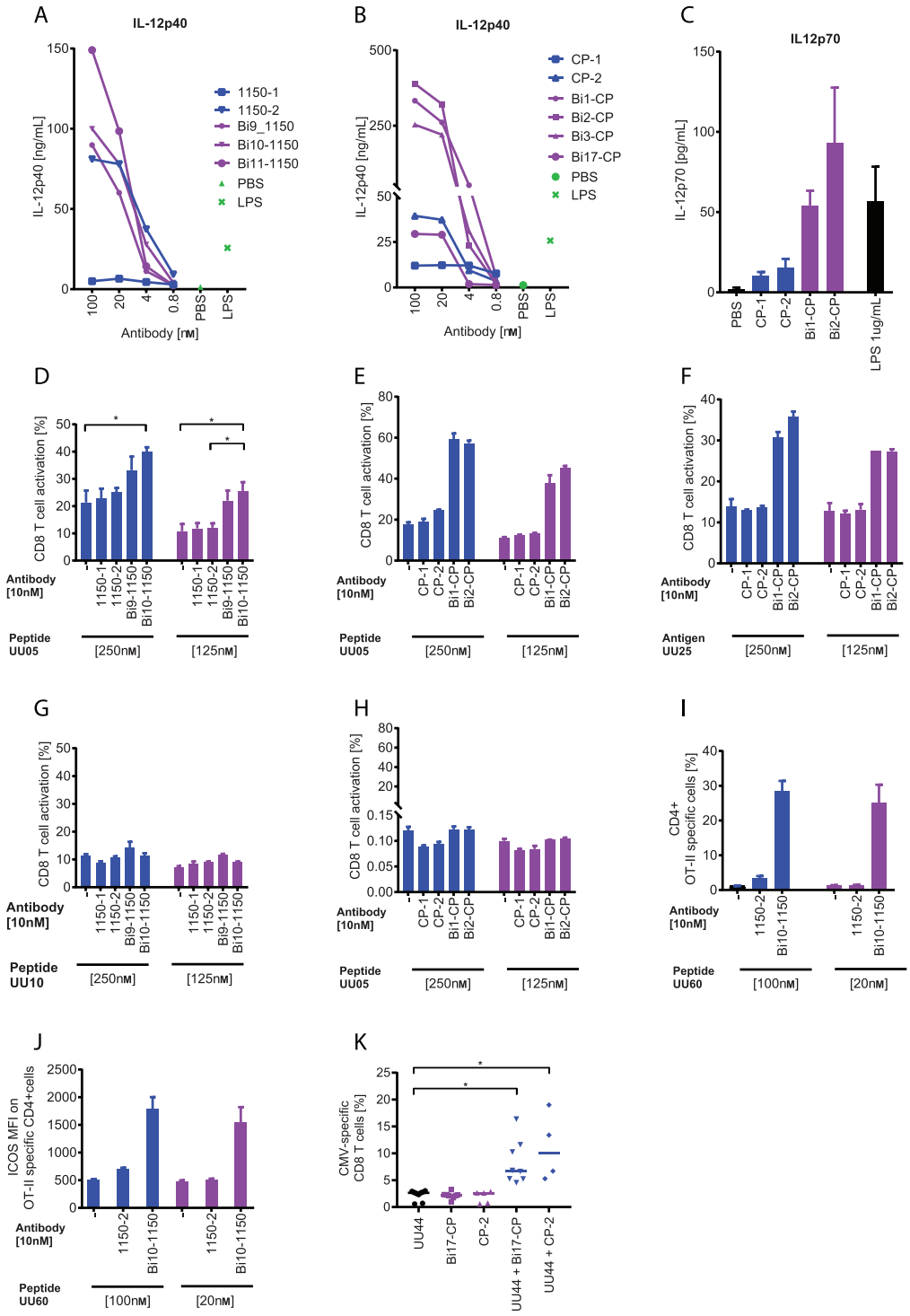

Figure 4. In vitro agonistic activity and antigen uptake enhancement by the BiTag platform. A–C) imBMDC from tghCD40 were treated with BiTag or parental antibodies for 48 h. IL-12p40 (A,B) or IL12p70 (C) concentrations were measured in the supernatant by ELISA 48 h after tghCD40 BMDC treatment or LPS. D–G) tghCD40 BMDC were treated with UU-05 (D,E), UU25 (F), or UU-10 (G) in the presence or absence of BiTag or parental antibodies. After 24 h, unbound treatments were washed and DCs were co-cultured with B3Z cells. B3Z cell activation was quantified after a further 24 h via measuring the colorimetric change in CPRG substrate as described in the Experimental Section. "CD8 T cell activation [%]" refers to the fraction of T cells activated in reference to the positive control, which saturates the colorimetric reaction at 100% activation. H) B3Z cell activation assay when wild type BMDC was pulsed with UU05 in the presence of BiTag or parental antibodies. I,J) Transgenic $CD4^+$ T cell proliferation (I), and ICOS expression (J) after co-culturing the T cells with OT-II pulsed tghCD40 BMDC with the pTag-OT-II peptide UU60. K) CMV specific $CD8^+$ T cell proliferation after co-culturing the T cells with UU44, a pTag containing CMV pp65 $NLV_{495\text{-}503}$ CD8 epitope, pulsed moDCs in the absence or the presence of BiTag or parental antibodies ($n = 4$–8). Dots represent the mean. Error bars represent SEM. * = $p < 0.05$, Kruskal Wallis test with Dunn's post-test.

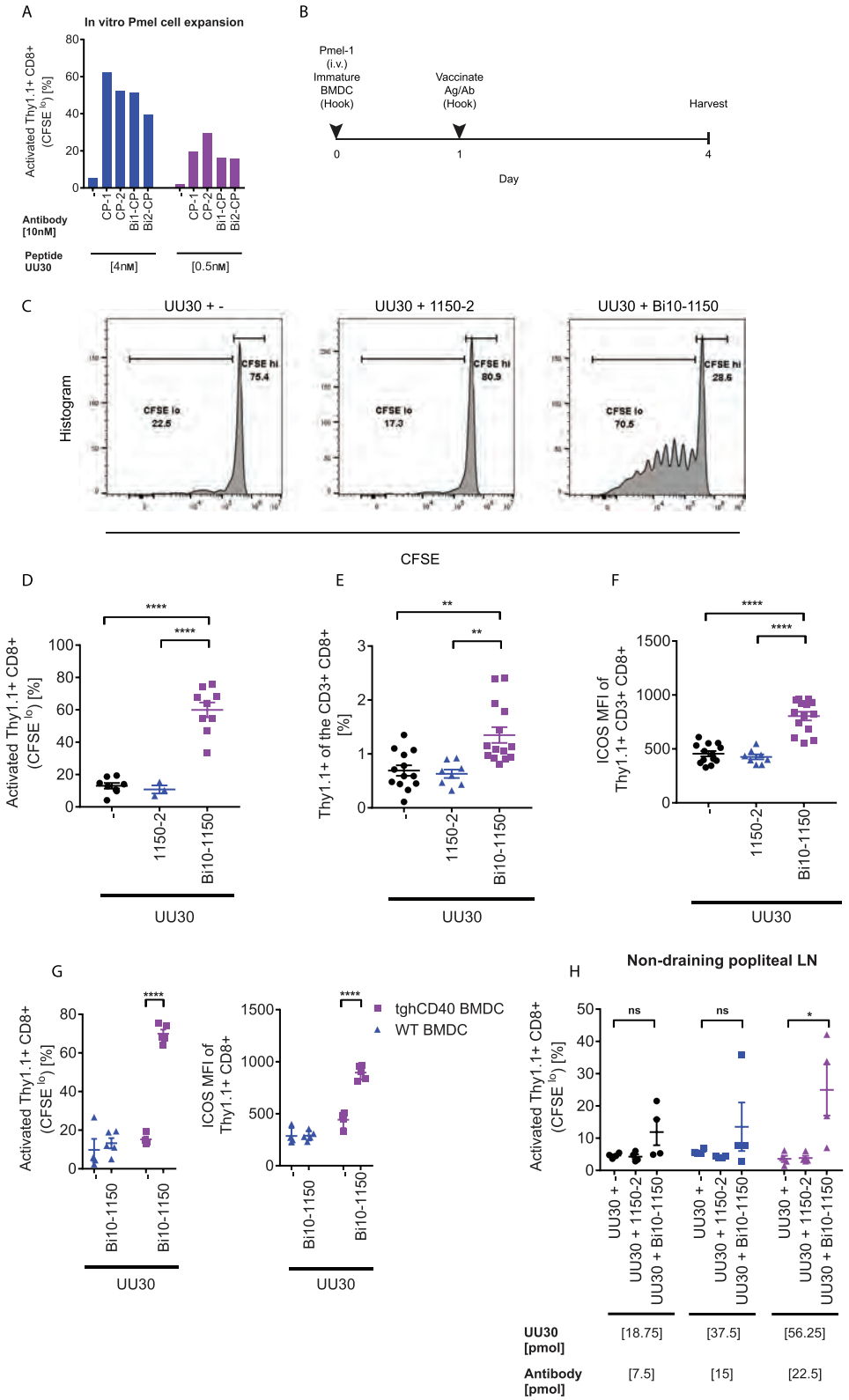

Figure 5. BiTag induces robust antigen-specific CD40-dependent CD8$^+$ T cell expansion and activation in vivo. A) In vitro activation and proliferation of the CFSE-labeled congenially marked thy1.1 Pmel-1 CD8$^+$ T cells when co-cultured with the tghCD40 BMDC were treated with UU30 peptide in the presence or the absence of BiTag or parental antibodies. After 24 h, unbound treatments were washed and DCs were co-cultured with pmel-1 CD8$^+$ T cells. Pmel-1 cell proliferation was quantified after a further 72 h. B) tghCD40 BMDC and CFSE-labeled thy1.1$^+$ Pmel-1 cells were transferred into the hock and intravenously, respectively. Mice were vaccinated with the peptide antigen UU30, UU30+Bi10-1150, or UU30+1150-2 in the same side hock

will determine the dispersion of the compounds, the activity of the BiTag platform was assessed in vivo using the pmel-1 model. CFSE-labeled pmel-1 cells were administrated by intravenous tail vein injection, and tghCD40 BMDCs were injected in the hock of C57BL/6 mice. The IgG2-based Bi10-1150 and 1150–2 were chosen for this experiment due to the uniform DC activation profile of the bispecific and parental antibodies and the superior T cell activation in vitro, along with literature supporting the IgG2 format for agonistic activity.[26–29] A mixture of UU30 and Bi10-1150 or 1150–2 was injected to the same side hock that received the tghCD40 BMDCs (Figure 5B). Draining popliteal lymph node analysis after 72 h of treatment identified an average of 60% expansion of pmel-1 (Thy1.1$^+$, CD3$^+$, CD8$^+$) cells in the UU30/Bi10-1150 group (Figure 5C–E). Similarly, the superiority of the BiTag in inducing antigen-specific T cell expansion was observed with Bi1-CP and Bi2-CP (Figure S9, Supporting Information). Besides this, ICOS was upregulated on the antigen-specific T cells in the group treated with UU30/Bi10-1150 combination compared to UU30 monotherapy or UU30/1150-2 in combination (Figure 5F). To confirm the CD40 dependence of the antigen uptake, the setup was repeated by transferring CFSE-labeled pmel-1 and WT BMDCs lacking the target hCD40 to the mice. Bi10-1150 did not induce Pmel-1 expansion or activation when WT BMDCs were transferred (Figure 5G). Furthermore, this experiment was repeated with increasing UU30 and antibody mix concentrations to investigate dose-dependent responses. There was no notable difference in the local pmel-1 cell activation/proliferation in the draining popliteal lymph node (Figure S10, Supporting Information). However, with the higher dose (56.25 pmol/22.5 pmol UU30/Bi10-1150), a significantly enhanced pmel-1 proliferation in the non-draining popliteal lymph node (Figure 5H) was noted. No pmel-1 cell proliferation or activation in the spleen was apparent at any doses. Together, these results demonstrate the in vivo CD40-dependent improved DC antigen delivery and presentation by the BiTag platform and that the effect is mainly localized, supporting the safety aspect of the therapy. T cell migration and tumor targeting will occur regardless of whether the priming and expansion are induced locally.

4. Discussion and Conclusion

Agonistic anti-CD40 antibodies have shown promising anticancer effects in pre-clinical evaluations via T cell-dependent[22,30] or T cell-independent mechanisms.[31,32] In the clinic, the maximum tolerated dose (MTD) is limited to ≈0.3 mg kg^{-1} for selicrelumab, and systemic leakage of tumor-localized, injected anti-CD40 therapy into highly vascularized tumors using mitazalimab (ADC-1013) has been shown to trigger systemic cytokine release.[33] As anti-CD40 antibodies rely on antigens for proper T cell activation in T cell-dependent anti-tumor responses, it is crucial to adapt CD40-targeting strategies. Bispecific antibody targeting strategies can be developed to target tumor antigens on the surface of the tumor cells, for example, targeting mesothelin/CD40[34,35] and HER2/CD40,[36] or surface-expressed tumor antigens that are also present on exosomes or other cellular released particles.[37] All with the ambition to couple the stimulation of CD40 with antigen presentation. However, a limitation of this strategy is its reliance on high expression of the tumor antigen to achieve effective tumor antigen-specific immune stimulation, which is not always the case and often there is a limited number of tumor-specific surface targets.[38] In addition, vesicles/exosomes that carry tumor material are also potentially immunosuppressive, increasing the risk for an ineffective antigen presentation pathway.[39–41] Next-generation sequencing offers a novel pathway to individualized therapies. Synthetic peptide drugs can be synthesized per individual based on sequencing data and epitope-based algorithm prediction strategies.[9] However, the peptides' physicochemical properties will affect the synthesis, identification, purification, solubility, and half-life. An alternative to the peptide-based vaccine is the use of the more traditional whole protein vaccine strategy for broad HLA and immunological response coverage. However, whole protein vaccines come with several limitations in cancer therapeutics. DCs are less efficient in presenting and cross-presenting antigens delivered as whole proteins compared to synthetic peptides.[42,43] Additionally, targeting endogenous proteins, as whole proteins combined with adjuvants, leads to the formation of polyclonal anti-drug antibodies against the endogenous protein, which can both impact the natural biology of the endogenous protein and increase the toxicity risk of the vaccine candidate. SLPs focus on the identified neoantigen regions, can maintain a proper HLA coverage if not trimmed to a specific epitope, and are produced with the focus on inducing a T cell response. Although antibody response may sometimes develop, it is to a specific linear peptide sequence and is less likely to bind the endogenous peptide sequence as that will have an alternative conformation in the endogenous protein.[44,45]

A significant difficulty with therapeutic peptides is the in vivo stability and the rapid clearance in the blood. Several approaches have been investigated to improve peptide half-life, including chemical modification of the peptide, for example, glycosylation or acetylation of the peptide's terminal amino acids,[46] or by ovalbumin conjugation or Fc fusions.[47,48] Herein, we show that, in addition to increasing the peptide immunogenicity, the peptide-BiTag interaction enhances the peptide half-life in mouse and human plasma both in vitro and in vivo. This amplifies the bioavailability and contributes to the improved immunogenicity of the BiTag peptide vaccination. Despite the observed improved half-life of all peptides tested, we did note that the effect was peptide dependent. It is thus likely that both the inherent stability of each peptide along with sequence-specific enzymatic cleavage sites and their distance to the pTag can impact the resulting

after 24 h. Draining and non-draining popliteal lymph nodes were analyzed after 72 h. C) Representative histograms showing T cell proliferation and the resulting CFSE signal intensity reduction. D–F) Draining popliteal LN flow cytometry analysis for pmel-1 expansion measured as D) %CFSE low, E) %thy1.1$^+$, and F) pmel-1 cell activation measured by ICOS expression (n = 3–14, data are pooled from 3 independent experiments). G) Comparison of pmel-1 cell expansion and activation in draining popliteal lymph node when WT versus tghCD40 BMDC are transferred to the hock (n = 4). H) Flow cytometry analysis of pmel-1 proliferation at the non-draining popliteal lymph node at antibody doses (7.5, 15, and 22.5 pM). The peptide is given at 2.5× of the antibody molar concentration. Data are shown as mean +/−SEM. * = $p < 0.05$, ** = <0.01, *** = $p < 0.001$, **** = $p < 0.0001$, Kruskal Wallis test with Dunn's post-test or Mann–Whitney test.

half-life either as a naked peptide or when in complex with the BiTag. Importantly, the superior BiTag responses are dependent on CD40-mediated uptake. Therefore, the dual effects of the CD40-mediated peptide uptake and half-life improvement result in the noted superior expansion of T cells using the ADAC approach. Bonifaz et al.[49] have shown earlier that antibody-mediated targeting of antigens to dendritic cells via DEC205 leads to tolerance rather than T cell activation in the absence of adjuvant, which one can overcome by adding CD40 agonistic stimulation, herein features that are combined in the form of dual delivery and adjuvant capacity by using the ADAC technology.

The agonistic anti-CD40 antibodies rely on the IgG2 format and the unique disulfide hinge for retained agonistic activity.[26–29] However, IgG1 formats are also employed, taking advantage of the FcγR interaction to deliver agonistic anti-CD40 signaling.[26,50] While BiTag antibodies of IgG1 format (e.g., Bi1-CP) appeared to retain their FcγRIIIA interaction in the SPR experiment, the human whole blood experiment indicated that the FcγRIIIA interaction was impaired, possibly by steric hindrance on cell surfaces by the presence of the scFv. Notably, however, the Fc interaction of BiTag with FcγRIIIB, and to some extent, FcγRIIA, appeared to be attenuated. Nonetheless, we observed no apparent differences between BiTag of IgG1 or IgG2 format in relation to agonistic activity when using murine tghCD40 BMDC. In contrast, when using human moDCs, the IgG2 format was superior to the IgG1 (data not shown), which is in line with previous studies.[26,29] Based on agonistic data and because Fc receptor interaction in trans may hamper antibody internalization, an Fc independent agonistic effect as IgG2 is preferred in our case. However, the antibody isotype and the interaction with FcγR warrant further investigation to evaluate the BiTag signaling via FcγR, and the toxicity implications, such as target cell depletion, related to FcγR interaction following anti-CD40 infusion or intratumoral administration.[33,51] It is also known from the literature that the IgG2 isotype is not entirely Fc inert, as it can cross-link human FcγRIIA when antibodies are bound to a target and the Fc part is presented in a complexed form,[52] also supported by our own data herein. This should be taken into account when improving cargo delivery to cells via the ADAC technology ahead.

Our study is not without limitations. The comparison between the BiTag platform and the parental agonistic anti-CD40 antibodies in vitro, where the antigens and antibodies are available in excess and do not follow the physiologic pharmacokinetics, including distribution and elimination, makes direct comparison challenging. In vitro BiTag-induced T cell activation was observed with all the in vitro models we tested. However, the superiority of the BiTag platform relative to the parental anti-CD40 was best studied in vivo when the peptides and the antibodies follow physiologic pharmacokinetics, where elimination of smaller molecular weight substances is rapid. Additionally, despite BiTag displaying superior antigen uptake and presentation by DCs in vivo, our in vivo model was based on adoptive transfer of transgenic human CD40 BMDCs, which limited characterization of the other critical APCs, B cells, and macrophages. Further analysis of these critical cell populations and the mode-of-action of the ADAC technology is thus warranted in human CD40 transgenic mice and by the use of humanized model systems.

In summary, the ADAC platform provides a means for flexible peptide-based therapeutic vaccines tailored for individualized cancer therapy. The increased immunogenicity and stability of the peptides using this strategy enable a local low dose of administration of the anti-CD40 antibody in conjunction with tumor antigens. The ADAC platform removes the constraint of an intratumoral injection in deep tumor lesions, the risk of expanding myeloid suppressor cells in the tumor, as well as the toxicity profile of the intravenous infusion. It also provides antigens in cases where tumor antigen release is not sufficient. This promising pre-clinical proof-of-concept and characterization of this novel bispecific approach justify further clinical development of this approach to study its effects in treating human cancer.

Supporting Information

Supporting Information is available from the Wiley Online Library or from the author.

Acknowledgements

The authors thank Peter Ellmark and Adnan Deronic (Alligator Biosciences, Lund, Sweden) for providing bones to prepare bone marrow dendritic cells from the transgenic human CD40 mouse strain. They thank all the blood donors for their contribution in providing them with blood samples. They thank the financial support from the Swedish Society for Medical Research and Knut and Alice Wallenberg Foundation as well as SweLife/Vinnova, all to S.M.M.

Conflict of Interest

S.M.M. is a co-founder of Immuneed, Vivologica, and Strike Pharma and holds shares in the above companies. M.E., I.L., and M.L. are co-founders and shareholders in Strike Pharma. S.M.M. and M.E. are shareholders in Ultimovacs ASA, and S.M.M. is also an employee of Ultimovacs AB. None of the companies have had any influence over the work nor have contributed financially to the work presented herein.

Data Availability Statement

The data is freely available and is already provided in the manuscript as a whole.

Keywords

Antibody Drug Affinity Conjugate (ADAC), cancer vaccine, cargo delivery, CD40, immunotherapy, multivalent antibodies, synthetic peptides

Received: February 6, 2022
Revised: April 4, 2022
Published online: June 14, 2022

[1] T. R. Pearce, K. Shroff, E. Kokkoli, *Adv. Mater.* **2012**, *24*, 3803.
[2] C. D. Spicer, C. Jumeaux, B. Gupta, M. M. Stevens, *Chem. Soc. Rev.* **2018**, *47*, 3574.
[3] S. D. Xiang, K. L. Wilson, A. Goubier, A. Heyerick, M. Plebanski, *Front. Immunol.* **2018**, *9*, 2968.
[4] A. de Mare, A. J. A. Lambeck, J. Regts, G. M. van Dam, H. W. Nijman, H. Snippe, J. Wilschut, T. Daemen, *Gene Ther.* **2008**, *15*, 393.

[5] W. Yin, L. Gorvel, S. Zurawski, D. Li, L. Ni, D. Duluc, K. Upchurch, J. R. Kim, C. Gu, R. Ouedraogo, Z. Wang, Y. Xue, H. M. Joo, J. P. Gorvel, G. Zurawski, S. K. Oh, *eBioMedicine* **2016**, *5*, 46.
[6] T. A. Barr, A. L. McCormick, J. Carlring, A. W. Heath, *Immunology* **2003**, *109*, 87.
[7] C. Hatzifoti, A. W. Heath, *Immunology* **2007**, *122*, 98.
[8] J. Carlring, M. J. Szabo, R. Dickinson, E. De Leenheer, A. W. Heath, *Blood* **2012**, *119*, 2056.
[9] Z. Hu, P. A. Ott, C. J. Wu, *Nat. Rev. Immunol.* **2018**, *18*, 168.
[10] S. M. Mangsbo, S. Broos, E. Fletcher, N. Veitonmäki, C. Furebring, E. Dahlén, P. Norlén, M. Lindstedt, T. H. Tötterman, P. Ellmark, *Clin. Cancer Res.* **2015**, *21*, 1115.
[11] L. C. Sandin, T. H. Tötterman, S. M. Mangsbo, *Oncoimmunology* **2014**, *3*, e27400.
[12] L. C. Sandin, A. Orlova, E. Gustafsson, P. Ellmark, V. Tolmachev, T. H. Tötterman, S. M. Mangsbo, *Cancer Immunol. Res.* **2014**, *2*, 80.
[13] P. Y. Pan, G. Ma, K. J. Weber, J. Ozao-Choy, G. Wang, B. Yin, C. M. Divino, S. H. Chen, *Cancer Res.* **2010**, *70*, 99.
[14] J. Karttunen, S. Sanderson, N. Shastri, *Proc. Natl. Acad. Sci. USA* **1992**, *89*, 6020.
[15] W. W. Overwijk, M. R. Theoret, S. E. Finkelstein, D. R. Surman, L. A. De Jong, F. A. Vyth-Dreese, T. A. Dellemijn, P. A. Antony, P. J. Spiess, D. C. Palmer, D. M. Heimann, C. A. Klebanoff, Z. Yu, L. N. Hwang, L. Feigenbaum, A. M. Kruisbeek, S. A. Rosenberg, N. P. Restifo, *J. Exp. Med.* **2003**, *198*, 569.
[16] M. J. Barnden, J. Allison, W. R. Heath, F. R. Carbone, *Immunol. Cell Biol.* **1998**, *76*, 34.
[17] E. A. K. Fletcher, W. van Maren, R. Cordfunke, J. Dinkelaar, J. D. C. Codee, G. van der Marel, C. J. M. Melief, F. Ossendorp, J. W. Drijfhout, S. M. Mangsbo, *J. Immunol.* **2018**, *201*, 87.
[18] E. Söderlind, L. Strandberg, P. Jirholt, N. Kobayashi, V. Alexeiva, A. M. Åberg, A. Nilsson, B. Jansson, M. Ohlin, C. Wingren, L. Danielsson, R. Carlsson, C. A. K. Borrebaeck, *Nat. Biotechnol.* **2000**, *18*, 852.
[19] C. Preger, E. Wigren, E. Ossipova, C. Marks, J. Lengqvist, C. Hofström, O. Andersson, P. J. Jakobsson, S. Gräslund, H. Persson, *J. Biol. Chem.* **2020**, *295*, 13981.
[20] J. R. Wisñiewski, F. Z. Gaugaz, *Anal. Chem.* **2015**, *87*, 4110.
[21] E. A. K. Fletcher, M. Eltahir, F. Lindqvist, J. Rieth, G. Törnqvist, J. Leja-Jarblad, S. M. Mangsbo, *Int. Immunopharmacol.* **2018**, *54*, 1.
[22] R. R. French, H. T. C. Chan, A. L. Tutt, M. J. Glennie, *Nat. Med.* **1999**, *5*, 548.
[23] M. Eltahir, E. Fletcher, L. Dynesius, J. L. Jarblad, M. Lord, I. Laurén, M. Zekarias, X. Yu, M. S. Cragg, C. Hammarström, K. H. Levedahl, M. Höglund, G. Ullenhag, M. Mattsson, S. M. Mangsbo, *Int. Immunopharmacol.* **2021**, *90*, 107226.
[24] K. Nopora, C. A. Bernhard, C. Ried, A. A. Castello, K. M. Murphy, P. Marconi, U. Koszinowski, T. Brocker, *Front. Immunol.* **2012**, *3*, 348.
[25] E. M. Janssen, E. E. Lemmens, T. Wolfe, U. Christen, M. G. Von Herrath, S. P. Schoenberger, *Nature* **2003**, *421*, 852.
[26] A. L. White, H. T. C. Chan, R. R. French, J. Willoughby, C. I. Mockridge, A. Roghanian, C. A. Penfold, S. G. Booth, A. Dodhy, M. E. Polak, E. A. Potter, M. R. Ardern-Jones, J. S. Verbeek, P. W. M. Johnson, A. Al-Shamkhani, M. S. Cragg, S. A. Beers, M. J. Glennie, *Cancer Cell* **2015**, *27*, 138.
[27] M. Eltahir, H. Persson, S. Mangsbo, *Expert Opin. Biol. Ther.* **2020**, *20*, 215.
[28] X. Yu, H. T. C. Chan, C. M. Orr, O. Dadas, S. G. Booth, L. N. Dahal, C. A. Penfold, L. O'Brien, C. I. Mockridge, R. R. French, P. Duriez, L. R. Douglas, A. R. Pearson, M. S. Cragg, I. Tews, M. J. Glennie, A. L. White, *Cancer Cell* **2018**, *33*, 664.
[29] X. Yu, H. T. C. Chan, H. Fisher, C. A. Penfold, J. Kim, T. Inzhelevskaya, C. I. Mockridge, R. R. French, P. J. Duriez, L. R. Douglas, V. English, J. S. Verbeek, A. L. White, I. Tews, M. J. Glennie, M. S. Cragg, *Cancer Cell* **2020**, *37*, 850.
[30] G. J. D. Van Mierlo, A. T. Den Boer, J. P. Medema, E. I. H. Van Der Voort, M. F. Fransen, R. Offringa, C. J. M. Melief, R. E. M. Toes, *Proc. Natl. Acad. Sci. USA* **2002**, *99*, 5561.
[31] H. D. Lum, I. N. Buhtoiarov, B. E. Schmidt, G. Berke, D. M. Paulnock, P. M. Sondel, A. L. Rakhmilevich, *J. Leukocyte Biol.* **2006**, *79*, 1181.
[32] G. L. Beatty, E. G. Chiorean, M. P. Fishman, B. Saboury, U. R. Teitelbaum, W. Sun, R. D. Huhn, W. Song, D. Li, L. L. Sharp, D. A. Torigian, P. J. O'Dwyer, R. H. Vonderheide, *Science* **2011**, *331*, 1612.
[33] S. M. M. Irenaeus, D. Nielsen, P. Ellmark, J. Yachnin, A. Deronic, A. Nilsson, P. Norlén, N. Veitonmäki, C. S. Wennersten, G. J. Ullenhag, *Int. J. Cancer* **2019**, *145*, 1189.
[34] S. Ye, D. Cohen, N. A. Belmar, D. Choi, S. S. Tan, M. Sho, Y. Akamatsu, H. Kim, R. Iyer, J. Cabel, M. Lake, D. Song, J. Harlan, C. Zhang, Y. Fang, A. F. Wahl, P. Culp, D. Hollenbaugh, D. T. Chao, *Cancer Immunol. Res.* **2019**, *7*, 1864.
[35] J. J. Luke, L. Fong, K. Chung, A. W. Tolcher, K. Kelly, A. Hollebecque, C. Le Tourneau, V. Subbiah, F. Tsai, S. Kao, P. Cassier, M. Khasraw, K. Allaire, F. Fan, H. Fang, M. Patel, W. Henner, J. Hayflick, M. McDevitt, F. Barlesi, *Ann. Oncol.* **2019**, *30*, v498.
[36] L. Lu, N. Liu, K. Fan, G. Zhang, C. Li, Y. Yan, T. Liu, W. H. Fu, *Mol. Immunol.* **2019**, *109*, 149.
[37] P. Ellmark, K. Hägerbrand, M. Levin, L. Von Schantz, A. Deronic, L. Varas, A. Säll, K. Barchan, D. Werchau, L. Ljug, M. Thageson, A. Rosen, C. Sakellariou, M. Lindstedt, P. Ellmark, *J. Immunother. Cancer* **2020**, *8*, A911.
[38] T. So, M. Takenoyama, M. Mizukami, Y. Ichiki, M. Sugaya, T. Hanagiri, K. Sugio, K. Yasumoto, *Cancer Res.* **2005**, *65*, 5945.
[39] G. H. Nam, Y. Choi, G. B. Kim, S. Kim, S. A. Kim, I. S. Kim, *Adv. Mater.* **2020**, *32*, 2002440.
[40] K. Gabrusiewicz, X. Li, J. Wei, Y. Hashimoto, A. L. Marisetty, M. Ott, F. Wang, D. Hawke, J. Yu, L. M. Healy, A. Hossain, J. C. Akers, S. N. Maiti, S. Yamashita, Y. Shimizu, K. Dunner, M. A. Zal, J. K. Burks, J. Gumin, F. Nwajei, A. Rezavanian, S. Zhou, G. Rao, R. Sawaya, G. N. Fuller, J. T. Huse, J. P. Antel, S. Li, L. Cooper, E. P. Sulman, et al., *Oncoimmunology* **2018**, *7*, e1412909.
[41] F. Chalmin, S. Ladoire, G. Mignot, J. Vincent, M. Bruchard, J. P. Remy-Martin, W. Boireau, A. Rouleau, B. Simon, D. Lanneau, A. De Thonel, G. Multhoff, A. Hamman, F. Martin, B. Chauffert, E. Solary, L. Zitvogel, C. Garrido, B. Ryffel, C. Borg, L. Apetoh, C. Rébé, F. Ghiringhelli, *J. Clin. Invest.* **2010**, *120*, 457.
[42] R. A. Rosalia, E. D. Quakkelaar, A. Redeker, S. Khan, M. Camps, J. W. Drijfhout, A. L. Silva, W. Jiskoot, T. van Hall, P. A. van Veelen, G. Janssen, K. Franken, L. J. Cruz, A. Tromp, J. Oostendorp, S. H. van der Burg, F. Ossendorp, C. J. M. Melief, *Eur. J. Immunol.* **2013**, *43*, 2554.
[43] M. L. Disis, J. R. Gralow, H. Bernhard, S. L. Hand, W. D. Rubin, M. A. Cheever, *J. Immunol.* **1996**, *156*, 3151.
[44] E. M. J. van Brummelen, W. Ros, G. Wolbink, J. H. Beijnen, J. H. M. Schellens, *Oncologist* **2016**, *21*, 1260.
[45] K. P. Pratt, *Antibodies* **2018**, *7*, 19.
[46] A. K. Sato, M. Viswanathan, R. B. Kent, C. R. Wood, *Curr. Opin. Biotechnol.* **2006**, *17*, 638.
[47] R. Léger, K. Thibaudeau, M. Robitaille, O. Quraishi, P. van Wyk, N. Bousquet-Gagnon, J. Carette, J. P. Castaigne, D. P. Bridon, *Bioorg. Med. Chem. Lett.* **2004**, *14*, 4395.
[48] J. A. Dumont, S. C. Low, R. T. Peters, A. J. Bitonti, *BioDrugs* **2006**, *20*, 151.
[49] L. Bonifaz, D. Bonnyay, K. Mahnke, M. Rivera, M. C. Nussenzweig, R. M. Steinman, *J. Exp. Med.* **2002**, *196*, 1627.
[50] R. H. Vonderheide, *Annu. Rev. Med.* **2020**, *71*, 47.
[51] P. Johnson, R. Challis, F. Chowdhury, Y. Gao, M. Harvey, T. Geldart, P. Kerr, C. Chan, A. Smith, N. Steven, C. Edwards, M. Ashton-Key, E. Hodges, A. Tutt, C. Ottensmeier, M. Glennie, A. Williams, *Clin. Cancer Res.* **2015**, *21*, 1321.
[52] P. Bruhns, B. Iannascoli, P. England, D. A. Mancardi, N. Fernandez, S. Jorieux, M. Daëron, *Blood* **2009**, *113*, 3716.

Patients are waiting for ADCs like yours

Every day, scientists like you are discovering exciting new possibilities related to antibody-drug conjugates (ADCs). ADCs have the potential to save many lives — but they also present hurdles when it comes to process development and manufacturing.

At Cytiva, our scientists share the same mission to advance and accelerate therapeutics. We drive rapid innovation to meet an ever-growing demand for novel therapies that are precise, personalized, and effective. No matter where you are in the pipeline, we're ready to help you reach your next milestone.

Discover our solutions for optimizing your process and unlocking the full potential of your ADC.

Learn more